Appendix 1

Milan Bousa, Barbora Laskova, Marketa Zukalova, Jan Prochazka, Alison Chou and Ladislav Kavan. "Polycrystalline TiO_2 Anatase with a Large Proportion of Crystal Facets (001): Lithium Insertion Electrochemistry." *J. Electrochem. Soc*, 2010, **157**, A1108-A1112.

Journal of The Electrochemical Society, **157** (10) A1108-A1112 (2010)
0013-4651/2010/157(10)/A1108/5/$28.00 © The Electrochemical Society

Polycrystalline TiO_2 Anatase with a Large Proportion of Crystal Facets (001): Lithium Insertion Electrochemistry

Milan Bousa,[a,c] Barbora Laskova,[a,c] Marketa Zukalova,[a] Jan Prochazka,[a,*] Alison Chou,[b] and Ladislav Kavan[a,c,*,z]

[a] *J. Heyrovský Institute of Physical Chemistry, v.v.i., Academy of Sciences of the Czech Republic, CZ-18223 Prague 8, Czech Republic*
[b] *Australian Research Council Centre of Excellence for Functional Nanomaterials, The University of Queensland, Queensland 4072, Australia*
[c] *Department of Inorganic Chemistry, Faculty of Science, Charles University, CZ-12840 Prague 2, Czech Republic*

The electrochemical behavior of TiO_2 anatase with a predominant (001) face (ANA001) was studied by cyclic voltammetry of Li insertion and chronoamperometry. Both voltammetric and chronoamperometric diffusion coefficients and rate constants proved the higher activity of ANA001 toward Li insertion compared to that of a reference anatase material (C240) with dominating (101) facets. The enhanced activity of the anatase (001) face for Li insertion stems from synergic contributions of a faster interfacial charge transfer at this surface and a facile Li transport within a more open structure of the anatase lattice in the direction parallel to the *c*-axis. Despite the larger particle size of ANA001, the values of integral charge capacity and Li-insertion coefficient further confirmed its improved Li-insertion properties. The results of this study further complete the analogous data published on single-crystal anatase electrodes and evidence their validity for nanocrystalline materials too.
 [DOI: 10.1149/1.3479192]

Manuscript submitted June 10, 2010; revised manuscript received July 16, 2010. Published August 25, 2010.

The insertion of lithium into TiO_2 (anatase) has been a subject of intense research in the past (see, e.g., Ref. 1-6, for review Ref. 7). Anatase accommodates lithium electrochemically, which can be schematically described by the equation

$$TiO_2 + x(Li^+ + e^-) \rightarrow Li_xTiO_2\ ; \quad x \approx 0.5 \qquad [1]$$

Fundamental studies have been carried out on anatase single-crystal electrodes.[5,6] For the fabrication of electrodes, macroscopic (millimeter-sized) single crystals were grown in two orientations with the exposed faces (101) or (001), respectively.[5,6] The (001) face had more negative flatband potential and was more active for Li insertion than the (101) face.[5] The conclusion about the flatband potential shift has been recently confirmed also on polycrystalline electrodes.[8] A different activity for Li insertion was attributed to a more open structure of the anatase lattice in the direction parallel to the *c*-axis.[5] The actual argument was that the anisotropy of Li^+ transport normal to the (101) and (001) faces was a consequence of different numbers the Li^+ hopping events between pseudo-octahedral positions in the anatase lattice.[5]

Due to its thermodynamic stability, the (101) face is dominating in the usual TiO_2 materials (>94% of the total surface area of ordinary crystals).[9] Hence, many earlier studies of polycrystalline anatase electrodes addressed the effects occurring virtually on this face only. Obviously, the studies of polycrystalline electrodes, made from industrial powders[10] or from laboratory-made materials,[11,12] should rather be regarded as the investigation of anatase (101) because the proportion of other crystal faces is, in general, very low. The remaining face on anatase crystal is (001), which is consistent with the conclusion that a truncated bipyramid is the corresponding crystal morphology.[13] Only rarely, the rhombic crystals are found, exposing the (010) face.[14] Both (001) and (010) facets are called "high energy" or "reactive" ones. They show interesting activity in catalysis and photocatalysis.[14-16]

Recently, Yang et al.[9] have discovered that micrometer-sized platelets of anatase with 47% of (001) facets can be grown hydrothermally from a TiF_4 aqueous solution with HF; the latter acts as the morphology directing agent. The unusual crystal shape of very flat truncated bipyramids was stabilized by fluorine termination of the surface, but the surface can be cleaned from fluorine by heat-treatment without affecting the crystal shape. This work was announced as the first demonstration of large anatase crystals with high percentage of (001) facets.[9] Although there were also earlier works on the pure (001) face,[5] the facile synthesis of microcrystalline anatase enriched with (001) faces[9] opened a pathway to a deeper investigation of orientation-dependent effects in polycrystalline anatase materials. The follow-up studies[15-18] have reported on materials enriched up to 89% with the (001) face.

To our knowledge, there is only one paper reporting on Li insertion into a F-terminated anatase (001) nanosheet.[17] It concluded that the nanosheet showed improved charge capacity and cycle life. However, it is unclear whether the effect is caused by the F-atom modified surface (doping) or by the crystal morphology itself.[17] The investigation of F-free materials remains to be a challenge, which was the central motivation of our study. Also, we report here on a detailed investigation of Li-insertion kinetics, which upgrades the earlier works on single-crystal electrodes[5] and polycrystalline (001) nanosheets.[17]

Experimental

Preparation of electrodes.— Anatase was prepared as follows: 1.2 mL of HF (50%; Ajax Finechem) was added to 10 mL of titanium(IV) butoxide. The mixture was sealed in a Teflon cell encased in a stainless steel autoclave and heated at 200°C for 24 h. The sample was collected after 24 h of heating and washed with copious amounts of Milli-Q water. The solid was dried at 100°C. The as-received material contained 8 wt % of F, as determined by energy-dispersive X-ray (EDX) analysis (see below for details). After calcination (450°C, 30 min) the F content dropped practically to zero. X-ray diffraction (XRD) patterns and scanning electron microscopy (SEM) images (data not shown) confirmed that the material was phase-pure anatase with the plateletlike morphology,[9,17] whereas both the phase composition and crystal morphology remained intact during this thermal treatment. The material is further abbreviated as ANA001. For comparison was used a material coded as C240.[10] Briefly, C240 is a nanocrystalline anatase with the Brunauer–Emmett–Teller (BET) surface area, $S_{BET} = 89\ m^2/g$. It was prepared by hydrolysis of titanium tetra(isopropoxide), which was followed by hydrothermal recrystallization at 240°C in autoclave.[19] The crystal morphology of C240 is characterized by particles ca. 10–20 nm in size exposing mainly the (101) facets.[20] A second reference material was titanium dioxide P90 (from Degussa AG, Germany) powder, with a S_{BET} of 100 m^2/g [rutile/anatase mixture with >90% anatase with trace amount of TiO_2(B)].[21] For the preparation of electrodes, the powder samples were sonicated in pure

* Electrochemical Society Active Member.
z E-mail: kavan@jh-inst.cas.cz

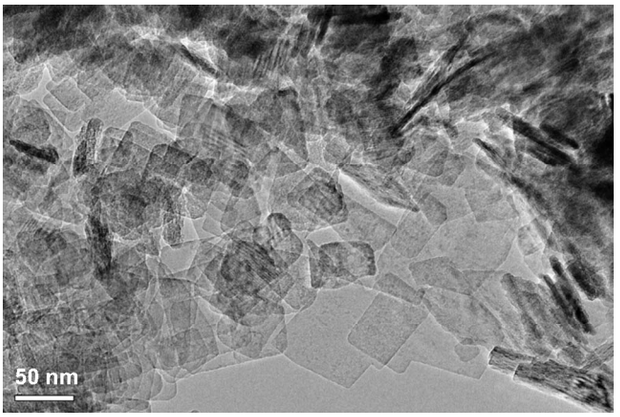

Figure 1. TEM image of the sample ANA001. Scale bar 50 nm.

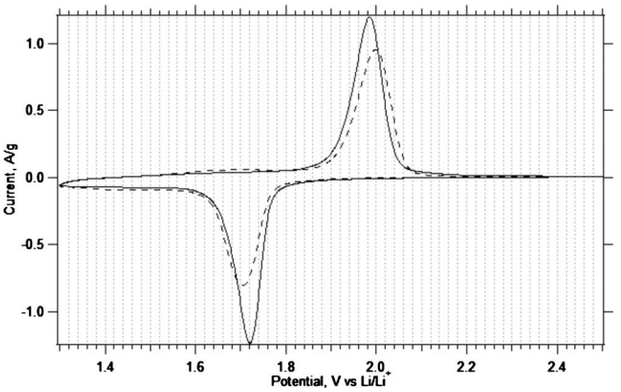

Figure 2. Cyclic voltammogram of ANA001 (solid lines) and C240 (dashed lines) in 1 M $LiN(CF_3SO_2)_2$ + EC/DMC (1/1 by mass). Scan rate was 0.2 mV/s. Smaller separation of anodic and cathodic peaks of ANA001 confirms better Li-insertion kinetics.

ethanol. The obtained slurry was deposited on an electrode support (titanium grid, 5 mm × 25 mm, Dexmet, 0.14 mm thick) as in Ref. 22. The electrodes were prepared by dip-coating and the coated area was 5 mm × 10 mm. The electrodes were dried in air and then sintered at 450°C in air for 30 min. The final mass of active material on a grid was between 0.1 and 0.7 mg. Blank experiments proved a negligible contribution of a bare titanium grid to the overall charge capacity of a particular electrode.

Methods.— The transmission electron microscopy (TEM) images were measured on JEOL-2100 microscope. The BET surface areas of the prepared materials were determined from nitrogen adsorption isotherms at 77 K using the Micromeritics ASAP 2020 instrument. Before the adsorption measurement, all samples were degassed at 300°C overnight. SEM and EDX analyses were carried out using a Hitachi field-emission-scanning electron microscope S-4800 equipped with the Noran EDX system. Powder XRD was studied on a Bruker D8 Advance diffractometer using Cu Kα radiation. Electrochemical measurements were carried out in a one-compartment cell using an Autolab Pgstat-30 (Eco Chemie) controlled by GPES-4 software. The electrolyte solution was 1 mol/L $LiN(CF_3SO_2)_2$ in ethylene carbonate (EC) + dimethyl carbonate (DMC) (1/1 w/w). The reference and counter electrodes were from Li metal; hence, all potentials were quoted against the Li/Li^+ reference electrode in this medium. All electrochemical measurements were carried out in a glove box under Ar atmosphere.

Results and Discussion

The morphology of our polycrystalline TiO_2 anatase with a predominant (001) face (ANA001) was characterized by TEM (Fig. 1). The anatase crystals are not truncated bipyramids (cf. Ref. 9) but rectangular platelets with a thickness of ~5 to 8 nm. The specific surface area of ANA001 determined from nitrogen adsorption measurement was S_{BET} = 68 m^2/g. (The theoretical surface area of an anatase platelet 50 mm × 50 mm × 8 nm in size is 85 m^2/g, which is not too far from the experimental value.) The morphology of our sample is similar to that of Chen and Lou,[17] which simplifies the comparison of the electrochemical activity of both materials (see below).

Cyclic voltammetry (CV) of the Li insertion of ANA001 and a reference material C240 was measured in a potential window of 1.3/2.5 V at different scan rates. The main selection criterion for the reference material (C240) was its particle size (10–20 nm) and surface area (S_{BET} = 89 m^2/g) roughly comparable to that of ANA001. More importantly, C240 is distinguished by exposing mostly the (101) facets in quite uniform bipyramidal crystals.[20] Figure 2 compares the cyclic voltammograms of the above-mentioned samples at a scan rate of 0.2 mV/s. They exhibit just one pair of peaks with a formal potential (E_f) of 1.85 V assignable to the presence of phase-pure anatase.[5,10,21,23] Our ANA001 material exhibited a symmetrical cyclic voltammogram (as in Fig. 2) even for the first run on virgin electrode. This is a distinct difference from the data of Chen and Lou,[17] who presented a cathodic double peak for the first run on their (001)-terminated material. The effect was not commented in Ref. 17, but it is presumably not a consequence of particle morphology, which is known to influence prevailingly the shape of the anodic peak rather than the cathodic peak.[12] For completeness, we should also notice different electrolyte solutions used in the cited study.[17]

The peak-to-peak splitting (ΔE_p) is obviously smaller for ANA001 compared to that for C240 (Fig. 2). This splitting is known to be inversely proportional to S_{BET} for a variety of anatase samples.[12,22] The comparison of ANA001 vs C240 indicates just the opposite trend, that is, the decrease in ΔE_p for ANA001 having smaller S_{BET}. This provided a qualitative indication of improved Li-insertion properties of the latter material.

To arrive at more quantitative data, we calculated the parameters of Li-insertion kinetics in both materials. To that purpose, we use the formalism of diffusion-controlled charge transfer, which describes the faradaic insertion reaction.[3-6,22-27] In CV, the insertion/extraction peak current (I_p) scales with the square root of the scan rate (v) [3-5,23,25,28]

$$|I_p| = 0.4958nFAc(D_{Li}\alpha nFv/RT)^{1/2} \quad [2]$$

where n is the number of electrons, A is the electrode area, c is the maximum concentration of Li^+ in the accumulation layer (0.024 mol/cm^3 for x = 0.5; cf. Eq. 1), α is the charge-transfer coefficient, and the other symbols have their usual meaning. For accurate analysis, the voltammetric peak current in Eq. 2 should be corrected for the capacitive component,[3] which was usually neglected in earlier studies.[4-6,22-27] In our case, the correction is not significant because we compare anatase materials of similar surface areas. The kinetic analysis of voltammetric data (Fig. 3A) proved that Li insertion into ANA001 and C240 can be treated by Eq. 2. The values of D_{Li} calculated from CV (Table I) quantitatively describe the Li^+ transport in both samples and were of ~1 order of magnitude higher for ANA001. Hence, Li insertion is facilitated in anatase with a predominant (001) face. This fully agrees with previously published results on macroscopic single-crystal electrode[5] and confirms that the anisotropy of Li^+ transport is clearly expressed in polycrystalline materials too.

For assessment of the quality of Li-insertion host, we can also determine the standard rate constant of charge transfer (k_0). The voltammetric peak current (I_p) scales with the peak potential (E_p) [5,22,28]

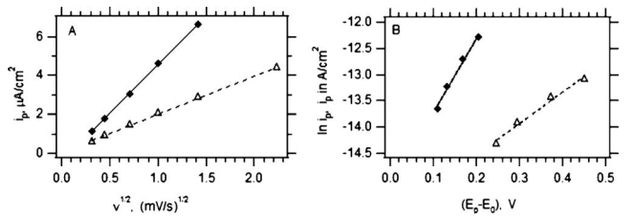

Figure 3. (A) Voltammetric peak current densities vs square root of the scan rate. Data for ANA001 (full squares) and C240 (open triangles) are plotted according to Eq. 2. The steeper slope of the fit for ANA001 (solid lines) as compared to that for C240 (dashed lines) is obvious and indicates higher diffusion coefficient of the former material. (B) Current densities of voltammetric peaks vs the potential difference depicted with a fit according to Eq. 3. Solid lines and full squares: ANA001. Dashed lines and open triangles: C240.

$$|I_p| = 0.227AnFck_0 \exp\left[\frac{-\alpha nF(E_p - E_f)}{RT}\right] \quad [3]$$

The standard rate constants of Li insertion into ANA001 and C240 were calculated from slopes of the dependence of current densities of voltammetric peaks on $E_p - E_f$ according to Eq. 3 (Fig. 3B) and are listed in Table I. Analogous to D_{Li} values, standard rate constants also evidence the higher activity of ANA001 toward Li insertion.

Table I summarizes the lithium-insertion coefficients (x) (Eq. 1) and the corresponding integral charge capacity (C). Our results support the conclusion of Chen and Lou for a similar (001)-dominated sample.[17] However, these authors[17] reported on dramatically smaller capacities for their reference materials. For instance, P-25 (Degussa) reportedly exhibited ca. 75 mAh/g at 1C rate ($x \approx 0.2$), which was less than half of the capacity of their (001) material (ca. 200–175 mAh/g at 1C rate). This is a surprisingly large difference, especially if we consider that others[10] reported on $x \approx 0.42$ for P-25. Despite this numerical mismatch, obviously, the (001)-terminated materials, like our ANA001, exhibit superior performance at comparable conditions, which surpass those of various reference titania materials.

Further insight into the kinetics of Li insertion and the verification of the values of D_{Li} provided a series of chronoamperometric measurements carried out with an electrode polarized by square wave potential steps. The potential was stepped from 1.3 to 3 V and back, and the duration of each potential step was 1000 s.

In potential-step chronoamperometry (CHA), the insertion/extraction current (I) obeys the Cottrell equation[5,6,22,23,27]

Table I. Electrochemical parameters of Li insertion into ANA001, P90, and C240 obtained by analysis of voltammetric and chronoamperometric data. Symbols CV and CHA specify method used for calculation of diffusion coefficients.

	ANA001	P90	C240
Rate constant k_0 (cm/s)	5×10^{-10}	3×10^{-10}	3×10^{-10}
Charge-transfer coefficient α	0.36	0.38	0.15
Diff. coefficient D_{Li} (cm^2/s) CV	1.33×10^{-18}	4.65×10^{-19}	4.89×10^{-19}
Diff. coefficient D_{Li} (cm^2/s) CHA	5.43×10^{-15}	3.20×10^{-15}	3.40×10^{-15}
Charge capacity C (C/g)	616	570	550
Lithium insertion coefficient x	0.51	0.47	0.46
Activation energy E_A (eV)	0.09	0.14	0.17
Formal potential E_f (V)	1.849	1.848	1.858

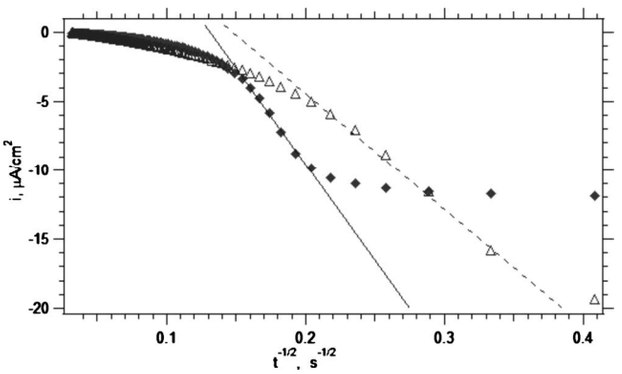

Figure 4. Chronoamperometric plot of ANA001 (full squares) and C240 (open triangles) in 1 M $LiN(CF_3SO_2)_2$ + EC/DMC (1/1 by mass). Diagram in coordinates i vs $t^{-1/2}$. Chronoamperometric data are for ANA001 (solid lines, full squares) and C240 (dashed lines, open triangles) plotted according to Eq. 4.

$$|I| = AFD_{Li}^{1/2}c\pi^{-1/2}t^{-1/2} \quad [4]$$

This formalism is valid for Li insertion into single-crystal anatase.[5,6] However, for polycrystalline electrodes, the I-$t^{-1/2}$ curves deviate from the Cottrell-like behavior, and we observe typical S-shaped plots[23,27] as in Fig. 4. [Reasonably linear plots, similar to those for single crystals,[5,6] were only reported for Nb-doped TiO_2 (anatase) grown by chemical vapor deposition.[4]] In general, the values of D_{Li} determined on nanocrystalline electrodes by CHA (Eq. 4) are larger by orders of magnitude compared to the values by CV (Eq. 2).[23-25] This was interpreted as an effect of different strengths of electrical field after the potential step,[26] and the discrepancies were smaller in single-crystal electrodes.[5,6] Analogously, the rate constants (k_0) (Eq. 3) decrease for anatase nanocrystals by orders of magnitude[22,28] compared to the values of single crystal.[5,6]

Despite these limitations, Eq. 2 and 4 provide two independent techniques for the determination of D_{Li} and the comparison of materials. Chronoamperometric diffusion coefficients calculated from the steepest linear parts of I vs $t^{-1/2}$ (cf. Fig. 4) are presented in Table I. They attain higher values for ANA001 again but are uniformly 4 orders of magnitude higher compared to D_{Li} obtained from CV (cf. Ref. 4, 23, 24, and 26 and the discussion above). In addition to this interpretation,[4,23,24,26] we should also consider different conditions of data collection in both methods. The steepest part of the chronoamperometric plot (Fig. 4) represents ~40 s of Li insertion into already conductive (partially lithiated) but not fully charged host material. CV of Li insertion at a scan rate of 0.1 mV/s reaches its insertion current maximum after ca. 2 h. At that time, the host material is charged on half of its nominal capacity and the stress induced by the repulsion of Li^+–Li^+ occupying neighboring vacancies can take place and hinder diffusion in nanosized particles.

The enhanced electrochemical activity of ANA001 as compared to that of C240 is a synergic consequence of both the faster bulk diffusion in the direction parallel to the c-axis and the interfacial charge-transfer kinetics. However, we can distinguish the contributions of each effect from our data if we describe the electrochemical activity by the current density on the particular material in the given method. Then, the diffusion-driven improvement (Eq. 2 and 4 and Table I) can be estimated as

$$\sqrt{\frac{D_{Li,ANA001}}{D_{Li,C240}}} \approx 1.3 \quad \text{(from CV data)}$$

$$\sqrt{\frac{D_{Li,ANA001}}{D_{Li,C240}}} \approx 1.7 \quad \text{(from CHA data)}$$

and the kinetics-driven improvement (Eq. 3 and Table I) as

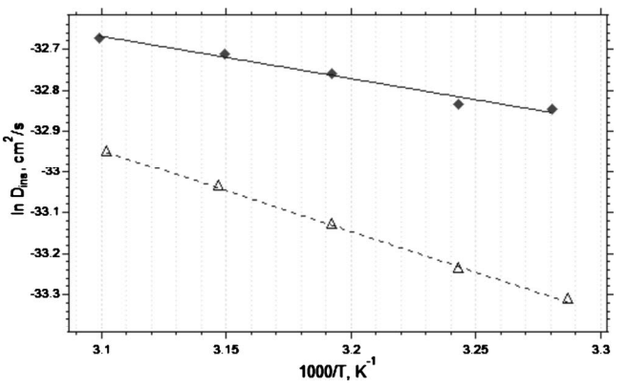

Figure 5. Dependence of solid-state diffusion coefficients for Li^+ insertion on temperature. Coefficients calculated from chronoamperometric data for ANA001 (solid lines, full squares) and C240 (dashed lines, open triangles) are plotted according to Eq. 5. The steeper slope of the fit for C240 (dashed lines) than for ANA001 indicates higher activation energy of C240.

$$\frac{k_{0,\mathrm{ANA001}}}{k_{0,\mathrm{C240}}} \approx 1.7$$

Obviously, the interfacial charge transfer is facilitated on the (001) surface similarly as the bulk diffusion of Li^+ in the direction perpendicular to (001).

To address not only the kinetic aspects of Li insertion into polycrystalline TiO_2 anatase with a predominant (001) face but also the thermodynamics of the process, the temperature dependence of D_{Li} was studied (Fig. 5).

The diffusion coefficients follow the Arrhenius-type temperature dependence

$$D = D_0 \exp\left(\frac{-E_a}{kT}\right) \qquad [5]$$

where E_a is the activation energy. From Fig. 5, we can estimate the activation energy for Li insertion to be 0.1 and 0.2 eV for ANA001 and C240, respectively (Table I). The values are smaller than those predicted theoretically by ab initio calculations[4] (from 0.6 to 0.7 eV) and verified experimentally for single crystals[5] (ca. 0.5 eV). They are well comparable to bulk activation energies determined by ^{7}Li-NMR; the reported values were 0.2 eV for Li-poor anatase and 0.09 eV for Li-rich lithium titanate.[29] The lowering of the activation barrier for nanocrystalline materials might be a consequence of defects and surface states. Also, the strain induced at the phase and/or particle boundaries plays a role in determining the charge-transfer rate on anatase.[30] The contribution of particle morphology, that is, the (001)-rich particles vs the (101)-rich particles, toward the strain penalty cannot be quantified at this stage of research. Nevertheless, we again trace a smaller activation barrier for our ANA001. Hence, all methods reported above confirmed in unison that the Li-insertion activity of ANA001 is better, that is, the (001) face is more active than the (101) face. This supports the earlier results from single crystals but, particularly, the E_a values for both crystal orientations were similar on macroscopic single-crystal electrodes.[5]

For further illustration of the morphology/activity dependence, we have tested another reference material (P90) (Degussa, S_{BET} = 100 m^2/g) at the same conditions, and the corresponding data are summarized in Table I. Generally, the results are very similar to those of C240.

Both CV and CHA data confirm a more facile Li insertion into polycrystalline TiO_2 anatase with a predominant (001) face. These results perfectly agree with previously published works on single-crystal anatase electrodes and prove that Li insertion in anatase with a predominant (001) face is facilitated in polycrystalline materials too.

Conclusion

CV and CHA of Li insertion into polycrystalline TiO_2 anatase with a predominant (001) face proved its higher activity toward Li insertion compared to that of reference materials (C240 and P90). The lithium diffusion coefficient of ANA001 calculated from CV is by 1 order of magnitude higher than those of both reference materials with a dominating (101) face. The same tendency, although not so large difference, exhibited the chronoamperometric diffusion coefficients and rate constants of ANA001, C240, and P90. The enhanced activity of the anatase (001) face for Li insertion stems from synergic contributions of a faster interfacial charge transfer at this surface and a facile Li transport within a more open structure of the anatase lattice in the direction parallel to the *c*-axis. The presented study represents an upgrade of previously published results on single-crystal anatase electrodes. The main new finding of this work is the proof that the crystal morphology, rather than F termination of the surface, is decisive for the improved Li-insertion behavior.

Acknowledgment

This work was supported by the Czech Ministry of Education, Youth and Sports (contract no. LC-510) and by the Academy of Sciences of the Czech Republic (contract IAA 400400804 and KAN 200100801).

J. Heyrovský Institute of Physical Chemistry assisted in meeting the publication costs of this article.

References

1. M. Wagemaker, A. P. M. Kentgens, and F. M. Mulder, *Nature (London)*, **418**, 397 (2002).
2. M. Wagemaker, G. J. Kearley, A. A. van Well, H. Mutka, and F. M. Mulder, *J. Am. Chem. Soc.*, **125**, 840 (2003).
3. T. Brezesinski, J. Wang, J. Polleux, B. Dunn, and S. H. Tolbert, *J. Am. Chem. Soc.*, **131**, 1802 (2009).
4. S. Lunell, A. Stashans, H. Lindström, and A. Hagfeldt, *J. Am. Chem. Soc.*, **119**, 7374 (1997).
5. R. Hengerer, L. Kavan, P. Krtil, and M. Grätzel, *J. Electrochem. Soc.*, **147**, 1467 (2000).
6. L. Kavan, M. Grätzel, S. E. Gilbert, C. Klemenz, and H. J. Scheel, *J. Am. Chem. Soc.*, **118**, 6716 (1996).
7. L. Kavan, *Adv. Sci. Technol. (Faenza, Italy)*, **51**, 20 (2006).
8. M. Kawakita, J. Kawakita, Y. Sakka, and T. Shinohara, *J. Electrochem. Soc.*, **157**, H65 (2010).
9. H. G. Yang, C. H. Sun, S. Z. Qiao, J. Zou, G. Liu, S. C. Smith, H. M. Cheng, and G. Q. Lu, *Nature (London)*, **453**, 638 (2008).
10. L. Kavan, M. Grätzel, J. Rathousky, and A. Zukal, *J. Electrochem. Soc.*, **143**, 394 (1996).
11. L. Kavan, M. Zukalova, M. Kalbac, and M. Grätzel, *J. Electrochem. Soc.*, **151**, A1301 (2004).
12. L. Kavan, T. N. Murakami, P. Comte, and M. Grätzel, *Electrochem. Solid-State Lett.*, **10**, A85 (2007).
13. C. L. Olson, J. Nelson, and M. S. Islam, *J. Phys. Chem. B*, **110**, 9995 (2006).
14. B. Wu, C. Guo, N. Zheng, Z. Xie, and G. D. Stucky, *J. Am. Chem. Soc.*, **130**, 17563 (2008).
15. X. Han, Q. Kuang, M. Jin, Z. Xie, and L. Zheng, *J. Am. Chem. Soc.*, **131**, 3152 (2009).
16. D. Zhang, G. Li, X. Yang, and J. C. Yu, *Chem. Commun. (Cambridge)*, **2009**, 4381.
17. J. S. Chen and X. W. Lou, *Electrochem. Commun.*, **11**, 2332 (2009).
18. H. G. Yang, G. Liu, S. Z. Qiao, C. H. Sun, Y. G. Jin, S. C. Smith, J. Zou, H. M. Cheng, and G. Q. Lu, *J. Am. Chem. Soc.*, **131**, 4078 (2009).
19. C. Barbé, F. Arendse, P. Comte, M. Jirousek, F. Lenzmann, V. Shklover, and M. Grätzel, *J. Am. Ceram. Soc.*, **80**, 3157 (1997).
20. M. Grätzel, *Prog. Photovoltaics*, **14**, 429 (2006).
21. L. Kavan, R. Bacsa, M. Tunckol, P. Serp, S. M. Zakeeruddin, F. Le Formal, M. Zukalova, and M. Grätzel, *J. Power Sources*, **195**, 5360 (2010).
22. L. Kavan, A. Attia, F. Lenzmann, S. H. Elder, and M. Grätzel, *J. Electrochem. Soc.*, **147**, 2897 (2000).
23. L. Kavan, J. Rathousky, M. Grätzel, V. Shklover, and A. Zukal, *J. Phys. Chem. B*, **104**, 12012 (2000).
24. H. Lindström, S. Södergen, A. Solbrand, H. Rensmo, J. Hjelm, A. Hagfeldt, and S. E. Lindquist, *J. Phys. Chem. B*, **101**, 7710 (1997).

25. H. Lindström, S. Södergen, A. Solbrand, H. Rensmo, J. Hjelm, A. Hagfeldt, and S. E. Lindquist, *J. Phys. Chem. B*, **101**, 7717 (1997).
26. R. van de Krol, A. Goossens, and J. Schoonman, *J. Phys. Chem. B*, **103**, 7151 (1999).
27. L. Kavan, J. Prochazka, T. M. Spitler, M. Kalbac, M. Zukalova, T. Drezen, and M. Grätzel, *J. Electrochem. Soc.*, **150**, A1000 (2003).
28. A. Attia, M. Zukalova, J. Rathousky, A. Zukal, and L. Kavan, *J. Solid State Electrochem.*, **9**, 138 (2005).
29. M. Wagemaker, R. van de Krol, A. P. M. Kentgens, A. A. van Well, and F. M. Mulder, *J. Am. Chem. Soc.*, **123**, 11454 (2001).
30. M. Wagemaker, W. J. H. Borghols, and F. M. Mulder, *J. Am. Chem. Soc.*, **129**, 4323 (2007).

Appendix 2

Barbora Laskova, Marketa Zukalova, Arnost Zukal, Milan Bousa and Ladislav Kavan. "Capacitive Contribution to Li-storage in TiO_2 (B) and TiO_2 (anatase)." *Journal of Power Sources*, 2014, **246**, 103-109.

Journal of Power Sources 246 (2014) 103–109

Contents lists available at ScienceDirect

Journal of Power Sources

journal homepage: www.elsevier.com/locate/jpowsour

Capacitive contribution to Li-storage in TiO_2 (B) and TiO_2 (anatase)

Barbora Laskova [a,b], Marketa Zukalova [a], Arnost Zukal [a], Milan Bousa [a,b], Ladislav Kavan [a,b,*]

[a] J. Heyrovsky Institute of Physical Chemistry of the ASCR, v. v. i., Dolejskova 2155/3, CZ-182 23 Prague 8, Czech Republic
[b] Department of Inorganic Chemistry, Faculty of Science, Charles University, Hlavova 2030/8, CZ-128 43 Prague 2, Czech Republic

HIGHLIGHTS

- Capacitive parts of cyclic voltammograms of Li-storage were deconvoluted.
- TiO_2 (B) has by 30% larger capacitive contribution than anatase.
- The capacitive Li-storage in TiO_2 (B) occurs in bulk crystal.

GRAPHICAL ABSTRACT

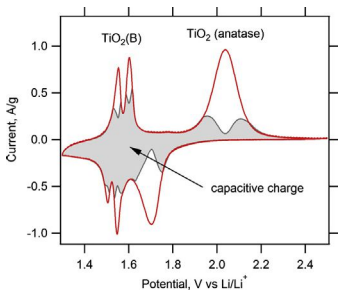

ARTICLE INFO

Article history:
Received 23 May 2013
Received in revised form
29 June 2013
Accepted 17 July 2013
Available online 25 July 2013

Keywords:
Titanium dioxide
TiO_2 (B)
Li-insertion
Cyclic voltammetry
Capacitive charging

ABSTRACT

Analysis of cyclic voltammograms of Li insertion into TiO_2 (B) and anatase provides information about capacitive contributions to overall charge of Li-storage. The enhancement of 30% is found in capacitive contributions (normalized to the total stored charges) in TiO_2 (B) compared to that in anatase, in spite of ca. three times smaller surface area of the former. Different charging mechanism explains facilitated Li^+ insertion in TiO_2 (B). The difference is caused mainly by pseudocapacitive Li-storage in the bulk TiO_2 (B). Deconvolution of cyclic voltammograms also indicates different capacitive contributions of the two voltammetric peaks, S1 and S2 of TiO_2 (B). These results provide novel insight into the Li-storage in TiO_2 (B) and its difference from that in anatase.

1. Introduction

TiO_2 (anatase) and TiO_2 (B) are attractive candidates for anodes in rechargeable Li-ion batteries, due to their low cost, non-toxicity, cycling stability at high charging rate, reasonable capacity and higher operating potential as compared to that of graphite anode [1–8]. The higher Li-insertion potential offers enhanced safety, and prevents formation of lithium dendrites in the battery, albeit at the expense of smaller energy density. The maximal Li-insertion coefficient x (in Li_xTiO_2) is usually close to 0.5 for anatase [9–11], but larger reversible capacities, $x \approx 0.8$ were also reported in certain anatase nanostructures [12–14]. Similar or even larger insertion coefficients were obtained for TiO_2 (B) [1–4,13–18]. The classical synthetic protocols for TiO_2 (B) [19–21] were modified to improve the capacity and charging rate [22–25]. TiO_2 (B) was prepared in the form of nanowires [22,23] ($x = 0.91$), nanoribbons ($x = 0.84$) [26], mesoporous TiO_2 (B) [27], nanoparticles and nanosheets ($x = 0.7–0.8$) [25,28].

* Corresponding author. J. Heyrovsky Institute of Physical Chemistry of the ASCR, v. v. i., Dolejskova 2155/3, CZ-182 23 Prague 8, Czech Republic. Tel.: +420 2 6605 3975; fax: +420 2 8659 2307.
E-mail address: kavan@jh-inst.cas.cz (L. Kavan).

0378-7753/$ – see front matter © 2013 Elsevier B.V. All rights reserved.
http://dx.doi.org/10.1016/j.jpowsour.2013.07.073

TiO_2 (B) is metastable modification of titanium dioxide, adopting the monoclinic structure, space group $C2/m$, lattice parameters: $a = 12.127$ Å, $b = 3.7537$ Å, $c = 6.535$ Å, $\beta = 107.16°$ [29]. Zukalova et al. [21] found that Li-insertion into TiO_2 (B) is characterized by unusually large faradaic pseudocapacitance. This peculiar effect was ascribed to Li^+ accommodation in open channels of TiO_2 (B) structure allowing fast Li-transport in TiO_2 (B) lattice along the *b*-axis (perpendicular to (010) face). The presence of several lithium insertion sites inside the channels of the TiO_2 (B) structure was predicted by theoretical calculations, but significant contradictions remain about the relative accessibility of these sites [24,30–33]. Another peculiarity follows from the existence of two surface-like voltammetric peaks (S1 and S2, with formal potentials of 1.52 and 1.59 V, respectively [21]) in the cyclic voltammogram of TiO_2 (B), as theory predicts three different sites (labeled A1, A2 and C [7,18,24,28,30,31,34,35], or A, B, C [32]) in the TiO_2 (B) structure, where Li can be accommodated. Furthermore, the Li-insertion into the lowest-energy site might also be mismatched with anatase impurity in a sample [24,31]. Therefore deeper insight into charging mechanisms in TiO_2 (B) is still needed.

The charge equivalent of Li-ion storage in TiO_2 is superposition of diffusion-controlled Li-insertion in the bulk crystal and capacitive contribution of double-layer charging. The capacitive charging is important particularly for nanocrystalline TiO_2 materials, due to their large surface areas. Specific questions arise from the pseudocapacitive Li-storage in TiO_2 (B), which is assumed to occur in the bulk crystal [21]. Here we present a detailed voltammetric analysis of lithium insertion to compare the charging mechanisms of TiO_2 (B) and anatase. To this purpose, we adopted the method developed by Dunn et al. [36,37]. The overall stored charge was separated into the contribution from fast processes assigned to capacitive and/or pseudocapacitive ones, and contribution from diffusion-controlled Li-insertion into the bulk [11,36–38].

2. Experimental section

2.1. Materials

TiO_2 (B) was synthesized using a method previously reported by Zukalova et al. [21]. Briefly, 10 g of amorphous TiO_2 was mortared with 7.8 g of Cs_2CO_3 (Aldrich). This powder was then calcined at 800 °C for 4 h, mortared again, and heated to 800 °C in a crucible with a tight lid for 48 h to form cesium titanate. Excess of 1 M HCl was added to the solid and stirred vigorously for 4 × 24 h with the fresh acid exchanged every 24 h. The product was finally dried in air. To optimize the synthetic conditions for high crystallinity and phase purity of TiO_2 (B), this precursor was annealed stepwise in the temperature range 100–1000 °C on the Pt stage of X-ray diffractometer. The diffractogram was measured in situ immediately after each 100 °C step, and by the comparison of particular diffractograms with the JCPD diffraction pattern No. 35-0088, the optimum heat treatment conditions were found to be 500 °C for 1 h in air. The Brunauer–Emmett–Teller (BET) surface area of the product was $S_{BET} = 28$ m^2 g^{-1}. The material is further coded HTi19. For comparison was used a reference anatase sample coded C240 [10]. It is a nanocrystalline anatase with S_{BET} of 89 m^2 g^{-1}, prepared by hydrolysis of titanium tetra(isopropoxide) and hydrothermal recrystallization at 240 °C in autoclave [10,39]. The morphology of C240 is characterized by particles ca. 10–20 nm in size exposing mainly the (101) facets [40]. The titanium dioxide P90 (from Degussa AG, Germany) was a second reference material. This powder had a BET area of 90 m^2 g^{-1} (rutile/anatase mixture with >90% anatase, average anatase particle size 13 nm and very small amount of TiO_2 (B)) [41]. Another material for comparison (denoted N21) was a sample obtained from SusTech GmbH & Co. KG, Darmstadt, Germany. Its synthesis was described elsewhere [42]. Briefly, 8 mL of $TiCl_4$ was dissolved in 20 mL of water and 10 M NaOH was added to a total volume of 150 mL. The mixture was autoclaved at 250 °C for 6 h. Subsequently, the material was washed with hydrochloric acid and water and further autoclaved in water or weak acidic solvents for up to several hours. The concentrations of TiO_2 (B) and anatase phases were determined from powder X-ray diffraction (XRD) according to a method developed by Zhang et al. [43]. The N21 powder contained 49% TiO_2 (B), 51% anatase and had surface area $S_{BET} = 43$ m^2 g^{-1} [42].

2.2. Preparation of electrodes

The powder samples were sonicated in ethanol. Titanium grid (5 × 25 mm^2, Goodfellow) was used as the electrode support. The electrodes were prepared by dip-coating and the coated area was 5 × 10 mm^2 leaving uncovered edge for electrical contact. The electrodes were dried in air and then sintered in air at 450 °C for 30 min. The final mass of active material on a grid was adjusted between 0.30 and 0.62 mg. Blank experiments with Ti-grids annealed at the same conditions proved a negligible electrochemical charge capacity of the Ti grid compared to that of the active material.

2.3. Methods

Electrochemical measurements were carried out in a one-compartment cell using Autolab Pgstat-30 (Ecochemie) controlled by the GPES-4 software. $LiN(CF_3SO_2)_2$ (Fluka) was dried at 130 °C/1 mPa. Ethylene carbonate (EC) and 1,2-dimethoxyethane (DME) were dried over the 3 Å molecular sieve (Fluka). The electrolyte solution was 1 M $LiN(CF_3SO_2)_2$ in EC + DME (1/1 v/v). The reference and counter electrodes were from Li metal, hence, all potentials were quoted against the Li/Li^+ reference electrode in this medium. All electrochemical measurements were carried out under argon atmosphere in a glove box. The BET surface areas of the prepared materials were determined from nitrogen adsorption isotherms at 77 K using the Micromeritics ASAP 2020 instrument. The X-ray diffraction (XRD) was investigated on powder sample by RIGAKU Multiflex diffractometer using CuKα radiation. Raman spectra were measured on Micro Raman (LabRAM HR, Horiba Jobin-Yvon) with 633 nm excitation. Microscope (Olympus BX, objective 50×) allowed focusing laser beam on different grains of the solid material to test the homogeneity of studied sample. Scanning electron microscopy (SEM) images were obtained using a Hitachi field-emission-scanning electron microscope S-4800.

3. Results and discussion

The powder X-ray diffraction pattern of the as-prepared TiO_2 (B) (sample HTi19) is shown in Fig. 1a. The diffractogram confirms the presence of TiO_2 (B), monoclinic metastable polymorph of TiO_2 (space group $C2/m$, JCPD No. 35-0088). The sample is free from anatase, which is the usual impurity in various TiO_2 (B) materials. However, the main diagnostic diffraction peaks of TiO_2 (B) and anatase overlap. This decreases the sensitivity of phase analysis by XRD, and alternative methods, such as Raman spectroscopy or Li-insertion electrochemistry, are needed to test the sample purity [21] (see below). Raman spectrum of HTi19 (Fig. 1b) shows vibrational features of pure TiO_2 (B) without any features of anatase [21,22,25,27–29,44–47]. The centrosymmetric ($C2/m$) structure of TiO_2 (B) with four formula units in the primitive cell corresponds to 18 Raman-active vibration modes, $12A_g + 6B_g$. A comparison of theoretically calculated [29] and our experimental spectrum allows tentative assignment, which is labeled in Fig. 1b. Scanning electron

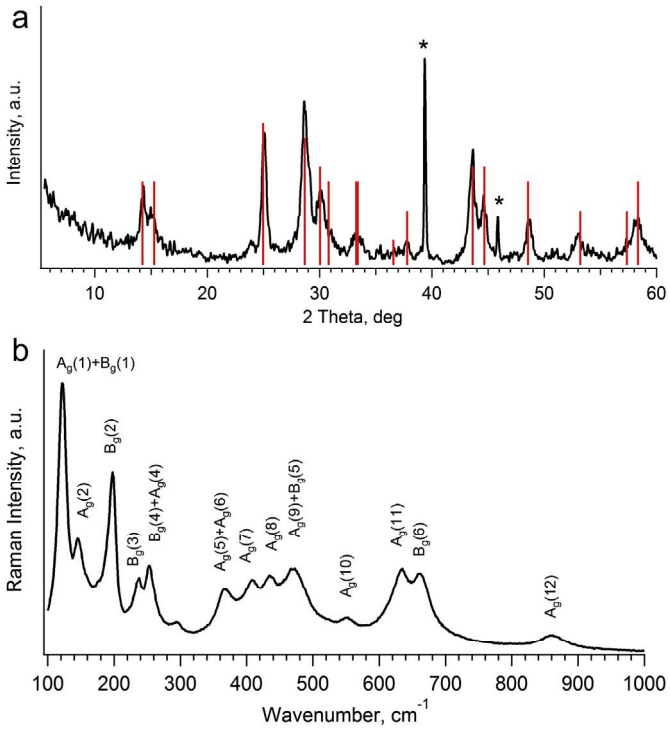

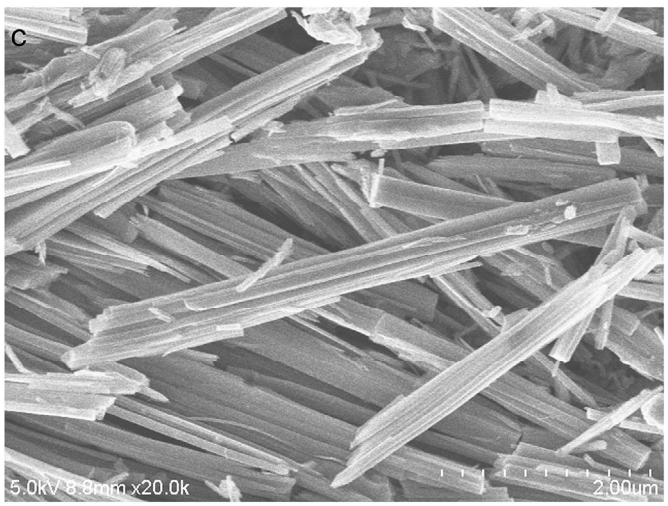

Fig. 1. The X-ray diffraction pattern (a), Raman spectrum (b) and SEM image (c) of HTi19 sample. The red lines in diffractogram (a) correspond to the diffraction pattern JCPD No. 35-0088. Diffraction peaks marked by asterisks arise from Pt sample stage. (For interpretation of the references to color in this figure legend, the reader is referred to the web version of this article.)

microscopy (SEM) image shown in Fig. 1c confirms fibrous texture, characteristic for TiO_2 (B) materials [21]. Adsorption isotherms of nitrogen at 77 K of the sample HTi19 and all three reference materials are presented in Fig. 2. The BET surface area of particular samples was calculated from the part of corresponding isotherm in the range of relative pressures 0.05–0.25.

Electrochemical properties were studied by cyclic voltammetry (CV) of Li-insertion. The absence of any features assignable to the Li insertion/extraction to/from anatase at ca. 1.7 V and 2.0 V, respectively (Fig. 3a) further confirms the phase purity of our HTi19 sample. The voltammogram of TiO_2 (B) exhibits two pairs of peaks labeled S1 and S2. This notation was introduced by us in Refs. [21,48,49] and adopted by others [7,8,50,51] to stress the

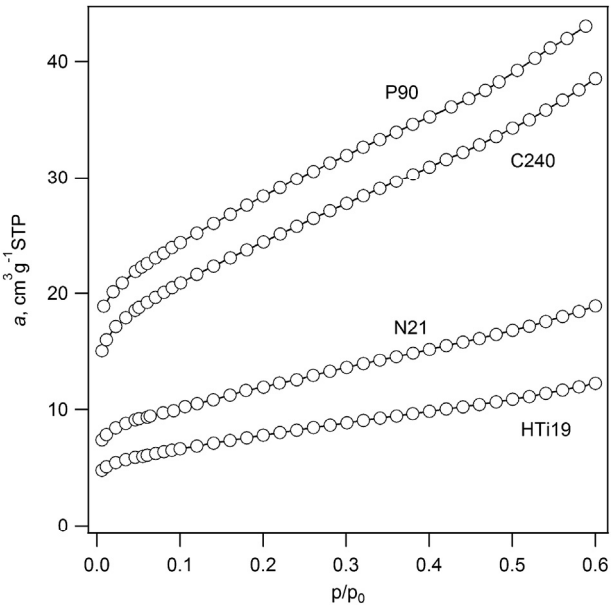

Fig. 2. Adsorption isotherms of nitrogen at 77 K of TiO_2 (B) (sample HTi19), anatase reference materials (samples C240, P90) and TiO_2 (B)/anatase composite (sample N21).

'surface-confined' nature of these peaks. It manifests itself by (i) very small (<59 mV) cathodic/anodic peak-to-peak splitting and (ii) the first-power dependence of peak current (i_p) on the scan rate (v), which is diagnostic for capacitive charging [7,8,18,21,50,51]. However, some authors also reported on the square-root dependence ($i_p \approx v^{1/2}$), indicating the diffusion-controlled charging in S1/S2 peaks [35] or both possibilities [27], and the solid-state Li-diffusion coefficients of the order of 10^{-14} to 10^{-16} cm^2 s^{-1} were calculated based on this assumption. To address these conflicting issues, cyclic voltammetry of the Li^+ insertion into HTi19 and into three reference materials (C240, P90, N21) was analyzed in detail according to the previously reported method [36–38]. The current response at a fixed potential can be expressed by:

$$i(V) = k_1 v + k_2 v^{1/2} \quad (1)$$

where $k_1 v$ corresponds to the capacitive current contribution associated with the storage of Li^+ at the TiO_2 surface and also to the bulk faradaic pseudocapacitance, specific for TiO_2 (B) [21]. The second term $k_2 v^{1/2}$ corresponds to the diffusion-controlled current, which is attributed to the insertion of Li^+ in the bulk of TiO_2 lattice. Dividing of equation (1) by $v^{1/2}$ leads to:

$$\frac{i(V)}{v^{1/2}} = k_1 v^{1/2} + k_2 \quad (2)$$

By linear fitting of measured voltammetric currents, at each specific potential, it is possible to determine the coefficients k_1 and k_2, and to distinguish between the contribution of capacitive current and diffusion-controlled current.

The electrodes from pure TiO_2 (B) (sample HTi19), anatase (C240, P90) and mixture of both phases (sample N21) were prepared with the same mass of the active material (0.58 ± 0.04 mg) to avoid any inaccuracy in CV data analysis due to different amount of active material on electrode. In addition to this series of experiments, the electrode with 0.3 mg of anatase C240 (coded C240half) was also prepared to test the influence of material mass on the computed capacitive contributions. The peak shift occurring as a result of different sweep rates was neglected and the cyclic

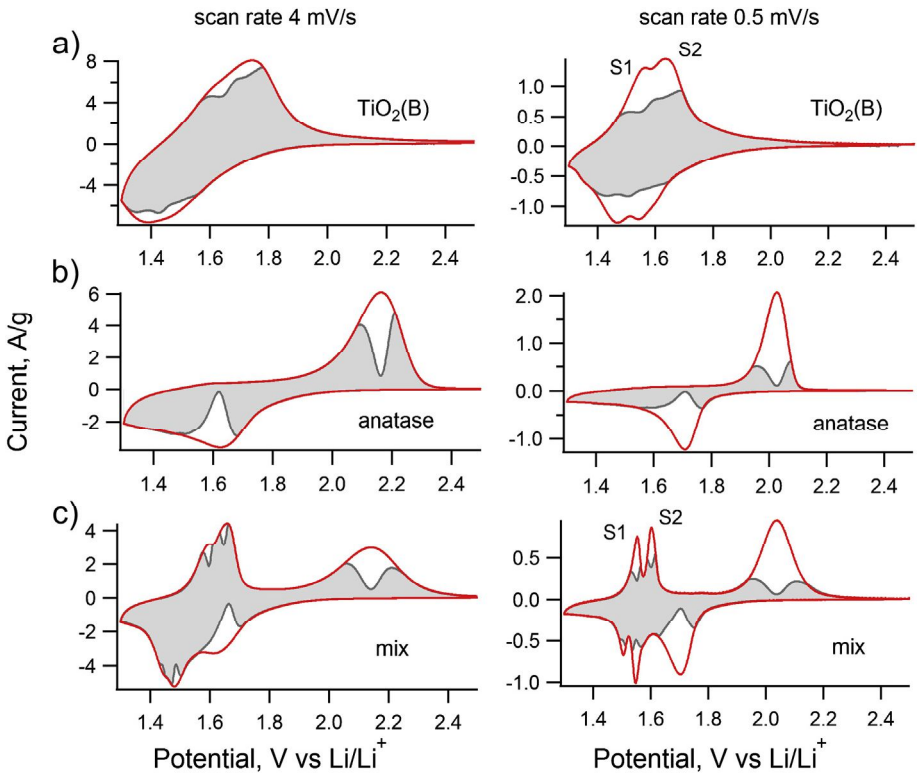

Fig. 3. The cyclic voltammograms of TiO_2 (B) (sample HTi19) (a), anatase (sample C240) (b) and mixture of both phases (sample N21) (c). The voltammograms are displayed for scan rates 4 mV s^{-1} (left charts) and 0.5 mV s^{-1} (right charts). The red lines correspond to experimentally obtained voltammetric currents. The shaded areas represent calculated capacitive contributions. S1 and S2 peaks in TiO_2 (B) are distinguished, particularly at slower scans (right charts a, c). (For interpretation of the references to color in this figure legend, the reader is referred to the web version of this article.)

voltammograms at 0.1 mV s^{-1} were used to define the potential of the current peak maximum [36]. The scan rates in a range of 4 mV s^{-1}–0.1 mV s^{-1} were chosen for analysis since the voltammetric peaks of all studied materials were well distinguishable at these rates. The voltammetric responses of electrodes HTi19, C240 and N21 at scan rates 4 mV s^{-1} and 0.5 mV s^{-1} are shown in Fig. 3 along with the calculated pseudocapacitive contributions to the total charges. Here, we adopted the convention introduced by Dunn et al. [36,37], i.e. the (pseudo)capacitive contribution is represented by shaded area in the voltammograms. To avoid any effect of data processing potential range, all measurements were made in the same way, and quantitative analysis of pseudocapacitive contributions was applied only in a specific range of potentials. To compare correctly all samples, the potential range was set as ±0.16 V from the maximum of the corresponding voltammetric peak. The majority of diffusion contribution (over 99%) occurred in this potential range. For extended potential ranges, only proportionally higher pseudocapacitive currents were observed for all the samples. Fig. 3 indicates that the (pseudo)capacitive charge is dominating in the voltammogram of TiO_2 (B) phase (Fig. 3a), and that of the TiO_2 (B) component in our mixed sample N21 (Fig. 3c) in comparison with that of anatase (sample C240, Fig. 3b).

The comparison of pure TiO_2 (B) and anatase electrodes is particularly interesting as the surface area of our TiO_2 (B) sample is only 28 m^2 g^{-1}, whereas the surface area of our anatase is 89 m^2 g^{-1}, i.e. larger by a factor of about 3. Our finding obviously contradicts the logical conclusion that the capacitive contribution is confined to the surface, i.e. it should scale with surface area (or reverse particle size) of TiO_2 [36]. For anatase electrodes, this was indeed confirmed: the found capacitive contributions were 55, 35, ad 15% for materials having the surface areas of 220, 150 and 50 m^2 g^{-1}, respectively (particles sizes of 7, 10 and 30 nm, respectively) [36]. Our comparison of TiO_2 (B) and anatase evidences that the capacitive Li-storage in TiO_2 (B) is qualitatively different and not confined to the surface only. This supports the idea of faradaic pseudocapacitance in the bulk crystal of TiO_2 (B) as proposed by Zukalova et al. [21].

The calculated contributions of capacitive charge to the overall accommodated Li for extraction peaks at different scan rates are shown in Table 1. The pseudocapacitive contribution for TiO_2 (B) (sample HTi19) is still high at the scan rate 0.5 mV s^{-1}. This contribution represents 68% of the total charge and matches well the result for the TiO_2 (B) peaks in the CV of mixed sample N21, which is 72%. The capacitive contributions for TiO_2 (B) are by about

Table 1
Comparison of capacitive charge storage contribution to the total stored charge for phase pure TiO_2 (B) material (HTi19); anatase reference samples (C240, P90); the anatase component in N21 (N21anatase) and the TiO_2 (B) component in N21 (N21TiO_2 (B)). C240half denotes the results for anatase electrode with mass of active material of 0.3 mg. The individual charges Q^{+}_{cap}, Q^{-}_{cap}, Q^{+}_{diff}, Q^{-}_{diff} were determined for scan rate of 0.5 mV s^{-1}.

Scan rate		HTi19	C240	C240 half	P90	N21 anatase	N21TiO_2 (B)
4 mV s^{-1}	Capacitive contribution (%)	89	68	69	71	67	89
0.5 mV s^{-1}	Capacitive contribution (%)	68	37	38	41	38	72
	Q^{+}_{cap} (C g^{-1})	426	162	154	189	241[a]	
	Q^{+}_{diff} (C g^{-1})	199	273	249	273	211[a]	
	Q^{-}_{cap} (C g^{-1})	447	167	152	181	324[a]	
	Q^{-}_{diff} (C g^{-1})	177	260	215	265	133[a]	

[a] Total charge integrated for anatase and TiO_2 (B) components of the N21 sample.

30% higher than the same contributions for anatase (samples C240, P90) and the anatase peak in the voltammogram of N21 at 0.5 mV s^{-1}. These results agree with data evaluated for the C240 electrode with lower active mass. Hence, the 30% enhancement of capacitive contributions in TiO_2 (B) (referred to that in anatase) is independent on the amount of electrode material. It can be also deduced that the particle size of anatase crystals in material N21 is close to that in C240 and P90 samples because of their similar capacitive contributions [36].

For the given range of potentials the overall charge storage in pure anatase (C240 and P90) at scan rate 0.5 mV s^{-1} was 435 C g^{-1} and 462 C g^{-1} respectively. The total stored charge 625 C g^{-1} in pure TiO_2 (B) material (HTi19) was by ca. 27% higher than that in anatase. Considering the error of CV deconvolution to be ca. 10% [36], then the observed difference in overall charge storage is close to the calculated one for corresponding capacitive contributions. The voltammetric charges normalized to BET surface area equal 4.9 and 5.1 C m^{-2} for C240 and P90, respectively, but 22.3 C m^{-2} for pure TiO_2 (B), sample HTi19. These results indicate, that previously discussed fast Li^+ insertion into TiO_2 (B) and its higher Li insertion coefficient (x) [21,23,27,42,52] are caused by higher level of pseudocapacitive charge storage. Table 1 further compiles the actual anodic and cathodic charges (Q^+_{cap} and Q^-_{cap}) corresponding to capacitive charge storage and analogous quantities for diffusion-controlled charge storage (Q^+_{diff} and Q^-_{diff}) at the scan rate of 0.5 mV s^{-1}. Reasonably symmetrical charging/discharging is observed for both types of contributions in phase-pure samples, i.e. in HTi19, C240 and P90. The bi-modal sample, N21, does not allow accurate distinction of charges assignable to each individual phase, because of overlapping voltammetric features of TiO_2 (B) and anatase. Nevertheless the total voltammetric charge of N21 shows again good symmetry: $Q^+_{cap} + Q^+_{diff} = 452$ C g^{-1}; $Q^-_{cap} + Q^-_{diff} = 457$ C g^{-1}.

The lithium ion can be accommodated at three specific sites inside TiO_2 (B) structure labeled A1, A2 and C (using the more common coding, see above) [18,24,28,30–32,34,35]. The A1 and A2 sites are localized close to equatorial oxygen atoms of the TiO_6 octahedra and are both 5-fold coordinated; the C site is 4-fold coordinated by axial (bridge) oxygen atoms and sits near the middle of the open *b*-axis channel. From our results and these computations we suppose that there is a substantial pseudocapacitive process in TiO_2 (B) connected with accommodation of Li inside the TiO_2 (B) open channels and this process apparently causes the main difference in electrochemical response of TiO_2 (B) and anatase. This conclusion also supports earlier experimental works [21,27]. The capacitive contribution was reported by Dunn et al. [36,37] to be inversely proportional to a particle size of anatase. In our case, the anatase materials had particle size about 10–20 nm and BET surface area close to 90 m^2 g^{-1}. The TiO_2 (B) fibers had three times lower BET surface area ($S_{BET} = 28$ m^2 g^{-1}) and a length in the order of μm. In spite of their so large aspect ratio and difference in size, the TiO_2 (B) samples still have a significantly larger pseudocapacitive contribution to overall charge storage. This further highlights the influence of morphology and open channels in TiO_2 (B) structure on its improved electrochemical charge storage capacity.

The supposed overall deviation of contributions given by CV deconvolution process is up to 10% [36], nevertheless, the observed deviation of contributions was different for each potential and it was minimal at potential corresponding to the current peak (<1%). The contribution of Li^+ diffusion process has the highest value at the potential of current peak too and thus the most pronounced difference in the ratio of capacitive contributions to the total current can be expected at potentials of the current maxima for all the samples. Therefore the capacitive/diffusion contributions at potentials corresponding to the current maxima of extraction peaks of all the samples were investigated separately. Both types of contributions at the current peak maxima for different scan rates were calculated by procedure described above.

Fig. 4 shows computed pseudocapacitive current ($k_1 \cdot \nu$) and diffusion-controlled current ($k_2 \cdot \nu^{1/2}$) as a function of the scan rate for the extraction peaks of HTi19 and C240. The current connected with Li^+ extraction from the bulk predominates over capacitive current for each scan rate more than five times in anatase (C240, Fig. 4a). On the other hand the pseudocapacitive current dominates to the total current until the scan rate of 0.5 mV s^{-1} for both peaks (S1 and S2 [21]) in CVs of HTi19 (see Fig. 4b and c). This high contribution of capacitive current at the potential of the peak maxima in HTi19 at slow scan rates clearly indicates the high pseudocapacitive storage in this material too [38]. The same conclusion follows from comparison of other anatase-containing materials, P90 and N21. The calculated contributions of the

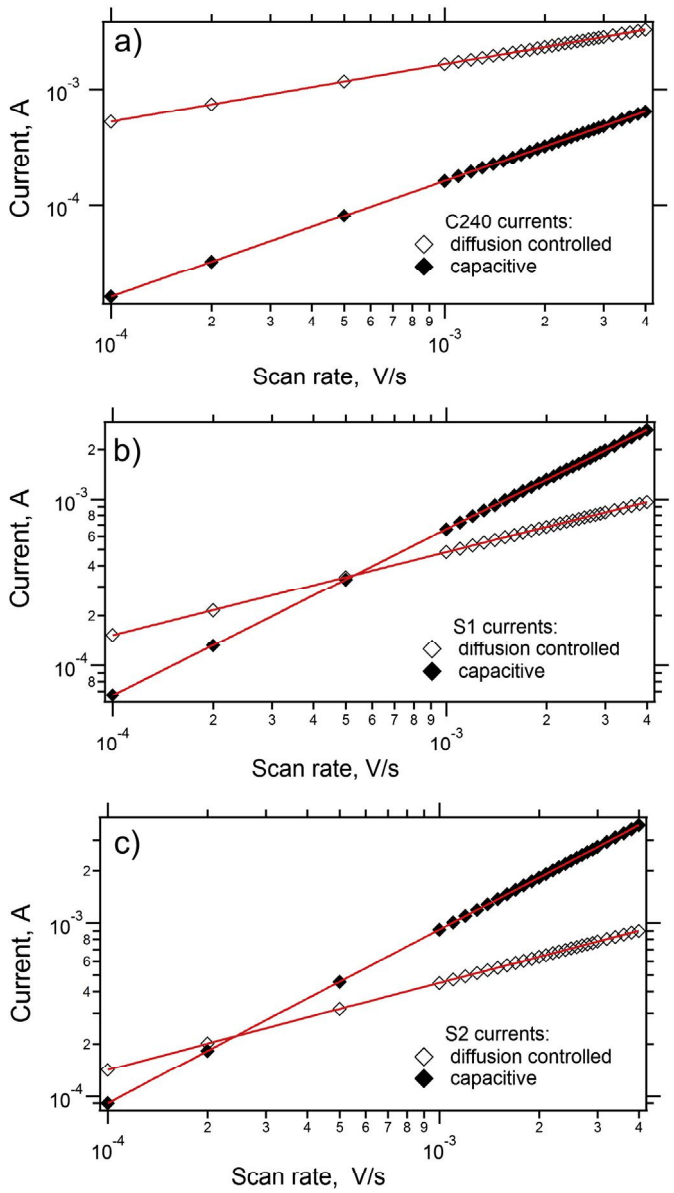

Fig. 4. Dependence of the calculated capacitive currents (full points) and diffusion controlled currents (open points) on scan rate for extraction peak maxima of anatase C240 (a), HTi19 peak at lower potentials S1 (b) and HTi19 peak at higher potentials S2 (c). The red lines represent fits corresponding to $k_1\nu$ for capacitive processes and $k_2\nu^{1/2}$ for diffusion processes, respectively. (For interpretation of the references to color in this figure legend, the reader is referred to the web version of this article.)

Table 2
Comparison of capacitive current contributions to the total current at peak maxima for phase pure TiO_2 (B) material (HTi19), the TiO_2 (B) component in N21 (N21TiO_2 (B)), the anatase reference samples (C240, P90) and the anatase component in N21 (N21anatase). C240half denotes the results for anatase electrode with mass of active material of 0.3 mg. The low-potential extraction peak of TiO_2 (B) is labeled as S1 and higher-potential extraction peak as S2.

	Scan rate	C240	C240half	P90	HTi19		N21TiO_2 (B)		N21anatase
					S1	S2	S1	S2	
Capacitive contribution (%)	4 mV s^{-1}	17	2	21	76	85	62	74	18
	0.5 mV s^{-1}	6	7	8	47	58	32	45	7

capacitive to the total current at the current peak maximum for different scan rates are summarized in Table 2. The data in Table 2 clearly show the capacitive contributions for TiO_2 (B) being of over 30% higher than those for anatase at 0.5 mV s^{-1}. Although there is a small difference in the actual data for pure TiO_2 (B) material HTi19 and the TiO_2 (B) component in N21, the high pseudocapacitive contribution as compared to that of anatase is still evident. For phase-pure sample (HTi19) and anatase samples is this difference even larger than 40%.

Theoretical studies of Li^+ accommodation sites in TiO_2 (B) and their stability were made recently [24,30–32,34]. However, they are contradictory as far as the preferential sites occupancy is concerned [24,31,32,34]. Arrouvel et al. [30] determined C site as the preferential one for Li^+ accommodation at $x < 0.25$, contrary to Dalton et al. [31], who concluded A1 site being more favorable for x lower than 0.5. Koudriachova [34], on the other hand, proposed that pseudocapacitive Li-storage is associated exclusively with the A2 site, but the effect of nanowire morphology also plays a role. Furthermore, the capacitive to overall contribution is lower for the low-potential extraction/insertion peak of TiO_2 (B) (denoted as S1 peak) in comparison with the higher-potential extraction/insertion peak (denoted as S2 peak), (see Figs. 4b, c, and Table 2). This effect is probably a result of saturation of the open *b*-axis channels by Li^+ at lower potentials. It can be assumed, that Li^+ is predominantly accommodated in certain sites at higher potentials and with potential decrease it diffuses from channels to the bulk material simultaneously. Since Li transport along the *b*-axis is faster than insertion into the bulk [30], the channels become almost saturated for potentials under 1.5 V and the decrease of pseudocapacitive contribution is observed for peak S1.

4. Conclusions

The charging mechanism of TiO_2 (B) and anatase during Li^+ insertion was investigated by deconvolution of cyclic voltammograms. The contribution of capacitive charge referred to the total stored charge was found to be over 30% higher in TiO_2 (B) compared to that in anatase nanocrystals, in spite of the factor of 3 smaller surface area of the former. The predominant pseudocapacitive process in TiO_2 (B) was related to accommodation of Li inside the TiO_2 (B) open channels in monoclinic lattice. The main difference in electrochemical response of TiO_2 (B) and anatase is caused by the pseudocapacitive processes in TiO_2 (B). To the best of our knowledge, this conclusion is here quantified for the first time. Moreover, the scan rate dependencies of cyclic voltammetry peak currents revealed different level of capacitive current for two voltammetric peaks (S1, S2) in TiO_2 (B). The capacitive contribution to the overall peak current was higher for voltammetric peak at higher potential (S2). This behavior is ascribed to saturation of open channels in the structure by Li^+ at lower potentials.

Acknowledgment

This work was supported by the Grant Agency of the Czech Republic (contracts No. 13-07724S and P108/12/0814) and by the Czech Ministry of Education Youth and Sports (COST Action CM1104, contract No. LD13060).

References

[1] Z. Yang, D. Choi, S. Kerisit, K.M. Rosso, D. Wang, J. Zhang, G. Graff, J. Liu, J. Power Sources 192 (2009) 588–598.
[2] P.G. Bruce, B. Scrosati, J.-M. Tarascon, Angew. Chem. Int. Ed. 47 (2008) 2930–2946.
[3] M. Wagemaker, F.M. Mulder, Acc. Chem. Res. 46 (2008) 1206–1215.
[4] S.T. Myung, N. Takahashi, S. Komaba, C.S. Yoon, Y.K. Sun, K. Amine, H. Yashiro, Adv. Funct. Mater. 21 (2011) 3231–3241.
[5] B.C. Melot, J.-M. Tarascon, Acc. Chem. Res. 46 (2012) 1226–1238.
[6] Z. Guo, X. Dong, D. Zhou, Y. Du, Y. Wang, Y. Xia, RSC Adv. 3 (2013) 3352–3358.
[7] C. Jiang, J. Zhang, J. Mater. Sci. Technol. 29 (2013) 97–122.
[8] S. Liu, H. Jia, L. Han, J. Wang, P. Gao, D. Xu, J. Yang, S. Che, Adv. Mater. 24 (2012) 3201–3204.
[9] S.Y. Huang, L. Kavan, M. Grätzel, I. Exnar, J. Electrochem. Soc. 142 (1995) L142–L144.
[10] L. Kavan, M. Grätzel, J. Rathousky, A. Zukal, J. Electrochem. Soc. 143 (1996) 394–400.
[11] H. Lindström, S. Södergen, A. Solbrand, H. Rensmo, J. Hjelm, A. Hagfeldt, S.E. Lindquist, J. Phys. Chem. B 101 (1997) 7717–7722.
[12] D. Bresser, E. Paillard, E. Binetti, S. Krueger, M. Striccoli, M. Winter, S. Passerini, J. Power Sources 206 (2012) 301–309.
[13] T. Berger, D. Monllor-Setoca, M. Jankulovska, T. Lana-Villarreal, R. Gomez, Chem. Phys. Chem. 13 (2012) 2824–2875.
[14] L. Kavan, Chem. Rec. 12 (2012) 131–142.
[15] B. Zachau-Christiansen, K. West, T. Jacobsen, S. Skaarup, Solid State Ionics 53–56 (1992) 364–369.
[16] B. Zachau-Christiansen, K. West, T. Jacobsen, S. Atlung, Solid State Ionics 28–30 (1988) 1176–1182.
[17] L. Brohan, R. Marchand, Solid State Ionics 9-10 (1983) 419–424.
[18] A.G. Dylla, G. Henkelman, K.J. Stevenson, Acc. Chem. Res. 46 (2013) 1104–1112.
[19] R. Marchand, L. Brohan, M. Tournoux, Mater. Res. Bull. 15 (1980) 1129–1133.
[20] T. Kasuga, M. Hiramatsu, A. Hoson, T. Sekino, K. Niihara, Langmuir 14 (1998) 3160–3163.
[21] M. Zukalova, M. Kalbac, L. Kavan, I. Exnar, M. Grätzel, Chem. Mater. 17 (2005) 1248–1255.
[22] A.R. Armstrong, G. Armstrong, J. Canales, P.G. Bruce, Angew. Chem. Int. Ed. 43 (2004) 2286–2288.
[23] A.R. Armstrong, G. Armstrong, J. Canales, P.G. Bruce, J. Power Sources 146 (2005) 501–506.
[24] A.R. Armstrong, C. Arrouvel, V. Gentili, S.C. Parker, M.S. Islam, P.G. Bruce, Chem. Mater. 22 (2010) 6426–6432.
[25] M. Kobayshi, V.V. Petrykin, M. Kakihana, Chem. Mater. 19 (2007) 5373–5376.
[26] T. Beuvier, M. Richard-Plouet, M. Mancini-Le Granvalet, T. Brousse, O. Crosnier, L. Brohan, Inorg. Chem. 49 (2010) 8457–8464.
[27] A.G. Dylla, J.A. Lee, K.J. Stevenson, Langmuir 28 (2012) 2897–2903.
[28] A.G. Dylla, P. Xiao, G. Henkelman, K.J. Stevenson, J. Phys. Chem. Lett. 3 (2012) 2015–2019.
[29] M.B. Yahia, F. Lemoigno, T. Beuvier, J.S. Filhol, M.R. Plouet, L. Brohan, M.L. Doublet, J. Chem. Phys. 130 (2009) 204501–20450111.
[30] C. Arrouvel, S.C. Parker, M.S. Islam, Chem. Mater. 21 (2009) 4778–4783.
[31] A.S. Dalton, A.A. Belak, A. Van der Ven, Chem. Mater. 24 (2012) 1568–1574.
[32] D. Panduwinata, J.D. Gale, J. Mater. Chem. 19 (2009) 3931–3940.
[33] T. Okumura, T. Fukutsuka, A. Yanagihara, Y. Orikasa, H. Arai, Z. Ogumi, Y. Uchimoto, Chem. Mater. 23 (2011) 3636–3644.
[34] M.V. Koudriachova, Surf. Interface Anal. 42 (2010) 1330–1332.
[35] C.W. Mason, I. Yeo, K. Saravanan, P. Balaya, RSC Adv. 3 (2013) 2935–2941.
[36] J. Wang, J. Polleux, J. Lim, B. Dunn, J. Phys. Chem. C 111 (2007) 14925–14931.
[37] T. Brezesinski, J. Wang, J. Polleux, B. Dunn, S.H. Tolbert, J. Am. Chem. Soc. 131 (2009) 1802–1809.
[38] K. Zhu, Q. Wang, J.H. Kim, A.A. Pesaran, A.J. Frank, J. Phys. Chem. C 116 (2012) 11895–11899.
[39] C. Barbe, F. Arendse, P. Comte, M. Jirousek, F. Lenzmann, V. Shklover, M. Grätzel, J. Am. Ceram. Soc. 80 (1997) 3157–3171.
[40] M. Grätzel, Prog. Photovolt. Res. Appl. 14 (2006) 429–442.
[41] L. Kavan, R. Bacsa, M. Tunckol, P. Serp, S.M. Zakeeruddin, F. Le Formal, M. Zukalova, M. Grätzel, J. Power Sources 195 (2010) 5360–5369.

[42] L. Kavan, M. Kalbac, M. Zukalova, I. Exnar, V. Lorenzen, R. Nesper, M. Grätzel, Chem. Mater. 16 (2004) 477–485.
[43] H. Zhang, M. Finnegan, J.F. Banfield, Nano Lett. 1 (2001) 81–85.
[44] T. Beuvier, M. Richard-Plouet, L. Brohan, J. Phys. Chem. C 113 (2009) 13703–13706.
[45] B. Santara, P.K. Giri, K. Imakita, M. Fujii, Nanoscale 5 (2013) 5476–5488.
[46] G. Xiang, Y.G. Wang, J. Li, J. Zhuang, X. Wang, Sci. Rep. 3 (2013) 1411–1411-6.
[47] W. Zhuang, L. Lu, X. Wu, W. Jin, M. Meng, Y. Zhu, X. Lu, Electrochem. Commun. 27 (2013) 124–127.
[48] L. Kavan, J. Rathousky, M. Grätzel, V. Shklover, A. Zukal, J. Phys. Chem. B 104 (2000) 12012–12020.
[49] L. Kavan, J. Rathousky, M. Grätzel, V. Shklover, A. Zukal, Micropor. Mesopor. Mater. 44-45 (2001) 653–659.
[50] J. Wang, Y. Zhou, Z. Shao, Electrochim. Acta 97 (2013) 386–392.
[51] H. Zhang, G.R. Li, L.P. An, T.Y. Yan, X.P. Gao, H.Y. Zhu, J. Phys. Chem. C 111 (2007) 6143–6148.
[52] M. Inaba, Y. Oba, F. Niina, Y. Murota, Y. Ogino, A. Tasaka, K. Hirota, \ 189 (2009) 580–584.

Appendix 3

Barbora Laskova, Otakar Frank, Marketa Zukalova, Milan Bousa, Martin Dracinsky and Ladislav Kavan. “Lithium Insertion into Titanium Dioxide (Anatase): A Raman Study with $^{16/18}O$ and $^{6/7}Li$ Isotope Labeling.” *Chem. Mater*, 2013, **25**, 3710-3717.

CHEMISTRY OF MATERIALS

Article

pubs.acs.org/cm

Lithium Insertion into Titanium Dioxide (Anatase): A Raman Study with $^{16/18}O$ and $^{6/7}Li$ Isotope Labeling

Barbora Laskova,[†,‡] Otakar Frank,[†] Marketa Zukalova,[†] Milan Bousa,[†,‡] Martin Dracinsky,[§] and Ladislav Kavan*[,†,‡]

[†]J. Heyrovský Institute of Physical Chemistry, v.v.i. Academy of Sciences of the Czech Republic, Dolejskova 3, 18223 Prague 8, Czech Republic

[‡]Department of Inorganic Chemistry, Faculty of Science, Charles University, Hlavova 2030/8, 12843 Prague 2, Czech Republic

[§]Institute of Organic Chemistry and Biochemistry, v.v.i. Academy of Sciences of the Czech Republic, Flemingovo nam. 2, 16610 Prague 6, Czech Republic

Supporting Information

ABSTRACT: Electrochemical and chemical (with *n*-butyllithium) insertion of Li into TiO_2 (anatase) is studied by Raman spectroscopy and by in situ Raman spectroelectrochemistry. Four isotopologue combinations in the system, namely $^{6/7}Li_xTi^{16/18}O_2$ (with x being the insertion coefficient), are prepared and studied. Spectral assignment is supported by numerical simulations using DFT calculations. The combination of experimental and theoretical Raman frequencies with the corresponding isotopic shifts brings new inputs for several still open questions about the Li-insertion into TiO_2 (anatase).

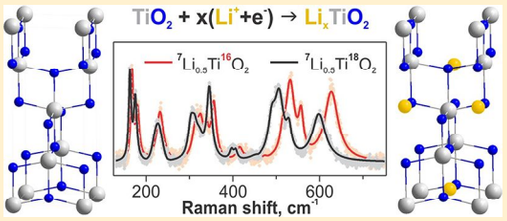

KEYWORDS: *titanium dioxide, lithium insertion, Raman spectroscopy, spectroelectrochemistry*

INTRODUCTION

Lithium insertion into TiO_2 (anatase) attracted considerable attention in the past. It is interesting both for addressing the fundamental questions[1−8] and for its prospective application in Li-ion batteries.[7−12] The reaction is described by the formal equation:

$$TiO_2 + x(Li^+ + e^-) \rightarrow Li_xTiO_2 \quad (1)$$

At a certain level of lithiation ($x \approx 0.5$), the tetragonal anatase TiO_2 (space group $I4_1/amd$, No. 141, lattice constants: a = 3.792 Å, c = 9.497 Å) is converted reversibly to orthorhombic titanate, $Li_{0.5}TiO_2$ (space group *Imma*, No. 74, lattice constants: a = 3.819 Å, b = 4.084 Å c = 9.066 Å). This conversion was first reported by Ohzuku et al.[13] and Cava et al.[14] and confirmed by others.[3−6,15−18] More precisely, the initial stages of Li-insertion were characterized by a coexistence of two phases: a Li-poor tetragonal phase ($x \approx 0.01-0.03$) with an anatase structure, and orthorhombic Li-titanate.[3−5] Ren et al.[16] reported that the growth of orthorhombic titanate started already at x = 0.05, but it was difficult to detect the onset of the nucleation of the orthorhombic phase by X-ray diffraction due to the small size of the nuclei.

Wagemaker et al.[6,19] found another Li-titanate at a deeper lithiation, $LiTiO_2$, but this phase was accessible solely with nanocrystalline (<7 nm in size) TiO_2 hosts. The titanate, $LiTiO_2$, had the same tetragonal structure as the starting anatase ($I4_1/amd$) but with different lattice constants (a = 4.043 Å, c = 8.628 Å). We may note that the previously reported[13] cubic $LiTiO_2$ was not confirmed in subsequent studies,[3−6,14−18,20] and there was also hexagonal $LiTiO_2$ found in yet another study of rutile.[21] With a pure nano-anatase host, the tetragonal structure seems to be the only Li-rich (up to $x \approx 1$) phase in the system.[6] It can be obtained both by chemical lithiation using n-butyllithium[6] and electrochemically.[20] Its detection is not always straightforward. For instance, the mesoporous anatase (~6 nm crystallite size) exhibited solely the orthorhombic Li-titanate up to x = 0.96.[16] Analogously, the $Li_{1.02}TiO_2$ made from anatase nanotubes showed only the weak Raman lines of orthorhombic Li-titanate; hence, the evolution of tetragonal $LiTiO_2$ is hard to detect in this way.[17] Nevertheless, we have quite surprisingly found that almost pure cubic $LiTiO_2$ was formed via the *n*-butyllithium reaction with special titania nanomaterials composed of anatase, TiO_2(B) and a large proportion (91%) of an "amorphous" component under conditions, where pure orthorhombic Li_xTiO_2 grew from an "ordinary" nanoanatase.[22]

Structural data about the Li/TiO_2 system were previously acquired using X-ray[3,23] and neutron diffraction[6,14,24] (the latter is preferred for its greater sensitivity to Li), ^{7}Li NMR[3−5,24] and EXAFS (XANES).[19,20] Raman spectroscopy is another popular technique of choice for structural studies.[15−18,25,26] Because of the sensitive probing of short-range structures, Raman spectroscopy is preferable over diffraction methods for small

Received: June 25, 2013
Revised: August 21, 2013
Published: August 21, 2013

nanocrystals or poorly crystalline materials, which are generated during insertion reactions.[16]

The vibrational lattice dynamics of pure TiO_2 (anatase) has been a subject of several studies.[27−31] The first-order Raman scattering of anatase TiO_2 gives rise to six Raman active vibrations: $A_{1g} + 2B_{1g} + 3E_g$. The experimental and numerically simulated spectra of TiO_2 (anatase) with defined oxygen isotopes (^{18}O, ^{17}O and ^{16}O) provided reasonable agreement of the corresponding isotope shifts of all these vibrations.[30,31] More specifically, the A_{1g} mode was predicted to be a pure oxygen vibration. Hence, the isotope shift of the vibration of the ^{18}O-labeled sample (ν_{18}) referenced to that of the ^{16}O-labeled sample (ν_{16}), which is defined as:

$$\Delta_{1618} = \frac{\nu_{16} - \nu_{18}}{\nu_{16}} \tag{2a}$$

attains its maximal value, ${}^{max}\Delta_{1618}$ for the A_{1g} vibration. It is calculated as follows:

$${}^{max}\Delta_{1618} = 1 - \sqrt{\frac{16}{18}} = 0.057 \tag{2b}$$

On the other hand, the $B_{1g}(1)$ mode in anatase is a pure Ti-atom vibration with no O-isotope shift ($\Delta_{1618} = 0$) and the remaining vibrations are mixes of both O-atom and Ti-atom motions ($0 < \Delta_{1618} < 0.057$).[30,31]

In-situ Raman spectroelectrochemistry is useful for the investigation of the electrochemical doping of anatase[32] and electrochemical Li-insertion.[15−18,25,26] The latter approach was pioneered by Dinh et al.[25] and further extended by Baddour-Hadjean et al.[26] and Hardvick et al.[15] These three initial works reported in unison that Li-insertion caused disappearance of the six anatase Raman lines ($A_{1g} + 2B_{1g} + 3E_g$), which were replaced by novel features attributed to orthorhombic Li-titanate. However, considerable disagreement exists concerning the actual number, positions and spectral assignment of these new lines. More specifically, five lines between 176 and 531 cm^{-1} were reported in ref 25, thirteen lines between 144 and 930 cm^{-1} were reported in ref 26, and fifteen lines between 163 and 636 cm^{-1} were reported in ref 15. The last work predicted, using factor group analysis, nine Raman-active bands: $3A_g + 3B_{2g} + 3B_{3g}$ for the orthorhombic Li_xTiO_2; therefore, six Raman bands (out of the 15 bands observed experimentally) were unassigned.[15] Recently, Gentili et al.[17] reported on 9 lines between 147 and 625 cm^{-1}, but they did not attempt to assign them. (The number of Raman active modes theoretically predicted in ref 15 and experimentally observed in ref 17 seem to be coincidental only.) To our knowledge, there are no Raman data concerning the tetragonal $LiTiO_2$ except for a brief note in ref 17.

To address these open points, we present here a detailed Raman and in situ Raman spectroelectrochemical study of Li-insertion into anatase. To arrive at accurate spectral data, we used a combined theoretical and experimental approach based on DFT calculation and isotope ($^{16/18}O$ and $^{6/7}Li$) labeling for the Raman assignment. In analogy to eqs 2a,2b, the corresponding isotope shifts of Li-vibrations are:

$$\Delta_{67} = \frac{\nu_6 - \nu_7}{\nu_6} \tag{3a}$$

$${}^{max}\Delta_{67} = 1 - \sqrt{\frac{6}{7}} = 0.074 \tag{3b}$$

The strategy of using isotope-labeled samples follows from our earlier theoretical and experimental study of pure TiO_2,[30,31] which is upgraded here by an investigation of both chemical and electrochemical lithiation.

EXPERIMENTAL SECTION AND THEORETICAL METHODS

Materials. The synthesis of TiO_2 samples was carried out in a closed all-glass vacuum apparatus according to our earlier work.[30,31] Briefly, vacuum distilled titanium tetrachloride (99.98% Aldrich) was contacted with $H_2{}^{18}O$ (^{18}O 99%) or ordinary water with natural isotope composition (approximated as $H_2{}^{16}O$). The product was heat-treated in vacuum at 450 °C to obtain an anatase form of TiO_2. Our synthetic protocol obviously eliminates the contamination of the sample by any other oxygen isotopologue, except for the obvious isotopic impurity present in the reagents, that is, in water. The Brunauer−Emmett−Teller (BET) surface area of the product was S_{BET} = 31 m^2/g for both O-isotopologues. The lithium-isotope labeled salt $^6LiClO_4$ (with 95 atom % of ^6Li, Sigma Aldrich) was used as an electrolyte. A common lithium perchlorate (Sigma Aldrich) approximated as $^7LiClO_4$ (natural abundance of ^7Li is 92.5%) was used for comparison. The chemically lithiated titania was prepared using *n*-butyllithium with a natural abundance of ^7Li. To this purpose, TiO_2 powder was stirred in a 1.6 M solution of *n*-butyllithium in hexane (Sigma Aldrich) with a Li/Ti molar ratio of 2.5. The product was washed with hexane and dried. Alternatively, the electrochemically (see below) lithiated titania powder was isolated after the $^6Li^+$ insertion. The treated electrode was washed with ethanol and dried. All operations were carried out in a glovebox under argon.

Preparation of Electrodes. Powder titania samples were dispersed in an aqueous medium into a viscous paste. The powders (2 mg) were mixed with 8 μL of 4% aqueous solution of hydroxypropylcellulose (Aldrich, MW 100 000) and 2 μL of 10% aqueous solution of Triton-X100 (Fluka), after which 4 μL of H_2O was added. Platinum mesh (4 × 4 mm^2, Goodfellow) served as a conductive support and the TiO_2 film was deposited by dip-coating. The coated area was ca. 2 × 4 mm^2 with an edge serving as an electrical contact. The prepared electrodes were dried in air and finally calcined in air at 450 °C for 30 min. Control tests by Raman spectra confirmed that there was no significant contamination of $Ti^{18}O_2$ with ^{16}O coming from water and/or from the other auxiliary chemicals mentioned above.

Experimental Methods. The electrochemical and spectroelectrochemical studies were carried out in an airtight spectroelectrochemical cell under Ar[33,34] using a μAutolabIII (Eco Chemie) controlled by NOVA 1.5 software. The Pt wire was employed as a counter electrode and AgCl-coated Ag-wire as the pseudoreference electrode. The latter is a convenient reference electrode for in situ Raman spectroelectrochemistry due to its easier use. To calibrate the potential of our Ag/AgCl-pseudoreference electrode, the cyclic voltammograms of Li-insertion were reproduced with the usual Li-metal) reference electrode (in 1 M $LiClO_4$). Figure S1 (Supporting Information) compares both electrochemical scales, indicating that our Ag/AgCl pseudoreference is upshifted by 2.78 V against the Li^+/Li reference electrode. One molar $LiClO_4$ (alternatively $^6LiClO_4$) in ethylene carbonate/dimethyl carbonate (EC/DMC, 1/1 by volume) was used as the electrolyte solution. The in situ Raman spectra were measured in a quasi-equilibrium state, which was attained after 3 min of arresting the electrode potential at the selected value. The spectra were normalized by subtracting the signals from the electrolyte solution. The Raman spectra were measured on a MicroRaman system (LabRAM HR spectrometer, Horiba Jobin-Yvon) with an Olympus BX microscope. The spectra were excited by a He−Ne integrated laser (633 nm), a diffraction grating of 1800 grooves/mm was used providing a point-to-point spectral resolution of 0.32 cm^{-1}. The ex-situ spectra of powder samples were measured in a hermetically closed optical cell to avoid any contact with air. The measurements at low temperature used the THS600 (Linkam, UK) stage cooled by liquid nitrogen. The Raman spectrometer was calibrated before each set of

dx.doi.org/10.1021/cm402056j | Chem. Mater. 2013, 25, 3710−3717

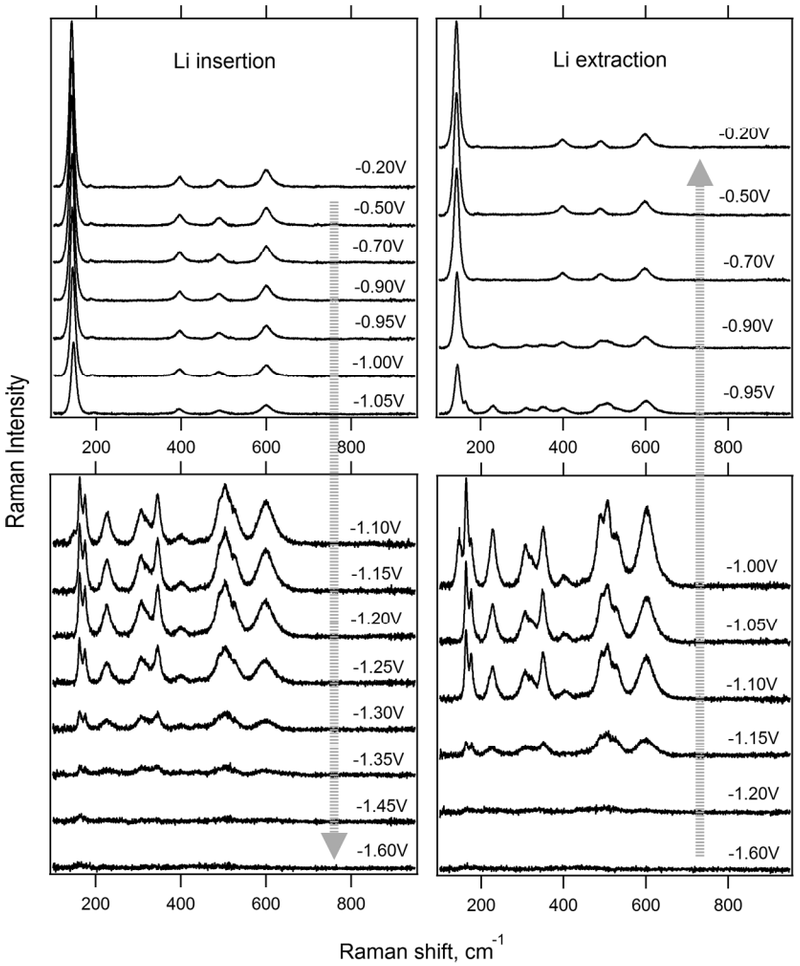

Figure 1. In situ Raman spectra of the $Ti^{18}O_2$ (anatase) electrode, which was treated in $^7LiClO_4$ + EC/DMC (1/1) at the potentials indicated. The left charts depict the spectra at gradually decreased potentials for the curves from top to bottom, that is, for Li-insertion. The right charts (bottom to top) show reverse process, that is, Li-extraction. The intensity scale is zoomed by a factor of 4 in the two bottom charts. The spectra are offset for clarity, but the intensity scale is identical in each chart.

measurements using the F_{1g} line of Si at 520.2 cm^{-1} as a reference. All spectra were deconvoluted using Lorentzian peak shapes. Scanning electron microscopy (SEM) images were acquired at Hitachi FE SEM S-4800 microscope. The BET surface areas of the prepared materials were determined from nitrogen adsorption isotherms at 77 K using the Micromeritics ASAP 2020 instrument. The X-ray diffraction was investigated on powder sample Bruker D8 Advance diffractometer using CuKα radiation.

Calculations. The atomic coordinates for $Li_{0.5}TiO_2$ were taken from Belak et al.[35] (28 atoms in the unit cell). The Raman frequencies were calculated by the CASTEP program,[36] which is a DFT-based code. The positions of all atoms were optimized by energy minimization prior to the spectral calculations, but the experimental lattice parameters were kept fixed. Electron-correlation effects were modeled using the generalized gradient approximation of Perdew, Burke and Ernzerhof.[37] For the atomic position optimization and Raman spectra calculation, we employed norm-conserving pseudopotentials, a plane wave cutoff energy of 900 eV with integrals taken over the Brillouin zone using a Monkhorst–Pack[38] grid of a minimum k-point sampling of 0.05 $Å^{-1}$ (12 k-points in total).

RESULTS AND DISCUSSION

The as-prepared $Ti^{16}O_2$ and $Ti^{18}O_2$ materials were characterized by the X-ray diffraction (XRD; Figure S2, Supporting Information) and the scanning electron microscopy (SEM, Figure S3, Supporting Information). The X-ray diffractograms confirm phase-pure anatase in both cases. The coherent domain size was determined from the XRD line width using the Scherrer formula, and compared to the particle size, which was estimated assuming the spherical anatase particle with the BET surface area of 31 m^2/g (see Experimental Section).[39,40] The calculated particle size was 50 nm, while the coherent domain sizes were 14 nm for $Ti^{16}O_2$ and 13 nm for $Ti^{18}O_2$. SEM images show sintered aggregates of about 30–60 nm in size for both samples.

The in situ Raman spectroelectrochemical data acquired on a $Ti^{18}O_2$ (anatase) electrode in $LiClO_4$ + EC/DMC electrolyte solution are shown in Figure 1. The electrolyte had a natural Li isotope composition (92.5% of ^7Li), which is approximated as $^7LiClO_4$. The spectra were acquired in a potentiostatic regime with the equilibration time of 3 min at each selected potential (see the Experimental Section). Under these conditions, the insertion coefficients at the given potential were similar to those found during a voltammetric sweep (Supporting Information, Figure S1 and Table S1). The sequence of measurement started from −0.2 V vs Ag/AgCl, which is near the open-circuit voltage (x = 0). Consequently, the initial spectrum is that of pristine $Ti^{18}O_2$ (anatase).[30,31] At a potential around −1 V ($x \approx 0.05$),

dx.doi.org/10.1021/cm402056j | Chem. Mater. 2013, 25, 3710–3717

the Raman features of orthorhombic Li_xTiO_2 start to grow, but the intensities attenuate again at potentials smaller than −1.15 V ($x \approx 0.2$), and become nonmeasurable around −1.6 V ($x \approx 0.4$).

The spectrum of TiO_2 (anatase) is completely transformed to that of orthorhombic Li-titanate at a lower level of lithiation than $Li_{0.5}TiO_2$, which is considered the nominal stoichiometry of this phase[17] (cf. Figure 1, Figure S1 and Table S1, Supporting Information). During the cathodic potential sweep, the strongest anatase mode, $E_g(1)$ suddenly disappears at the onset of insertion. This occurs between −1.05 V and −1.15 V, that is, between $x \approx 0.06$ and $x \approx 0.2$. A similar effect was observed also by others[15−17] and attributed to the surface-sensitivity of the Raman measurement on core−shell particles with a Li-rich phase at the surface.[15] No features assignable to tetragonal $LiTiO_2$ are perceptible, even at the most negative potentials, which essentially matches the conclusion of ref 17.

Nevertheless, even though the Raman spectrum was erased at −1.6 V, the reverse potential sequence (the right charts in Figure 1) caused an almost perfect restoration of all the features seen in the previous insertion potential sweep. More specifically, the spectrum of $Ti^{18}O_2$ (anatase) is fully recovered via the intermediate spectrum of orthorhombic Li_xTiO_2, but there is a small hysteresis in the insertion/extraction processes, cf. the spectra at −1.05 V (top left chart, Figure 1) and at −0.95 V (top right chart, Figure 1). Again, we observe an abrupt spectral transformation near −1 V, although the coexistence of both phases (TiO_2/Li_xTiO_2) is now detectable in a broader potential window during the extraction process. The good reversibility of our spectroelectrochemical data compares favorably to earlier works on the same subject.[15−18,25,26] They either did not report on the spectroelectrochemical reversibility,[16−18,25,26] or they found it irreversible.[15]

More specifically, Hardwick et al.[15] tested three different TiO_2 anatase materials in composite electrodes with carbon black and a fluoropolymer binder, but detected significant spectroelectrochemical irreversibility in all these three materials during the insertion/extraction potential sweep. The irreversibility was attributed to a poor electrical contact between some TiO_2 particles and the current collector in composite electrodes.[15] Similar composite electrodes were also used in the spectroelectrochemical studies reported by others.[16−18,26] Obviously, our binder-free and carbon-free electrodes (see the Experimental Section) no longer suffer from these problems, that is, the pure sintered titania nanoparticles supported by the Pt-mesh seem to be the ideal electrode for in situ Raman spectroelectrochemistry.

Figure 2 shows a detailed analysis of the spectra with a ^7Li-containing electrolyte for both oxygen isotopes acquired at −1.25 V, i.e. under conditions where pure orthorhombic Li-titanate is expected. The found Raman peaks are labeled p1 to p20. Certain peaks (p3, p6, p11, p18) are not distinguishable in Figure 2 or they overlap (p4 + p5 and p19 + p20), but these peaks can be deconvoluted in some other spectra, which will be shown in the text below. For the sake of coherent discussion, we shall keep the same peak coding in all our samples/spectra, *vide infra*. Supporting Information Table S2 summarizes the corresponding experimental Raman frequencies for all four samples representing the possible combinations of Li−O isotopologues in our system, that is, 6−16, 7−16, 6−18 and 7−18. Supporting Information Table S2 further compiles the corresponding isotope shifts, Δ_{1618} and Δ_{67} (cf. Equations 2a, 3a). The experimentally found Δ_{1618} shifts confirm that all

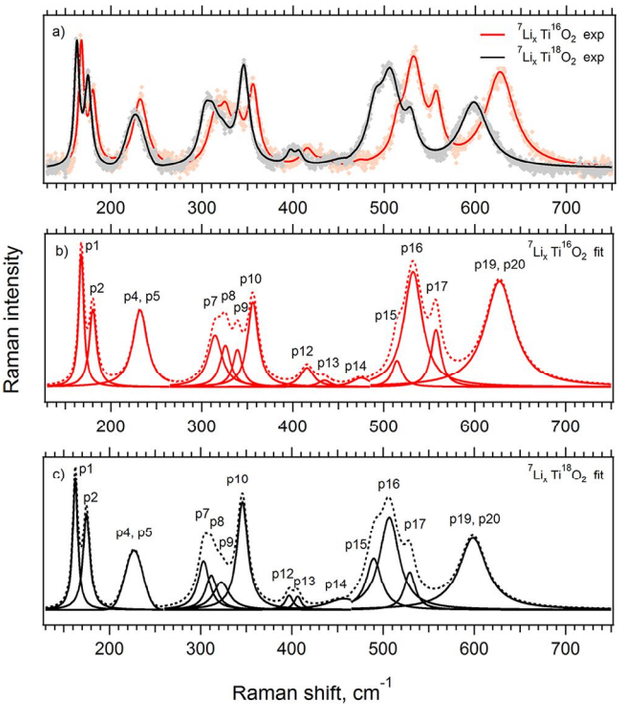

Figure 2. In situ Raman spectra of lithium titanates at −1.25 V vs Ag/AgCl electrode (corresponding to 1.53 V against the Li/Li$^+$ electrode) evolved by ^7Li insertion into $Ti^{16}O_2$ (red points) and $Ti^{18}O_2$ (gray points) using $LiClO_4$ in EC/DMC (1/1). The solid lines represent the convolution of individual Lorentzian components for $^7Li_xTi^{16}O_2$ (red) and $^7Li_xTi^{18}O_2$ (black). The individual Lorentzian components of $^7Li_xTi^{16}O_2$ and $^7Li_xTi^{18}O_2$ with their convolutions (dashed lines) are shown in charts (b) and (c), respectively.

peaks of orthorhombic Li-titanate contain some proportion of oxygen atom movement. The peaks p9, p12, p13, p15, p16, p17 are almost pure oxygen vibrations with isotope shifts close to the theoretical value of $^{max}\Delta_{1618}$ = 5.7%, see eq 2a,2b. This is reminiscent of the behavior of the A_{1g} mode in pristine TiO_2 anatase.[30,31] Solely in one case of a low-intensity shoulder peak (p13 in $^7Li_xTiO_2$), the measured shift slightly exceeds the theoretical maximum value, $^{max}\Delta_{1618}$ = 5.7%. We ascribe this to the larger error in the deconvolution of this particular peak. On the other hand, the fitting is quite accurate in most other cases.

The peaks p1, p2, p8−p10 and p17 do not shift upon Li-isotope exchange at all ($\Delta_{67} = 0$) and also the contribution of Li-movement to the vibration is quite small in the remaining measured peaks. The experimentally observed shifts are much smaller than the theoretical value for pure Li-vibration $^{max}\Delta_{67}$ = 7.4%, (see eq 3b) in all the modes measured, which is rationalized in terms of hindered Li^+−Li^+ interaction by Coulombic repulsion in the lattice. This is assumed to be responsible for the limitation in Li-uptake (up to $x \approx 0.7$) in anatase.[3] To better visualize the effect of Li-isotope exchange, the corresponding data are replotted in Figure 3 for both Li-isotopes inserted into $Ti^{18}O_2$. Other combinations of isotopologues studied under the same conditions, that is, electrochemical Li-insertion at −1.25 V, are shown in Figures S4, S5, Supporting Information.

Figure 4 shows the spectra of the powder samples of $^7Li_xTi^{16}O_2$ and $^7Li_xTi^{18}O_2$ made by chemical lithiation with n-butyllithium. This reactant has been reported to mimic electrochemical Li-insertion at potentials of ca. 1 V vs Li/Li$^+$

dx.doi.org/10.1021/cm402056j | *Chem. Mater.* 2013, 25, 3710−3717

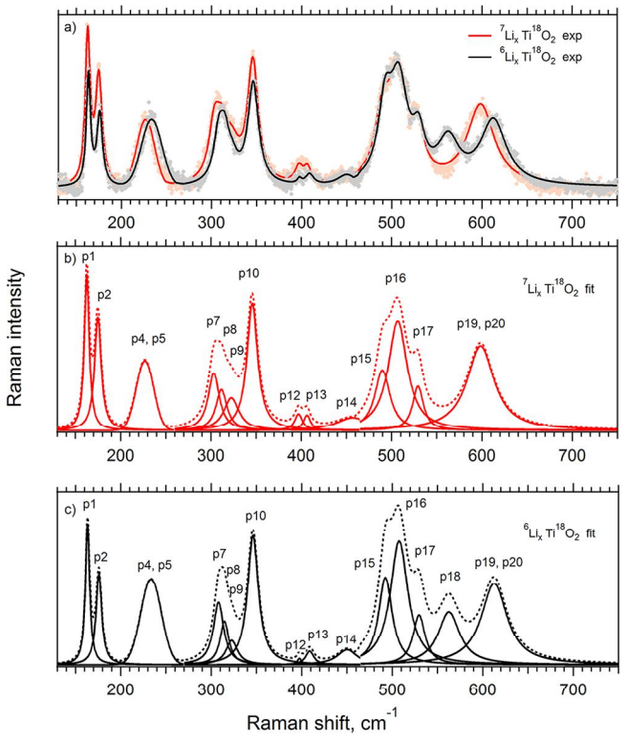

Figure 3. In situ Raman spectra of lithium titanates at −1.25 V vs Ag/AgCl electrode (corresponding to 1.53 V against the Li/Li$^+$ electrode) evolved by ^{7}Li insertion into $Ti^{18}O_2$ (red points) and ^{6}Li insertion into $Ti^{18}O_2$ (gray points) using $LiClO_4$ in EC/DMC (1/1). The solid lines represent the convolution of individual Lorentzian components for $^7Li_xTi^{18}O_2$ (red) and $^6Li_xTi^{18}O_2$ (black). The individual Lorentzian components of $^7Li_xTi^{18}O_2$ and $^6Li_xTi^{18}O_2$ with their convolutions (dashed lines) are shown in charts (b) and (c), respectively.

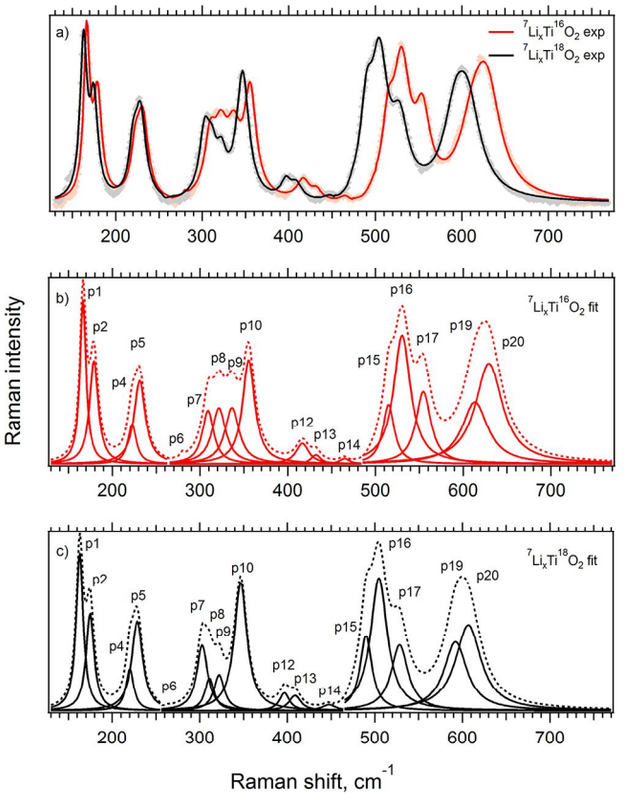

Figure 4. Ex-situ Raman spectra of lithium titanate prepared by chemical lithiation (with *n*-butyllithium, ^{7}Li) of $Ti^{16}O_2$ (red points) and $Ti^{18}O_2$ (gray points). The solid lines represent the convolution of individual Lorentzian components for $^7LiTi^{16}O_2$ (red) and $^7LiTi^{18}O_2$ (black). The individual Lorentzian components of $^7Li_xTi^{16}O_2$ and $^7Li_xTi^{18}O_2$ with their convolutions (dashed lines) are shown in charts (b) and (c), respectively.

(approx. −1.8 V vs Ag/AgCl) if *n*-butyllithium is used in large surplus.[3,6] The spectra of chemically lithiated titania can be compared to those of the corresponding products (with the same isotope mutations) obtained by electrochemical lithiation as shown in Figure 2. To our knowledge, the comparison of electrochemically and chemically lithiated anatase is presented here for the first time, although some earlier works[17] also prepared their samples by using both synthetic protocols. The main difference between electrochemically and chemically lithiated samples consists in a slightly better spectral resolution of the latter. Even though their deconvolution is still not precise, we distinguish the peaks p4/p5 and p19/p20 in the chemically made $^7Li_xTi^{16/18}O_2$ (Figure 4, Table S3, Supporting Information), but not in the corresponding spectra of electrochemically made samples (Figures 2 and 3). Otherwise, the spectra look expectedly similar, both in peak frequencies and their relative intensities. Minor variations in the intensities are attributable to slightly different linewidths, causing changes when the peaks overlap. Obviously, no other phases beyond orthorhombic Li_xTiO_2 are found upon reaction with *n*-butyllithium, which indirectly proves that the starting host was a well-defined anatase without TiO_2(B) and/or amorphous impurities (cf. ref 22).

To further improve spectral resolution, we repeated our measurements at low temperature in liquid nitrogen (77 K). The result is shown in Figure 5 for chemically prepared $^7Li_xTi^{16}O_2$ and $^7Li_xTi^{18}O_2$. This experimental sequence is completed by the low-temperature spectra of electrochemically prepared analogues, $^6Li_xTi^{16/18}O_2$ (Figures S6–S8, Supporting Information). In some cases, the spectra show contamination with TiO_2 (anatase) which is apparent in Figures 5c, S6b, S7c and S8b, Supporting Information. We ascribe this contamination to partial air-oxidation during sample transfer and/or handling. The Li-titanate is known to be air sensitive; therefore, the in situ electrochemical approach is preferable for room temperature measurements, because it provides cleaner experimental conditions and no oxidative contaminations (cf. Figures 1–3).

To summarize, 20 peaks are deconvoluted in all our Li_xTiO_2 isotopologues at 77 K. The observed frequencies and isotope shifts are listed in Tables 1 and S4, Supporting Information. It should be noted that in spite of a significant narrowing of the bands and thus a more precise fitting in most cases, the exact position of certain shoulder peaks (e.g., p19) is still debatable. The number of the measured bands is higher than in the previous works,[15,17,18,25,26] but it is still lower than the 42 Raman modes expected for the orthorhombic $Li_{0.5}TiO_2$ ($14A_g + 14B_{1g} + 7B_{2g} + 7B_{3g}$) from our DFT calculation. Obviously, low-intensity bands are unnoticed in the experimental spectra. The DFT calculation with a finite displacement algorithm does not make it possible to estimate band intensities due to the metallic character of the material.

dx.doi.org/10.1021/cm402056j | *Chem. Mater.* 2013, 25, 3710–3717

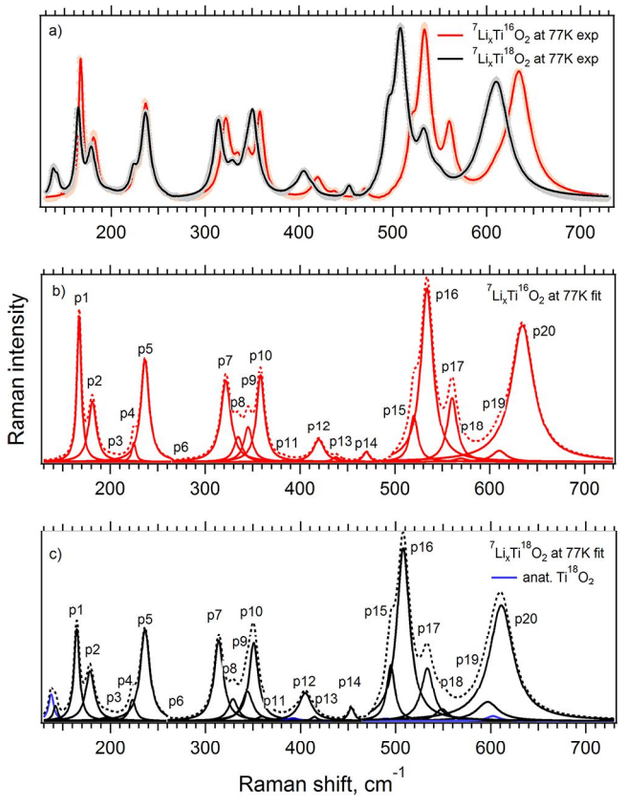

Figure 5. Ex-situ Raman spectra of lithium titanate prepared by chemical lithiation (with *n*-butyllithium, ^{7}Li) of $Ti^{16}O_2$ (red points) and $Ti^{18}O_2$ (gray points). The solid lines represent the convolution of individual Lorentzian components for $^{7}LiTi^{16}O_2$ (red) and $^{7}LiTi^{18}O_2$ (black). The individual Lorentzian components of $^{7}Li_xTi^{16}O_2$ and $^{7}Li_xTi^{18}O_2$ with their convolutions (dashed lines) are shown in charts (b) and (c), respectively. Anatase $Ti^{18}O_2$ impurity is also depicted in chart (c). The spectra were measured at 77 K.

The calculated positions of all the 42 Raman bands for the four isotopologues studied, including the symmetries of the respective vibrations and the corresponding atomic contributions for Li and O atoms are given in Table S5, Supporting Information. We should note that the number of our calculated vibrations (42) is considerably higher than the 9 modes ($3A_g$ + $3B_{2g}$ + $3B_{3g}$) predicted by Hardwick et al.[15] from their factor group analysis and the 15 modes measured experimentally by the same authors.[15] A possible explanation for the discrepancy in the theoretically simulated spectra is, that we used a refined structural model, in which the effect of Li consists not only in lowering the symmetry, but also in a larger primitive unit cell, in which the original *a*-axis of anatase is doubled along the b-direction[35] (see the Calculations section for details). All our 42 calculated bands fall in the range between 100 and 650 cm^{-1} in agreement with our experimental spectra. Given the high number of the calculated Raman bands and their unknown intensities, the assignment of the experimental peaks is based on the band positions and/or their corresponding isotope shifts.

Although the finite displacement calculation method is widely used, and can be very accurate, it has certain limitations too. Since the calculations use periodic boundary conditions, the repeating cell (the supercell) must be large enough for all the elements of the force constant matrix to be reduced to negligible values at the boundary of the supercell. This is readily achieved for some materials, particularly for metals. In ionic materials, however, convergence can be slow, because in the limit of zero wave-vector, the displacement of charges creates dipoles which interact with long-range forces, and therefore the force constant elements fall off with r^{-3} (r is interatomic distance).[41] Since force constants and dynamical matrices do not depend on nuclear mass, one set of computations is sufficient irrespective of isotopic substitution. Thus, the frequencies for different isotopic substitutions may be obtained without recomputing the dynamical matrices. This straightforward approach fails to take into account isotopic shifts in bond lengths and geometry and is therefore an approximate one.

There are several possible sources of errors in the Raman spectra calculations:[42] (i) errors related to the plane-wave pseudopotential DFT method caused by the treatment of exchange, correlation and the pseudopotential approximations, (ii) errors associated with evaluating forces using a finite basis set and a finite k-point set, (iii) errors in the finite convergence of the structural parameters—the geometry optimization is performed until the forces on the atoms reach a suitably small value, (iv) forces arising from anharmonicity, and (v) computational rounding errors and interpolation errors resulting from the discrete grid on which the wave function is represented. We performed the geometry optimization and the Raman spectra calculation for all isotope combinations available in our experiments. This allowed us to estimate the error associated with points (iii) and (v). For all vibrations, the calculated contributions of Li and O (differing to some extent for each isotopologue) were averaged and the corresponding shifts Δ_{67} and Δ_{1618} were calculated from eqs 3 and 2, respectively, giving also the standard deviations for the two traced isotope pairs in each vibration.

Table 1 (right part) shows these average Δ_{67} and Δ_{1618} shifts with the standard deviations for vibrations, which were selected as the most probable counterparts to the experimental ones, based on the combination of the proximity of the absolute frequency (up to ±40 cm^{-1}) and the closest possible Δ_{67} and Δ_{1618} shift when compared to the experimental values. As can be seen from Table 1, for the 15 peaks above 250 cm^{-1} a quite close match is found in most cases, i.e. the measured Δ_{67} and Δ_{1618} shifts fall within the standard deviation of the respective DFT calculated averaged shifts plus the possible error from the experimental spectral resolution. However, worse agreement is achieved for the lowest 5 peaks. It is especially apparent for the p5 peak, which exhibits an experimental Δ_{67} value of ca. half of the maximum shift expected for pure Li-vibration ($^{max}\Delta_{67}$ = 7.4%) and the Δ_{1618} shift close to zero, yet no such vibration was found in the calculation. We may only speculate about the reason for this discrepancy. Two partially overlapping bands in the position of p5 in the experimental spectra, which would "switch" intensities for the different isotopologues cannot be fully ruled out, a similar situation seems to occur around the p18 peak.

We now turn our attention to the issue of the two lithium atom positions in Li-titanate proposed by Wagemaker et al.[4,5] The two discrete sites for Li within an oxygen octahedron should be separated by ca. 0.3 Å. Hence, they cannot be occupied simultaneously and the Li atoms are supposed to hop between the two positions on a picosecond time scale.[5] On top of that, the occupancy of the two sites is equivalent at room temperature (RT), whereas one site becomes preferential at lower temperatures.[5] This finding, based so far on ^{7}Li NMR[4]

dx.doi.org/10.1021/cm402056j | *Chem. Mater.* 2013, 25, 3710−3717

Table 1. Comparison of the Measured (Electrochemically Prepared) and DFT Calculated Raman Frequencies of $^{6}Li_xTi^{16}O_2$, Measured Isotope Shifts for All Isotopologues (from Values in Supporting Information Table S4)[a]

	measured (77 K)					DFT calculated					
	$^{6}Li_xTi^{16}O_2$	^{16}O	^{18}O	^{6}Li	^{7}Li	$^{6}Li_{0.5}Ti^{16}O_2$	average			st.deviation	
peak	ν (cm^{-1})	Δ_{67} (%)	Δ_{67} (%)	Δ_{1618} (%)	Δ_{1618} (%)	ν (cm^{-1})	Δ_{67} (%)	Δ_{1618} (%)	sym.	Δ_{67} (%)	Δ_{1618} (%)
p1	169.7	1.4	0.8	2.2	1.6	165.7	0.1	0.8	B_{3g}	0.1	0.2
p2[b]	185.4	2.3	1.2	2.5	1.4	198.3	1.1	2.8	A_g	0.2	0.2
p3	203.4	1.3	0.7	2.4	1.8	236.1	0.9	2.7	B_{1g}	0.2	0.6
p4	227.6	1.2	0.3	1.5	0.7	244.1	0.1	3.2	A_g	0.0	0.4
p5[b]	245.9	3.8	2.8	1.1	0.1	247.8	0.3	3.1	B_{1g}	0.1	0.1
p6	282.1	0.6	0.4	4.2	4.0	286.7	0.9	4.6	B_{2g}	0.3	0.2
p7[b]	329.0	2.2	1.3	3.3	2.4	295.2	2.5	2.9	B_{1g}	0.3	0.1
p8	338.7	1.2	0.1	2.7	1.7	293.1	1.0	2.9	A_g	0.3	0.1
p9	349.6	1.2	−0.1	1.7	0.4	311.9	1.3	3.1	A_g	0.3	0.5
p10[b]	359.6	0.3	−0.2	2.7	2.1	354.9	0.3	3.9	B_{1g}	0.1	0.1
p11	385.3	0.8	1.7	5.1	5.9	387.2	1.3	4.6	B_{3g}	0.7	0.5
p12[b]	424.2	1.0	0.9	3.7	3.5	429.6	1.0	3.6	B_{1g}	0.2	0.2
p13	438.1	0.1	0.5	4.8	5.3	456.2	0.2	5.3	B_{1g}	0.1	0.1
p14[b]	475.5	1.2	1.0	3.7	3.5	467.7	0.7	4.2	A_g	0.3	0.4
p15	525.8	1.1	0.7	5.2	4.8	502.1	0.7	4.4	A_g	0.8	0.5
p16[b]	535.6	0.3	0.3	4.9	4.8	534.8	0.2	4.5	A_g	0.1	0.1
p17[b]	562.0	0.3	0.2	4.9	4.8	535.4	0.1	5.7	B_{2g}	0.0	0.0
p18	588.2	3.2	4.1	2.7	3.6	572.9	2.7	3.2	B_{1g}	0.9	0.8
p19	620.9	1.7	−0.8	4.6	2.2	583.1	1.6	3.2	A_g	1.0	0.8
p20[b]	643.8	1.5	2.2	2.9	3.6	610.2	0.8	2.7	B_{1g}	0.6	0.4

[a]The averaged DFT calculated shifts between Li (Δ_{67}) and O (Δ_{1618}) isotopes are listed with the corresponding standard deviations. All peaks are assigned to symmetries of the calculated vibrations. The measured Raman spectra were acquired at 77 K. The isotope shifts are given in % according to eq 2a and 3a. [b]Peaks with high measured intensity; their deconvolution is more precise.

and neutron diffraction studies,[5] should also be reflected in the Raman spectra; more specifically in the vibrations with a higher contribution of Li atoms. Indeed, changes in the position (upshift) and narrowing of the peaks with the lowered temperature of the Raman measurement correlate with the Li contribution of the vibrations. As an example, Supporting Information Figure S9 shows the Raman spectra of chemically lithiated $^{7}Li_xTi^{18}O_2$ at RT and 77 K. The differences in the peak positions (the values from Tables 1 and S4, Supporting Information) correlate with the measured Δ_{67} shifts with a Pearson coefficient of 0.58 with the 2-tail significance of 0.031 (see Supporting Information Figure S10). Note: A Pearson coefficient equal to 1 means a perfectly linear positive dependence and equal to 0 means no correlation, where the lower the significance the more important the statistical test is.

The changes of Raman linewidths between RT and 77 K (Table S6, Supporting Information) in $^{7}Li_xTi^{18}O_2$ are correlated with the Li contribution to the particular vibration mode with a Pearson coefficient of 0.42. For $^{7}LixTi^{16}O_2$, the Pearson correlation coefficients are 0.51 and 0.47 for the frequencies and widths, respectively, with a significance of ~0.05. Even though the correlations with the Li contribution are on the verge of a 5% significance in most cases, there is no correlation between the same peak parameters with the contribution of O (the Pearson coefficients <0.2, significance >0.4) or Ti. We may thus assume that the more prominent narrowing and shift of the "Li-rich" vibrations like p5 with temperature confirms the Li behavior proposed previously.[4,5] The existence of two Li positions may in turn be also one of the reasons for the observed difference between the measured and calculated peak frequencies (see above). However, when we started the geometry optimization from the structure with the occupied Li^{II} site (the notation of Wagemaker et al.[5]), it proceeded to the minimal geometry with the lithium atom in position I. This is in agreement with the previous observation based on neutron diffraction experiments, namely that the fraction of lithium atoms in site II decreases with decreasing temperature,[5] that is, the position I represents the enthalpy minimum. Therefore, we were not able to calculate the vibrational spectrum for the structure with Li^{II}. Note that geometry optimization is a prerequisite for the calculation of the Raman frequencies.

CONCLUSION

Electrochemical Li-insertion into TiO_2 (anatase) was investigated with the aid of isotope labeling on four isotopologue combinations in the system, namely $^{6/7}Li_xTi^{16/18}O_2$ (with x being the insertion coefficient). Chemical Li-insertion using *n*-butyllithium provided analogous samples, $^{7}Li_xTi^{16/18}O_2$.

Raman spectra were measured both in situ during electrochemical Li-insertion and ex-situ on isolated end-products, the latter also at a temperature of 77 K. The formation of orthorhombic Li_xTiO_2 manifested itself by a sudden change of the spectra when the insertion reaction was triggered. The process was fully reversible, albeit with small hysteresis in the spectra measured during the insertion/extraction potential sweeps, and with a slightly broader extraction-potentials window, in which the spectra of TiO_2/Li_xTiO_2 coexisted. The spectrum of the pure orthorhombic phase Li_xTiO_2 was detected already at $x \ll 0.5$, due to the core−shell morphology of the intermediate product of insertion. No other phases (tetragonal, cubic or hexagonal phases of $LiTiO_2$) were found even at the deepest level of lithiation.

Our DFT calculations predicted theoretically 42 Raman active vibrations ($14A_g + 14B_{1g} + 7B_{2g} + 7B_{3g}$) for the

dx.doi.org/10.1021/cm402056j | Chem. Mater. 2013, 25, 3710−3717

orthorhombic $Li_{0.5}TiO_2$. Experimental spectra allowed identification of 20 modes. The number of both theoretically predicted and experimentally measured Raman modes is considerably larger, if we compare our results with the theoretical/experimental data found in earlier literature. On the basis of Raman frequencies and the Li/O isotope shifts, all the observed 20 modes were assigned.

The DFT calculation was unable, for principal reasons, to distinguish between the two sites Li^I and Li^{II} in the orthorhombic Li_xTiO_2, which were assumed on the basis of previous NMR and neutron diffraction studies. On the other hand, there was a significant correlation between the difference of Raman frequency measured at room temperature and at 77 K and a Li-contribution to the particular mode. The same correlation was found also for the Raman linewidths, but there was no correlation between the same Raman parameters and the O- or Ti-contributions to the vibration. This brings additional arguments in favor of the existence of Li^I/Li^{II} sites in the structure.

■ ASSOCIATED CONTENT

Ⓢ Supporting Information

Cyclic voltammogram of Li-insertion into $Ti^{18}O_2$, X-ray diffraction patterns and SEM images of $Ti^{16}O_2$ and $Ti^{18}O_2$ samples and additional Raman spectra. This material is available free of charge via the Internet at http://pubs.acs.org.

■ AUTHOR INFORMATION

Corresponding Author

*E-mail: kavan@jh-inst.cas.cz.

Notes

The authors declare no competing financial interest.

■ ACKNOWLEDGMENTS

This work was supported by the Czech Science Foundation (contract No. 13-07724S). We are grateful to Jenő Kürti and János Koltai (Loránd Eötvös University Budapest) for stimulating discussions.

■ REFERENCES

(1) Kavan, L.; Grätzel, M.; Gilbert, S. E.; Klemenz, C.; Scheel, H. J. *J. Am. Chem. Soc.* **1996**, *118*, 6716.
(2) Hengerer, R.; Kavan, L.; Krtil, P.; Grätzel, M. *J. Electrochem. Soc.* **2000**, *147*, 1467.
(3) Wagemaker, M.; Van de Krol, R.; Kentgens, A. P. M.; Van Well, A. A.; Mulder, F. M. *J. Am. Chem. Soc.* **2001**, *123*, 11454.
(4) Wagemaker, M.; Kentgens, A. P. M.; Mulder, F. M. *Nature* **2002**, *418*, 397.
(5) Wagemaker, M.; Kearley, G. J.; Van Well, A. A.; Mutka, H.; Mulder, F. M. *J. Am. Chem. Soc.* **2003**, *125*, 840.
(6) Wagemaker, M.; Borghols, W. J. H.; Mulder, F. M. *J. Am. Chem. Soc.* **2007**, *129*, 4323.
(7) Berger, T.; Monllor-Setoca, D.; Jankulovska, M.; Lana-Villarreal, T.; Gomez, R. *ChemPhysChem* **2012**, *13*, 2824.
(8) Kavan, L. *Chem. Rec.* **2012**, *12*, 131.
(9) Myung, S.T.; Takahashi, N.; Komaba, S.; Yoon, C.S.; Sun, Y.K.; Amine, K.; Yashiro, H. *Adv. Funct. Mater.* **2011**, *21*, 3231.
(10) Yang, Z.; Choi, D.; Kerisit, S.; Rosso, K. M.; Wang, D.; Zhang, J.; Graff, G.; Liu, J. *J. Power Sources* **2009**, *192*, 588.
(11) Huang, S. Y.; Kavan, L.; Grätzel, M.; Exnar, I. *J. Electrochem. Soc.* **1995**, *142*, L142–L144.
(12) Jiang, C.; Zhang, J. *J. Mater. Sci. Technol.* **2013**, *29*, 97.
(13) Ohzuku, T.; Takehara, Z.; Yoshizawa, S. *Electrochim. Acta* **1979**, *24*, 219.
(14) Cava, R. J.; Murphy, D. W.; Zahurak, S. M.; Santoro, A.; Roth, R. S. *J. Solid State Chem.* **1984**, *53*, 64.
(15) Hardwick, L. J.; Holzapfel, M.; Novák, P.; Dupont, L.; Baudrin, E. *Electrochim. Acta* **2007**, *52*, 5357.
(16) Ren, Y.; Hardwick, L. J.; Bruce, P. G. *Angew. Chem., Int. Ed.* **2010**, *49*, 2570.
(17) Gentili, V.; Brutti, S.; Hardwick, L. J.; Armstrong, A. R.; Panero, S.; Bruce, P. G. *Chem. Mater.* **2012**, *24*, 4468.
(18) Smirnov, M.; Baddour-Hadjean, R. *J. Chem. Phys.* **2004**, *121*, 2348.
(19) Wagemaker, M.; Lutzenkirchen-Hecht, D.; Van Well, A. A.; Frahm, R. *J. Phys. Chem. B* **2004**, *108*, 12456.
(20) Lafont, U.; Carta, D.; Mountjoy, G.; Chadwick, A. V.; Kelder, E. M. *J. Phys. Chem. C* **2010**, *114*, 1372.
(21) Macklin, W. J.; Neat, R. J. *Solid State Ionics* **1992**, *53–56*, 694.
(22) Kavan, L.; Kalbac, M.; Zukalova, M.; Exnar, I.; Lorenzen, V.; Nesper, R.; Grätzel, M. *Chem. Mater.* **2004**, *16*, 477.
(23) Van de Krol, R.; Goossens, A.; Meulenkamp, E. A. *J. Electrochem. Soc.* **1999**, *146*, 3150.
(24) Wagemaker, M.; Borghols, W. J. H.; van Eck, E. R. H.; Kentgens, A. P. M.; Kearley, G. J.; Mulder, F. M. *Chem.—Eur. J.* **2007**, *13*, 2023.
(25) Dinh, N. N.; Oanh, N. T. T.; Long, P. D.; Bernard, M. C.; Hugot-Le Goff, A. *Thin Solid Films* **2003**, *423*, 70.
(26) Baddour-Hadjean, R.; Bach, S.; Smirnov, M.; Pereira-Ramos, J. P. *J. Raman Spectrosc.* **2004**, *35*, 577.
(27) Giarola, M.; Samson, A.; Monti, F.; Mariotto, G. *Phys. Rev. B* **2010**, *81*, 174305.
(28) Mazza, T.; Milani, P. *Appl. Phys. Lett.* **2007**, *91*, 046103.
(29) Rosella, F.; Galinetto, P.; Mozzati, M. C.; Malavasi, L.; Diaz Fernandez, Y.; Drera, G.; Sangaletti, L. *J. Raman Spectrosc.* **2010**, *41*, 558.
(30) Kavan, L.; Zukalova, M.; Ferus, M.; Kürti, J.; Koltai, J.; Civis, S. *Phys. Chem. Chem. Phys.* **2011**, *13*, 11583.
(31) Frank, O.; Zukalova, M.; Laskova, B.; Kürti, J.; Koltai, J.; Kavan, L. *Phys. Chem. Chem. Phys.* **2012**, *14*, 14567.
(32) Pelouchova, H.; Janda, P.; Weber, J.; Kavan, L. *J. Electroanal. Chem.* **2004**, *566*, 73.
(33) Kavan, L.; Dunsch, L. *ChemPhysChem* **2007**, *8*, 974.
(34) Kavan, L.; Dunsch, L. *ChemPhysChem* **2011**, *12*, 47.
(35) Belak, A. A.; Wang, Y.; Van der Ven, A. *Chem. Mater.* **2012**, *24*, 2894.
(36) Clark, S. J.; Segall, M. D.; Pickard, C. J.; Hasnip, P. J.; Probert, M. J.; Payne, M. C. *Z. Kristallogr.* **2005**, *220*, 567.
(37) Perdew, J. P.; Burke, K.; Ernzerhof, K. *Phys. Rev. Lett.* **1996**, *77*, 3865.
(38) Monhkorst, H. J.; Pack, J. D. *Phys. Rev. B* **1976**, *13*, 5188.
(39) Kavan, L.; Murakami, T. N.; Comte, P.; Grätzel, M. *Electrochem. Solid State Lett.* **2007**, *10*, A85–A87.
(40) Kavan, L.; Grätzel, M.; Rathousky, J.; Zukal, A. *J. Electrochem. Soc.* **1996**, *143*, 394.
(41) Alfe, D. *Comput. Phys. Commun.* **2009**, *180*, 2622.
(42) Ackland, G. J.; Warren, M. C.; Clark, S. J. *J. Phys.: Condens. Matter* **1997**, *9*, 7861.

Supporting Information

Lithium Insertion into Titanium Dioxide (Anatase): A Raman Study with $^{18/16}$O and $^{6/7}$Li Isotope Labeling

Barbora Laskova[a,b],Otakar Frank[a], Marketa Zukalova[a], Milan Bousa[a,b], Martin Dracinsky[c], and Ladislav Kavan[a, b]

[a] *J. Heyrovský Institute of Physical Chemistry, v.v.i. Academy of Sciences of the Czech Republic, Dolejskova 3, 18223 Prague 8, Czech Republic*
[b] *Department of Inorganic Chemistry, Faculty of Science, Charles University, Hlavova 2030/8, CZ-128 43 Prague 2, Czech Republic*
[c] *Institute of Organic Chemistry and Biochemistry, v.v.i. Academy of Sciences of the Czech Republic, Flemingovo nam. 2, 16610 Prague 6, Czech Republic*

Table S1 The Li-insertion coefficient, x determined from cyclic voltammogram (scan rate 0.2 mV/s) at the given potential. (The potentials are referred to the Ag/AgCl electrode, which is upshifted by 2.78 V against the Li/Li^+ electrode)

Insertion		Extraction	
Potential [V vs. Ag/AgCl]	x	Potential [V vs. Ag/AgCl]	x
-0.2	0	-1.6	0.406
-0.5	0	-1.2	0.279
-0.7	0.011	-1.15	0.279
-0.9	0.029	-1.1	0.278
-0.95	0.036	-1.05	0.277
-1	0.045	-1	0.275
-1.05	0.06	-0.95	0.273
-1.1	0.131	-0.9	0.268
-1.15	0.208	-0.7	0.0246
-1.2	0.249	-0.5	0
-1.25	0.276	-0.2	0
-1.3	0.298		
-1.35	0.322		
-1.45	0.369		
-1.6	0.406		

Table S2. The Raman frequencies of various isotopologues of Li_xTiO_2 generated electrochemically at -1.25 V vs. Ag/AgCl pseudoreference electrode (corresponding to 1.53 V against the Li/Li^+ electrode) ($x \approx 0.3$). Also shown are the istope shifts (in percent, calculated from Eqs. (2a) and (3b) for the actual experimental frequencies for all four possible combinations of isotopologues.

peak	$^6Li_xTi^{16}O_2$	$^7Li_x\,Ti^{16}O_2$	$^6Li_xTi^{18}O_2$	$^7Li_xTi^{18}O_2$	(^{16}O)	(^{18}O)	(^7Li)	(^6Li)
	ν (cm^{-1})	ν (cm^{-1})	ν (cm^{-1})	ν (cm^{-1})	Δ_{67} (%)	Δ_{67} (%)	Δ_{1618} (%)	Δ_{1618} (%)
p1	167.2	167.4	163.4	162.9	0	0	2.7	2.3
p2	179.9	180.1	175.9	175.3	0	0	2.7	2.2
p3	-	-	-	-	-	-	-	-
p4+p5[a]	237.0	232.2	233.6	227.7	2.0	2.5	1.9	1.4
p6	-	-	-	-	-	-	-	-
p7	317.7	314.2	308.1	304.3	1.1	1.2	3.2	3
p8	325.9	325.7	314.7	313.6	0	0	3.7	3.4
p9	338.5	339.9	322.7	323.8	0	0	4.7	4.7
p10	356.3	356.4	346.2	345.9	0	0	2.9	2.8
p11	-	-	-	-	-	-	-	-
p12	419.3	416.3	397.6	397.2	0.7	0	4.6	5.2
p13	433.5	436.7	408.8	408.1	0	0	6.6	5.7
p14	474.0	470.4	450.3	459.4	0.8	-2.0	2.3	5.0
p15	516.5	516.6	492.5	489.9	0	0.5	5.2	4.6
p16	531.9	532.5	507.7	506.1	0	0.3	5.0	4.5
p17	556.8	557.5	529.7	528.2	0	0	5.3	4.9
p18	578.1	-	562.7		-		-	2.7
p19+p20[a]	632.8	626.9	612.7	598.4	0.9	2.3	4.5	3.2

[a] overlapping bands fitted by one Lorentzian peak

Table S3. The Raman frequencies of $^{7}Li_xTiO_2$ generated by chemical reduction with n-butyllithium. Also shown are the istope shifts (calculated from Eq. 2b) for the actual experimental frequencies.

peak	$^{7}Li_xTi^{16}O_2$	$^{7}Li_xTi^{18}O_2$	(^{7}Li)
	ν (cm^{-1})	ν (cm^{-1})	Δ_{1618} (%)
p1	166.5	162.9	2.2
p2	179	174.8	2.3
p3	-	-	-
p4	222.5	220.1	1.1
p5	231.1	228.6	1.1
p6	279.9	264.4	5.5
p7	309.1	302.8	2
p8	321.5	311.2	3.2
p9	336.5	322.1	4.3
p10	355.4	346.7	2.4
p11	-	-	-
p12	416.6	396.7	4.8
p13	432.2	408.8	5.4
p14	464.9	447.5	3.7
p15	514.9	489.9	4.9
p16	530.4	504.7	4.8
p17	554.6	528.3	4.7
p18	-	-	-
p19	613.4	592.1	3.5
p20	629.4	606.8	3.6

Table S4. The Raman frequencies of various isotopologues of Li_xTiO_2 generated electrochemically at -1.25 V vs. Ag/AgCl pseudoreference electrode (corresponding to 1.53 V against the Li/Li^+ electrode); x≈0.3 ($^6Li_xTi^{16}O_2$, $^6Li_xTi^{18}O_2$) and chemically (^7Li_x $Ti^{16}O_2$, $^7Li_xTi^{18}O_2$). The Raman spectra were acquired at 77 K.

peak	$^6Li_xTi^{16}O_2$	^6Li_x $Ti^{18}O_2$	$^7Li_xTi^{16}O_2$	$^7Li_xTi^{18}O_2$
	ν (cm^{-1})			
p1	169.7	165.9	167.3	164.6
p2	185.4	180.9	181.2	178.6
p3	203.4	198.6	200.7	197.2
p4	227.6	224.1	224.8	223.3
p5	245.9	243.2	236.6	236.4
p6	282.1	270.2	280.4	269.2
p7	329.0	318.1	321.8	314.0
p8	338.7	329.4	334.8	329.0
p9	349.6	343.7	345.3	344.1
p10	359.6	350.0	358.4	350.8
p11	385.3	365.8	382.0	359.7
p12	424.2	408.6	419.7	405.0
p13	438.1	416.8	437.8	414.7
p14	475.5	458.0	469.9	453.4
p15	525.8	498.6	519.9	494.9
p16	535.6	509.6	533.8	508.1
p17	562.0	534.7	560.4	533.4
p18	588.2	572.5	569.4	548.8
p19	620.9	592.2	610.0	596.8
p20	643.8	624.9	634.4	611.2

Table S5. The calculated Raman frequencies of $Li_{0.5}TiO_2$ isotopologues. The involvement of different atoms in each normal vibration mode was characterized by the sum of the square roots of all components corresponding to the given atom. The atomic contributions for Li and O were averaged from calculations for each isotopologue, and are quoted as Avg(Li) and Avg(O), respectively. (The atomic contribution of Ti is 100-Avg(O)-Avg(Li)). The standard deviations (σ) of averaging are also listed in the last two columns.

symmetry	$^{6}Li_{0.5}Ti^{16}O_2$	$^{7}Li_{0.5}Ti^{16}O_2$	$^{6}Li_{0.5}Ti^{18}O_2$	$^{7}Li_{0.5}Ti^{18}O_2$	Atomic contributions			
	ν				Avg(Li)	Avg(O)	σ(Li)	σ(O)
	cm^{-1}				%			
A_g	107.5	122.3	111.9	123.2	16.1	20.5	1.2	2.3
B_{1g}	161.3	161.0	158.8	160.2	1.0	29.9	0.1	2.4
B_{2g}	165.1	163.6	163.9	164.9	0.0	3.7	0.0	0.4
B_{3g}	165.7	164.2	163.5	163.7	1.7	14.5	0.6	3.5
B_{3g}	171.9	171.8	173.1	172.3	1.7	11.3	0.2	2.4
B_{2g}	182.0	182.1	183.7	182.2	3.0	7.3	0.5	1.6
A_g	198.3	194.9	191.9	188.4	14.8	48.3	2.4	3.5
B_{1g}	236.1	233.7	229.6	227.5	12.4	47.6	2.7	10.0
A_g	244.1	244.2	232.6	234.8	0.9	56.3	0.4	7.2
B_{1g}	247.8	246.4	239.8	239.0	4.3	53.9	1.5	1.4
B_{3g}	254.1	252.5	245.3	242.5	10.3	63.4	2.5	2.9
B_{1g}	260.0	259.4	248.7	248.5	2.0	73.2	1.1	1.9
A_g	275.1	274.2	268.0	266.8	1.1	54.9	0.8	2.2
B_{1g}	277.6	274.5	272.4	270.2	11.8	30.8	8.0	5.3
B_{2g}	286.7	285.6	272.8	269.3	12.1	81.2	4.2	4.3
A_g	293.1	288.8	284.7	280.7	13.1	50.5	4.2	2.1
B_{1g}	295.2	288.1	287.1	279.4	33.3	50.6	3.9	2.3
B_{2g}	307.6	304.3	292.9	289.0	12.5	82.8	2.2	1.7
A_g	311.9	305.9	301.5	296.6	17.6	55.3	3.7	8.6
A_g	323.9	322.9	310.0	308.0	5.2	76.3	3.7	7.8
B_{3g}	331.1	329.1	313.5	310.5	8.5	90.0	2.6	2.4
B_{1g}	354.9	353.5	340.9	339.4	3.3	69.0	1.0	2.2
B_{2g}	365.5	363.5	347.0	345.0	7.1	91.0	2.3	2.3
B_{3g}	387.2	382.0	368.5	364.2	17.7	81.3	9.1	9.0
B_{1g}	397.7	388.6	389.0	380.7	28.0	36.3	2.4	2.4
A_g	410.2	402.8	400.6	393.9	27.0	39.8	1.8	1.4
B_{1g}	429.6	425.4	414.3	409.4	14.3	63.0	2.5	3.7
B_{3g}	440.6	419.7	434.0	411.4	60.1	39.8	14.0	14.0
B_{2g}	442.0	418.8	435.6	412.5	64.7	34.7	8.2	8.3
B_{1g}	456.2	455.8	432.0	431.3	3.2	93.7	1.5	1.4
A_g	462.6	461.3	442.1	441.3	5.0	74.6	3.0	11.4
A_g	467.7	463.2	447.4	444.3	10.1	73.7	4.4	7.3
B_{1g}	469.8	468.9	446.0	444.8	3.1	88.4	1.6	3.2
A_g	502.1	499.5	478.2	476.9	10.0	77.1	11.3	8.0
B_{1g}	527.5	509.7	505.3	495.4	35.3	60.3	16.5	17.1
A_g	528.8	503.9	510.2	493.5	54.1	37.9	12.3	11.2
B_{3g}	529.7	530.0	500.2	499.8	0.1	99.8	0.0	0.1
A_g	534.8	533.1	518.4	509.3	3.4	78.4	1.7	1.8
B_{2g}	535.4	535.7	505.5	504.9	0.6	99.2	0.2	0.2
B_{1g}	572.9	559.0	557.6	537.7	37.0	55.7	12.1	13.7
A_g	583.1	575.5	566.2	554.0	21.6	56.5	13.0	13.7
B_{1g}	610.2	607.0	594.4	588.5	10.9	47.6	8.4	7.7

Table S6. The full-widths-at-half-maxima (FWHM) of Raman peaks of $^{7}Li_xTiO_2$ generated by chemical reduction with with n-butyllithium at room temperature (RT) and 77 K. Values are in cm^{-1}. The entry Δ_{FWHM} is a difference between FWHM measured at room temperature and at 77 K.

peak	$^{7}Li_xTi^{16}O_2$ RT	$^{7}Li_xTi^{18}O_2$ RT	$^{7}Li_xTi^{16}O_2$ 77 K	$^{7}Li_xTi^{18}O_2$ 77 K	$^{7}Li_xTi^{16}O_2$	$^{7}Li_xTi^{18}O_2$
	FWHM	FWHM	FWHM	FWHM	Δ_{FWHM}	Δ_{FWHM}
p1	8.4	9.7	5.5	6.8	2.9	2.9
p2	11.9	11.1	10.0	11.1	1.9	0.1
p3	-	-	15.4	17.5	-	-
p4	11.5	10.9	5.3	8.0	6.2	2.8
p5	15.5	15.2	10.3	11.7	5.2	3.5
p6	4.2	12.0	5.4	5.4	-1.2	6.6
p7	15.6	15.0	12.5	11.8	3.2	3.2
p8	18.9	12.6	10.8	12.2	8.1	0.4
p9	19.5	14.3	10.6	13.8	8.9	0.4
p10	16.9	17.5	10.0	11.6	6.8	5.9
p11	-	-	5.4	12.4	-	-
p12	17.7	13.8	13.6	16.0	4.1	-2.2
p13	13.0	16.3	8.6	7.4	4.4	8.9
p14	13.6	19.2	7.7	7.4	5.9	11.8
p15	15.8	16.6	9.9	10.1	5.9	6.5
p16	23.4	23.0	15.4	16.2	8.0	6.8
p17	20.5	23.5	12.4	15.4	8.2	8.1
p18	-	-	15.7	16.6	-	-
p19	35.8	32.0	18.3	26.9	17.4	5.1
p20	37.4	35.5	28.3	30.0	9.0	5.5

Figure S1. The cyclic voltammogram of $Ti^{18}O_2$ (anatase) in 1 M $LiClO_4$ + EC/DMC (1/1), scan rate 0.2 mV/s. Current is normalized to the mass of the active electrode material. The potentials measured against the Ag/AgCl pseudoreference electrode are presented along with the corresponding potentials referenced to the Li^+/Li (1 M $LiClO_4$) reference electrode.

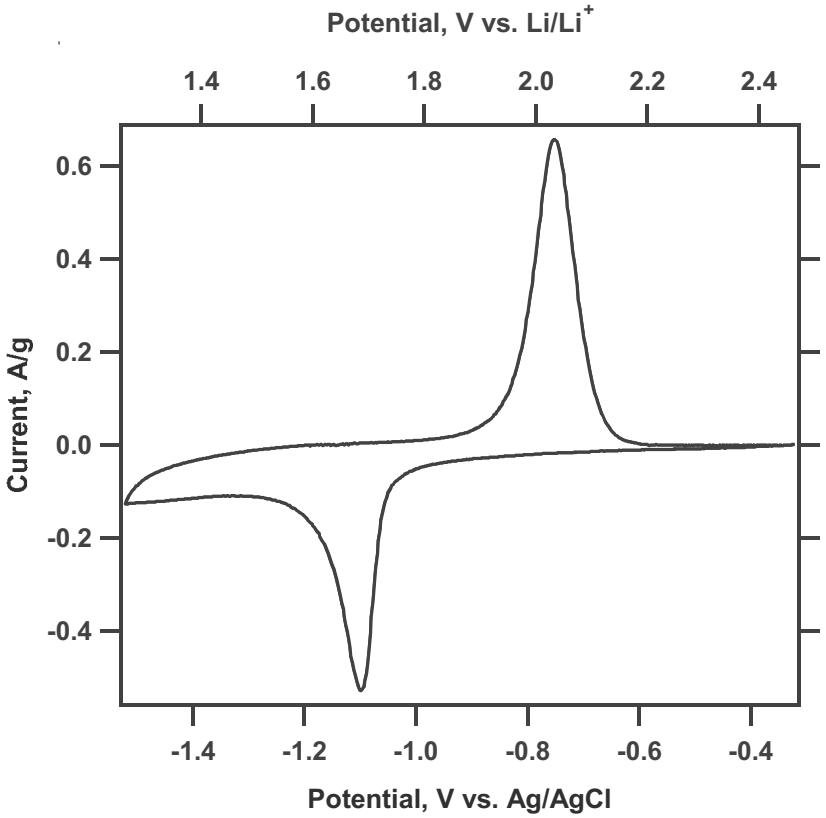

Figure S2. The X-ray diffraction patterns of anatase $Ti^{18}O_2$ and $Ti^{16}O_2$.

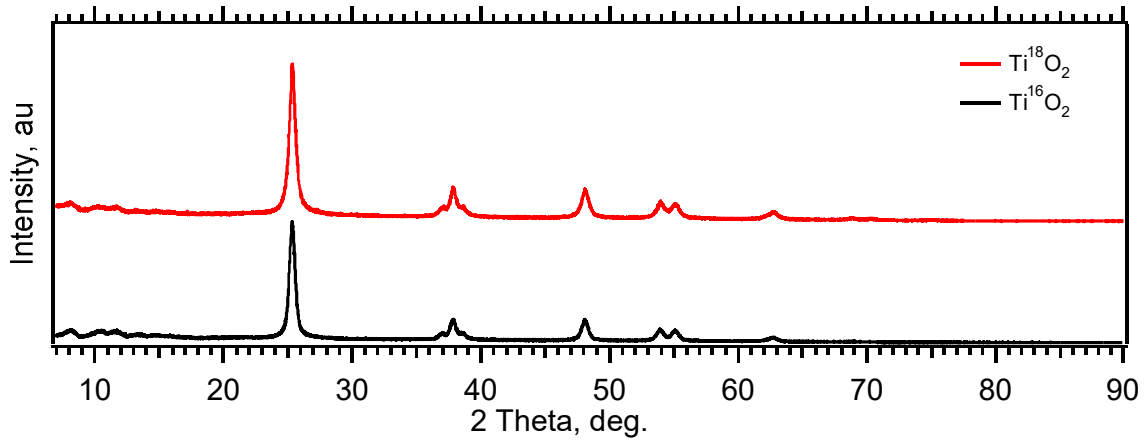

Figure S3. The scanning electron microscopy images of anatase $Ti^{16}O_2$ and $Ti^{18}O_2$.

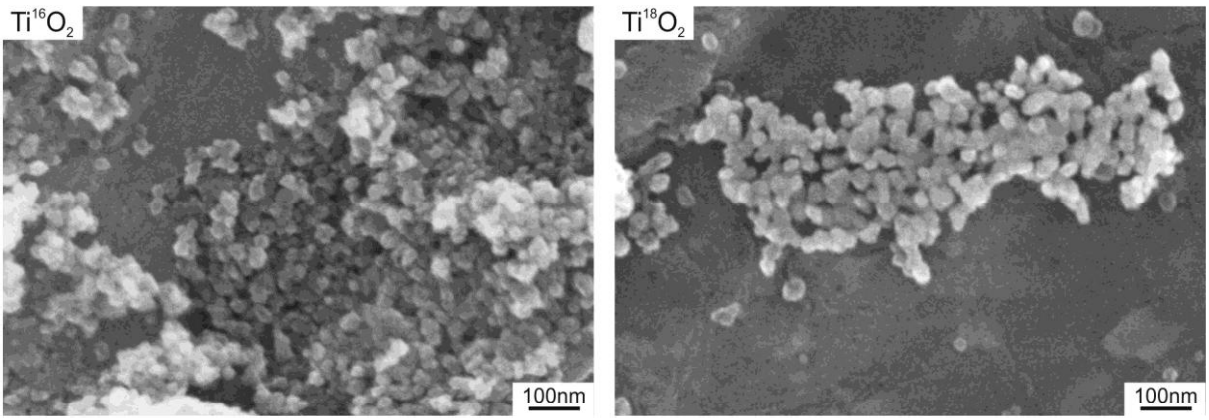

Figure S4. The in-situ Raman spectra of lithium titanates at -1.25 V vs. Ag/AgCl pseudoreference electrode (corresponding to 1.53 V against the Li/Li^+ electrode) made by ^6Li insertion into $Ti^{16}O_2$ (red points) and $Ti^{18}O_2$ (grey points). Electrolyte solution 1M $LiClO_4$ in EC/DMC (1/1). The solid lines represent convolution of individual Lorentzian components for $^6Li_xTi^{16}O_2$ (red) and $^6Li_xTi^{18}O_2$ (black). The individual Lorentzian components of $^6Li_xTi^{16}O_2$ and $^6LiTi^{18}O_2$ with their convolutions (dashed lines) are shown in charts (b) and (c), respectively.

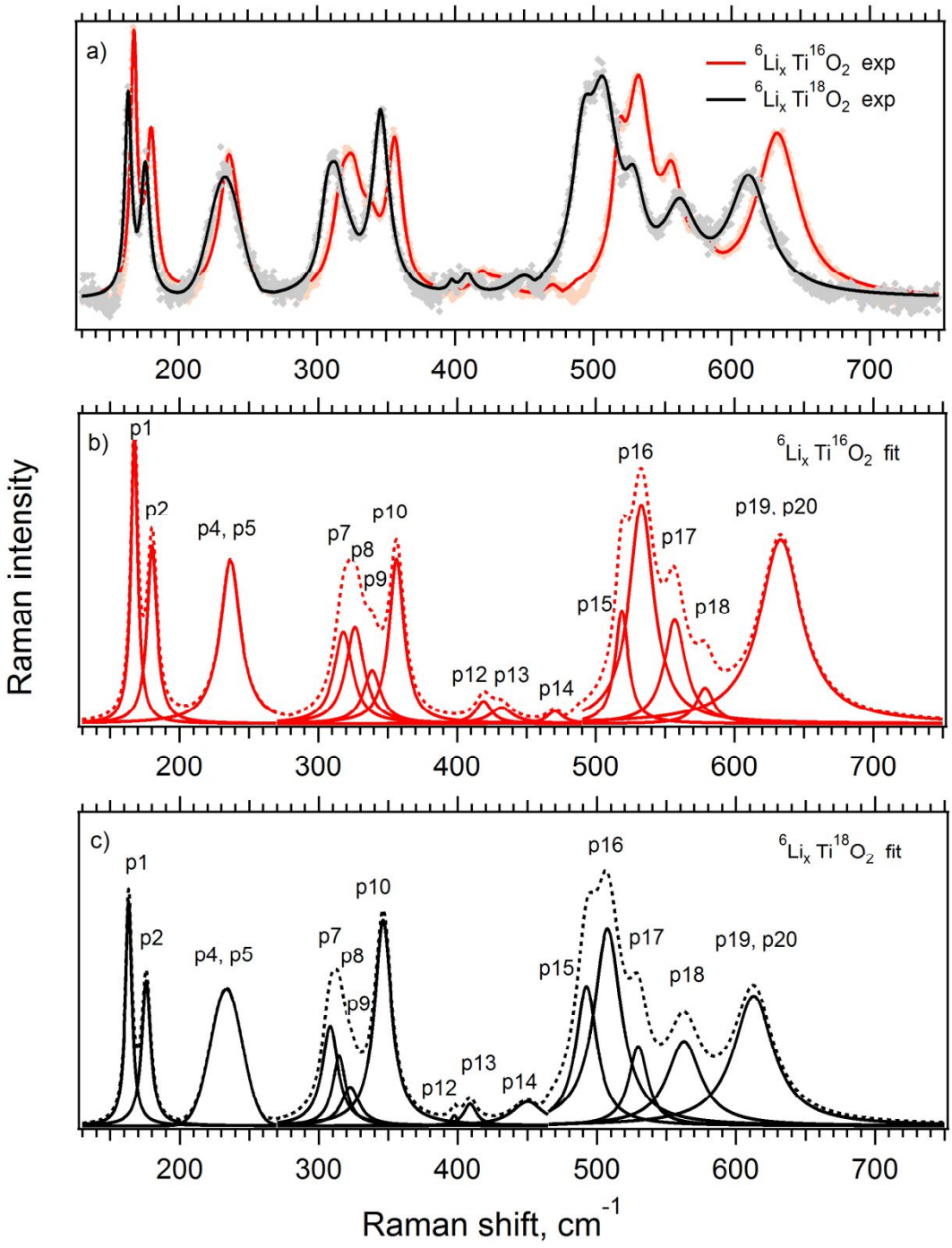

Figure S5. The in-situ Raman spectra of lithium titanates at -1.25 V vs. Ag/AgCl (corresponding to 1.53 V against the Li/Li^+ electrode) made by ^7Li insertion into $Ti^{16}O_2$ (red points) and ^6Li insertion into $Ti^{16}O_2$ (grey points). Electrolyte solution 1M $LiClO_4$ in EC/DMC (1/1). The solid lines represent convolution of individual Lorentzian components for $^7Li_xTi^{16}O_2$ (red) and $^6Li_xTi^{16}O_2$ (black). The individual Lorentzian components of $^7LiTi^{16}O_2$ and $^6LiTi^{16}O_2$ with their convolutions (dashed lines) are shown in charts (b) and (c), respectively.

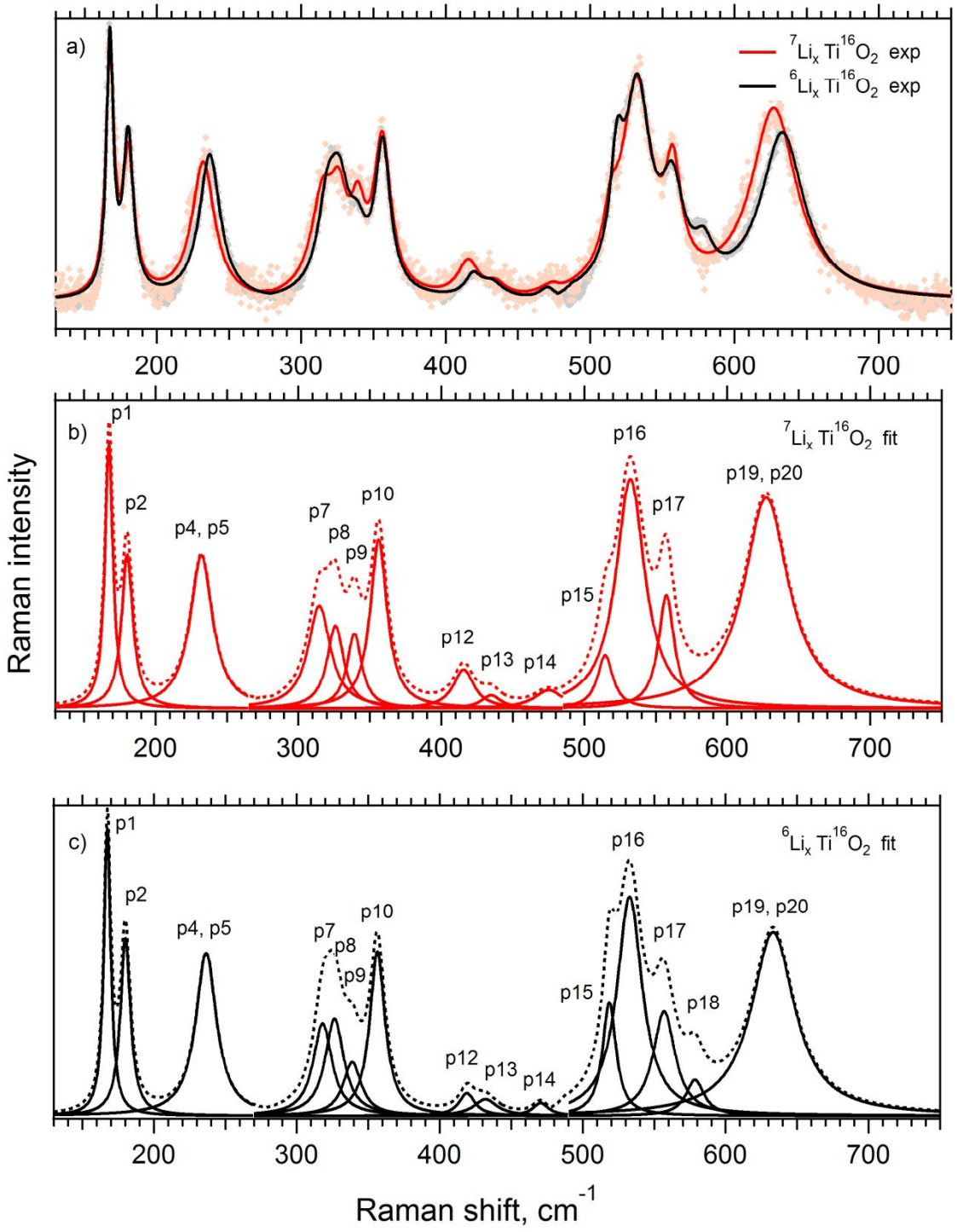

Figure S6. The ex-situ Raman spectra of lithium titanate prepared by electrochemical lithiation of $Ti^{16}O_2$ (red points) and $Ti^{18}O_2$ (grey points) in $^6LiClO_4$ electrolyte solution. The solid lines represent convolution of individual Lorentzian components for $^6Li_xTi^{16}O_2$ (red) and $^6Li_xTi^{18}O_2$ (black). The individual Lorentzian components of $^6Li_xTi^{16}O_2$ and $^6Li_xTi^{18}O_2$ with their convolutions (dashed lines) are shown in charts (b) and (c), respectively. Anatase $Ti^{16}O_2$ impurity is also seen in chart b. The spectra were measured at 77 K. The peak at ca. 125 cm^{-1} is unassigned. Since it does not appear in the same spectra at room teperature (Figs. 3,4) we ascribe it to an unknown impurity in these particular samples, $^6Li_xTi^{16/18}O_2$.

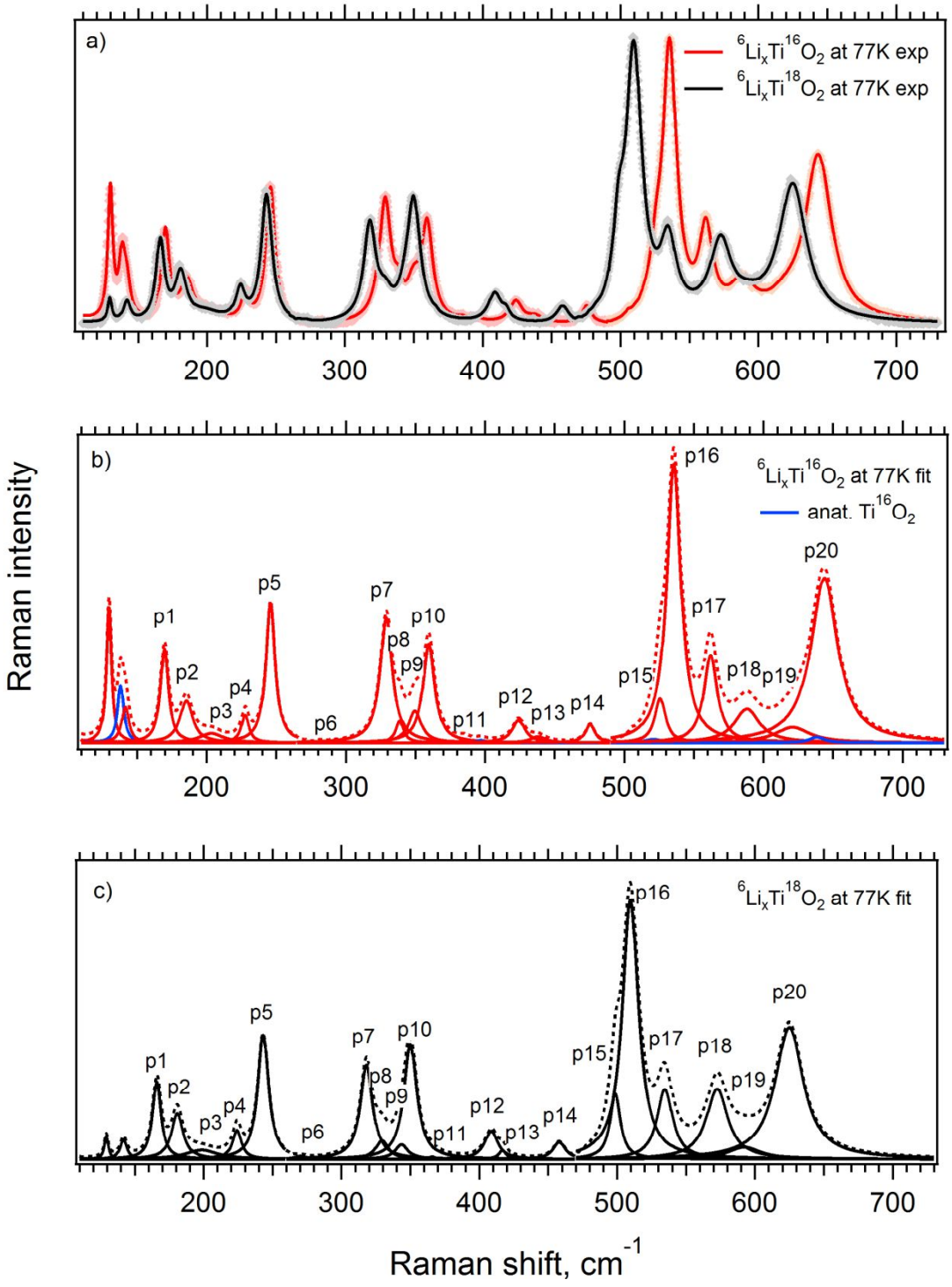

Figure S7. The ex-situ Raman spectra of lithium titanate prepared from $Ti^{16}O_2$ by electrochemical lithiation (^{6}Li, red points) or chemical lithiation (with n-butyllithium, ^{7}Li, grey points). The solid lines represent convolution of individual Lorentzian components for $^7Li_xTi^{16}O_2$ (red) and $^6Li_xTi^{16}O_2$ (black). The individual Lorentzian components of $^7Li_xTi^{16}O_2$ and $^6Li_xTi^{16}O_2$ with their convolutions (dashed lines) are shown in charts (b) and (c), respectively. Anatase $Ti^{16}O_2$ impurity is also seen in chart c. The spectra were measured at 77 K. The peak at ca. 125 cm^{-1} (charts a, c) is unassigned. Since it does not appear in the same spectra at room teperature (Figs. 3,4) we ascribe it to unknown impurity in this particular sample, $^6Li_xTi^{16}O_2$.

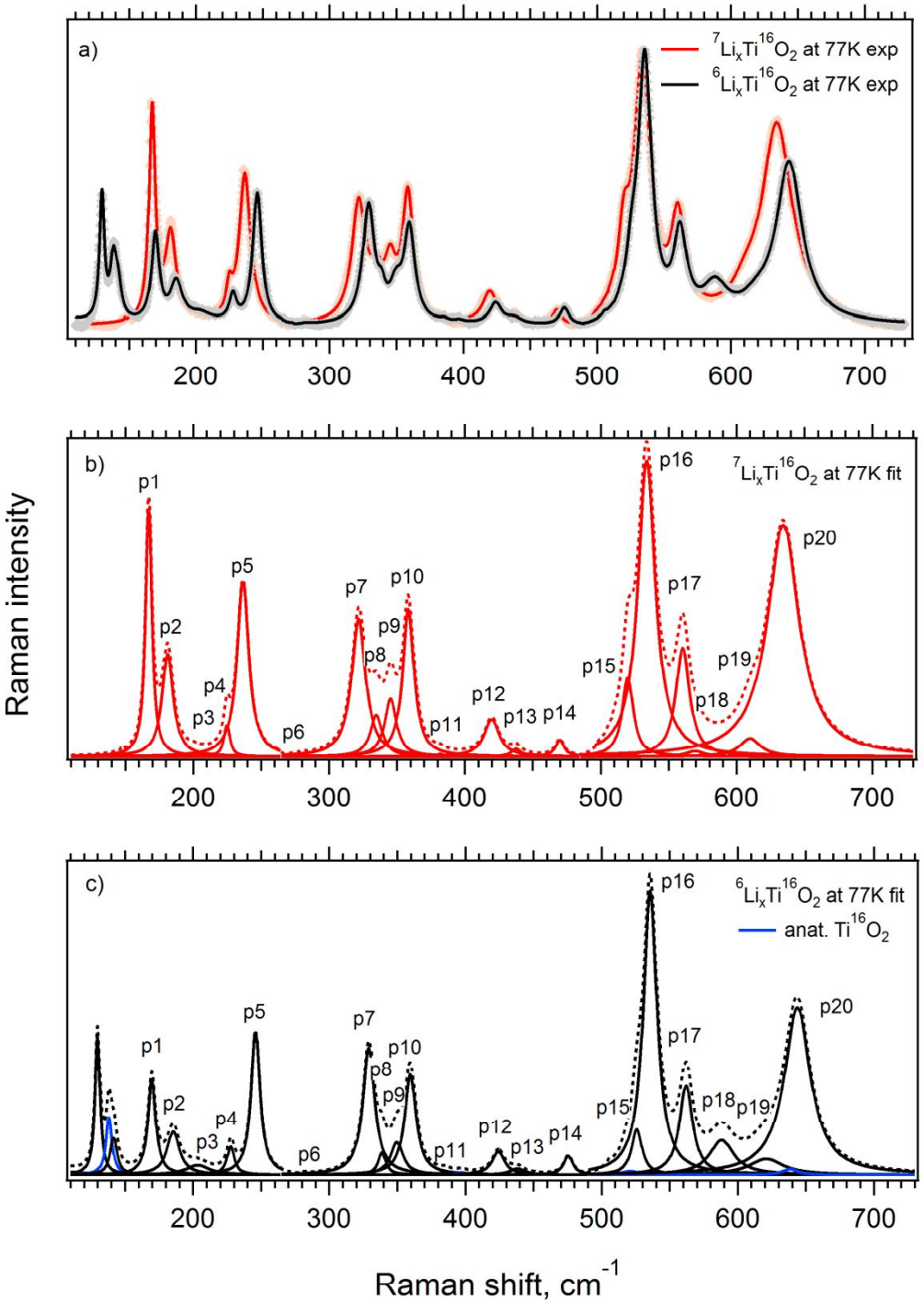

Figure S8. The ex-situ Raman spectra of lithium titanate prepared from $Ti^{18}O_2$ by electrochemical lithiation (^{6}Li, red points) or chemical lithiation (with n-butyllithium, ^{7}Li, grey points). The solid lines represent the convolution of individual Lorentzian components for $^7Li_xTi^{18}O_2$ (red) and $^6Li_xTi^{18}O_2$ (black). The individual Lorentzian components of $^7Li_xTi^{18}O_2$ and $^6Li_xTi^{18}O_2$ with their convolutions (dashed lines) are shown in charts (b) and (c), respectively. Anatase $Ti^{18}O_2$ impurity is also seen in chart b. The spectra were measured at 77 K. The peak at ca. 125 cm^{-1} (charts a, c) is unassigned. Since it does not appear in the same spectra at room teperature (Figs. 3,4) we ascribe it to unknown impurity in this particular sample, $^6Li_xTi^{18}O_2$.

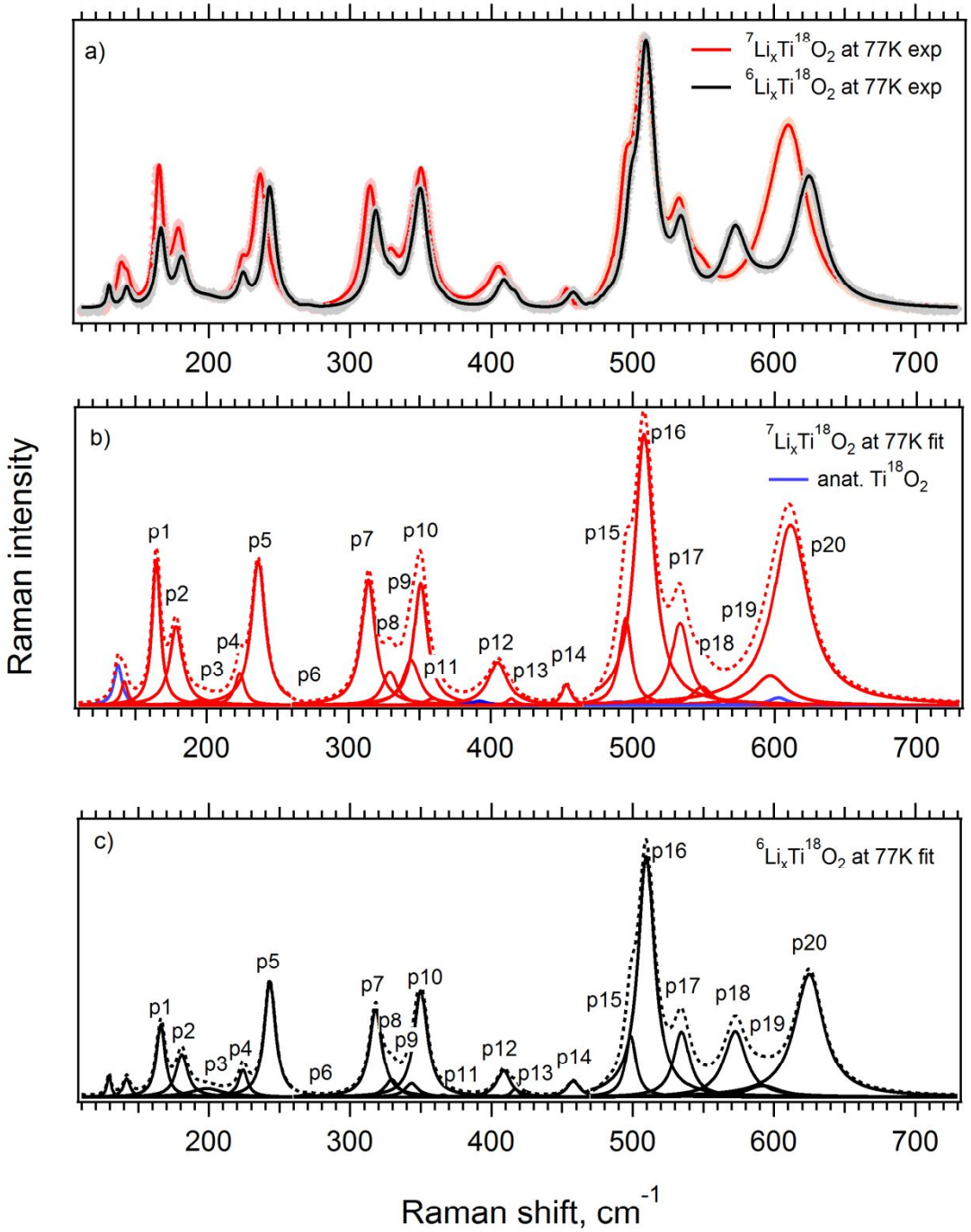

Figure S9. The ex-situ Raman spectra of lithium titanate prepared from $Ti^{18}O_2$ by chemical lithiation (with n-butyllithium, ^7Li) at room temperature (red) and 77 K (black). The spectrum of anatase impurity is also shown.

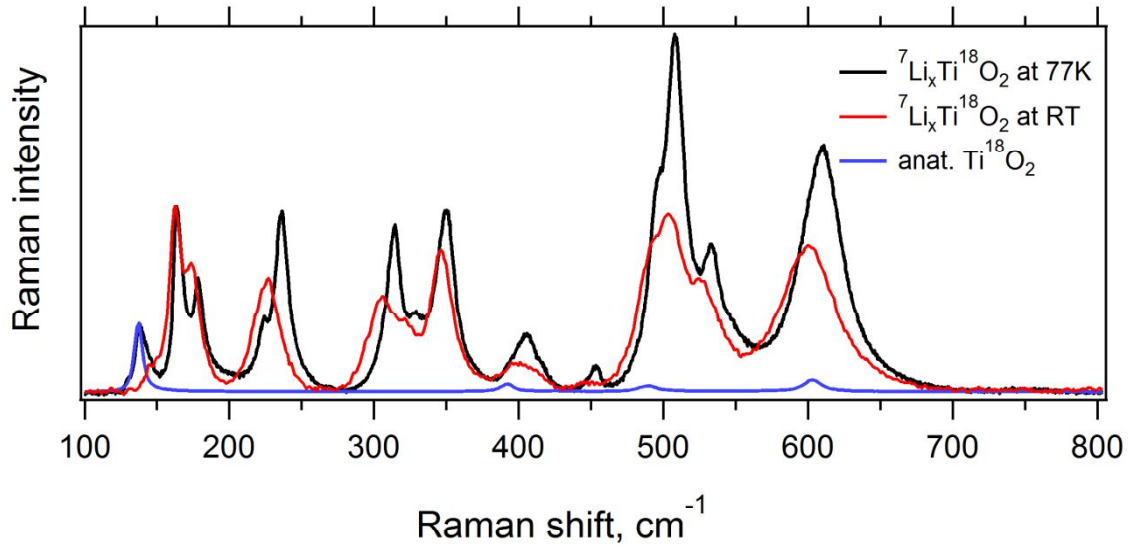

Figure S10. The scatter plot including the correlation ellipse for the relation between frequencies of peaks in chemically lithiated $^7Li_xTi^{18}O_2$ at 77 K and RT against the contribution of Li atoms to the respective vibrations as derived for the same material at 77 K from Δ_{67} using Eq. 3a.

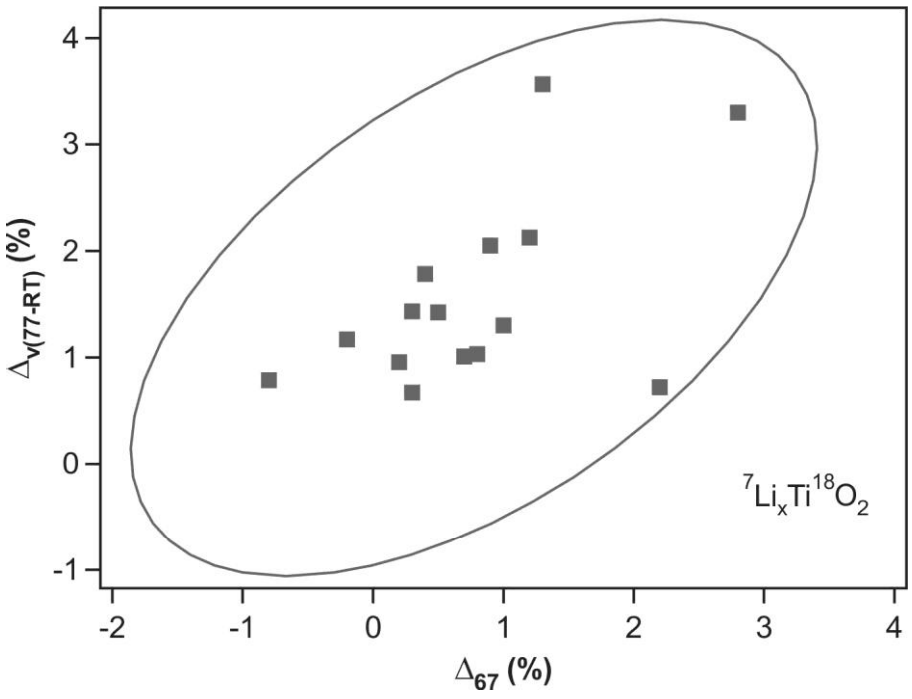

Appendix 4

Barbora Pitna Laskova, Ladislav Kavan, Marketa Zukalova, Karel Mocek and Otakar Frank. "In situ Raman spectroelectrochemistry as a useful tool for detection of TiO_2 (anatase) impurities in TiO_2 (B) and TiO_2 (rutile)." *Monatsh Chem*, 2016, **147**, 951-959.

Monatsh Chem (2016) 147:951–959
DOI 10.1007/s00706-016-1678-x

ORIGINAL PAPER

In situ Raman spectroelectrochemistry as a useful tool for detection of TiO_2(anatase) impurities in TiO_2(B) and TiO_2(rutile)

Barbora Pitna Laskova[1,2] · Ladislav Kavan[1,2] · Marketa Zukalova[1] · Karel Mocek[1] · Otakar Frank[1]

Received: 6 November 2015 / Accepted: 21 January 2016 / Published online: 9 March 2016

Abstract The TiO_2(B) and TiO_2(rutile) polymorphs are often contaminated by anatase phase residues from synthesis. The detection of anatase in TiO_2 material can be difficult in case of small anatase impurities. In situ Raman spectroelectrochemistry is presented here as the most reliable method for unequivocal determination of anatase phase in TiO_2 powder. Anatase detection is based on an occurrence of Raman vibrational bands of orthorhombic lithium titanate, a product of Li insertion in anatase, in Raman spectra of TiO_2(B) and TiO_2(rutile) materials during electrochemical Li^+ insertion/extraction.

Graphical abstract

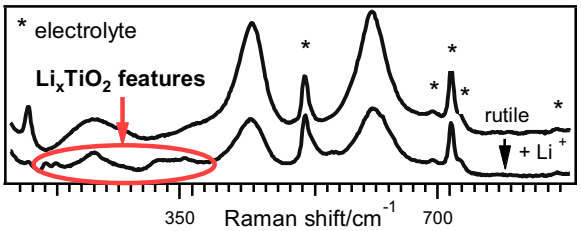

Keywords Raman spectroscopy · Electrochemistry · Nanochemistry · Phase transition

✉ Barbora Pitna Laskova
barbora.laskova@jh-inst.cas.cz

[1] Department of Electrochemical Materials, J. Heyrovsky Institute of Physical Chemistry of the AS CR, v.v.i., Dolejskova 3, 182 23 Prague 8, Czech Republic

[2] Department of Inorganic Chemistry, Faculty of Science, Charles University, Hlavova 2030/8, 128 43 Prague 2, Czech Republic

Introduction

Titanium dioxide (TiO_2) is a chemically stable non-toxic semiconductor material which is widely used mostly as white pigment in paints or in cosmetic industry. After the Fujishima and Honda's [1] discovery of water splitting on TiO_2 surface, TiO_2 became an attractive photocatalytic material. The development of nanomaterials opened new possibilities for TiO_2 application. Today, titanium dioxide is an important material for Li-ion batteries [2–5], photovoltaics [6, 7], catalysis and photocatalysis [4, 8, 9]. TiO_2 occurs in several natural and synthetic polymorphs, from which tetragonal modifications anatase and rutile are the most frequently used in applications due to their availability and stability [2, 3, 8–18]. In addition, metastable monoclinic TiO_2(B) has currently attracted attention of many research teams due to its open channel structure responsible for faster alkali metal insertion and higher Li-insertion coefficient predetermining this polymorph for charge storage applications [19–27]. An application potential of anatase nanoparticles, rutile nanocrystals and TiO_2(B) fibers motivated numerous studies addressing phase purity, phase transformation, particle size, nanocrystals shape, and electronic properties of these polymorphs [28–45].

The phase purity represents fundamental issue for correct interpretation of physicochemical, particularly electronic, properties of nanocrystalline TiO_2 polymorphs. Although the rutile phase is thermodynamically more stable for macroscopic crystals than the anatase one, anatase is considered to be a more stable form for nanocrystals below 20 nm in size. Hence, anatase impurities and post-synthetic residues in nanocrystaline rutile material are not rare [43, 46]. Analogously monoclinic TiO_2(B) can be easily contaminated with anatase during synthesis because

of metastability of the former [26]. X-ray diffraction (XRD) and Raman spectroscopy represent common methods for determination of phase composition of TiO_2 materials. However, XRD detectability of anatase impurities in low concentration is limited for small anatase nanocrystals and/or thin layers [21, 47]. In addition, an overlap of XRD diffraction peak of anatase [42] and TiO_2(B) [24] at 25° (2θ) further complicates applicability of this technique for detection of small amount of anatase phase in TiO_2(B). Raman spectra of rutile and TiO_2(B) are not unequivocal with regard to detection of minor anatase impurities as well. The first-order Raman scattering of rutile TiO_2 corresponds to four Raman-active vibrations: $A_{1g} + B_{1g} + B_{2g} + E_g$ [48]. Anatase TiO_2 has six Raman-active vibrations: $A_{1g} + 2B_{1g} + 3E_g$ and the TiO_2(B) has 18 Raman-active vibration modes: $12A_g + 6B_g$ [24, 48]. Unfortunately, the most intensive vibrational band E_g(1) of anatase is overlapped with the Raman mode B_{1g} of rutile and A_g(2) of TiO_2(B) at the corresponding wavenumber of 144 cm^{-1} [24, 48]. The overlap of vibrational bands of rutile and anatase can cause discrepancies in studies by Raman spectroscopy [48, 49]. Limited detectability of anatase phase in TiO_2(B) by means of XRD and Raman spectroscopy thus leads to questionable phase purity of TiO_2(B) in some studies [50, 51].

Here, we introduce in situ Raman spectroelectrochemistry of Li insertion as an extremely sensitive method for detection of very small impurities of anatase phase in TiO_2(B) and rutile. To the best of our knowledge, only papers reporting on in situ Raman spectroelectrochemistry of phase-pure anatase [30, 52–55] have been published until now. In situ Raman spectroelectrochemistry of TiO_2(B), rutile and their mixture with anatase phase is presented here for the first time.

Results and discussion

The powder X-ray diffraction patterns of both studied TiO_2(B) materials (TBa, TBb) and anatase C240 are presented in Fig. 1. The diffractograms prove the presence of monoclinic TiO_2(B) phase (space group *C*2/*m*, JCPD No. 35-0088) both in TBa and TBb [24, 56, 57]. However, the diffraction peak at 25° (2θ) is broadened for the TBb sample, which can be indirect proof of anatase impurities in the sample.

The Raman spectra of TBa and TBb powders were measured as a following step in characterization of phase structure of samples. Raman spectra of both materials showing features of TiO_2(B) are presented in Fig. 2 [21, 24, 56–58]. The TBa and TBb spectra differ mainly in the relative intensity of the vibrational band A_g(2) at 144 cm^{-1}. An additional low-intensity peak at 513 cm^{-1}

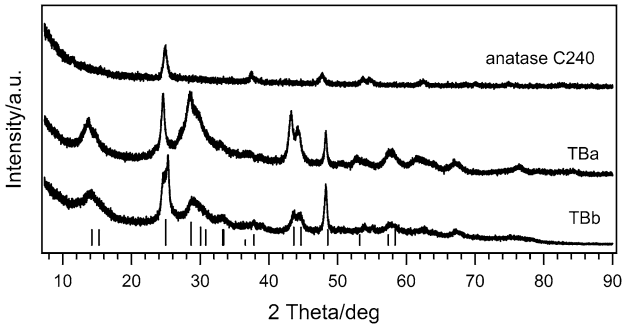

Fig. 1 X-ray diffractograms of samples. *Top to bottom* anatase C240, TBa, and TBb. The *vertical lines* correspond to the diffraction pattern of TiO_2(B) JCPD No. 35-0088

in the TBb spectrum compared to TBa is visible too. TiO_2(B) Raman mode A_g(2) overlaps the most intensive vibrational band E_g(1) of standard nanocrystalline anatase, which represents frequent contamination of TiO_2(B) phase. For that reason an increased intensity of the Raman mode at 144 cm^{-1} and a presence of the peak at 513 cm^{-1} were used as indication of anatase impurities in TiO_2(B) sample by Zukalova et al. [21]. However, in recent studies discrepancies persist and these features are more often assigned to TiO_2(B) structure [36, 57, 58]. Hence, another reliable method for detection of small anatase impurities in TiO_2(B) is still needed.

The changes in Raman spectra of TBa and TBb were investigated during Li insertion into these materials by in situ Raman spectroelectrochemistry. Recently, this technique has been applied to phase-pure anatase, where phase transition of tetragonal anatase to orthorhombic lithium titanate was observed and the spectrum of Li_xTiO_2 ($x \approx 0.2$–0.5) was characterized in detail [30, 52–55]. Cyclic voltammetry (CV) of Li insertion in TBa and TBb was measured at scan rate of 0.2 mV/s. The voltammograms are shown in Fig. 3a, b and correspond to a standard TiO_2(B) electrochemical response [21, 24]. Obviously, neither cathodic nor anodic peak of Li^+ insertion into anatase is observed during CV [3, 53]. There is only slight broadening of the TBb insertion peak at higher potentials, which could be caused by anatase, but the corresponding anatase extraction peak is not detected.

Subsequently, the Raman spectra of the samples were measured continuously during cyclic voltammetry at scan rate of 0.2 mV/s (for details see "Experimental" section). In situ Raman spectroelectrochemical data acquired on a TBa electrode in $LiClO_4$ + EC/DMC electrolyte solution are shown in Fig. 4. The sequence of measurement started near open-circuit voltage at 2.5 V versus Li/Li^+. The initial spectrum is that of pristine TiO_2(B) in electrolyte. Characteristic peaks of TiO_2(B) spectrum decrease gradually during the Li insertion (the left charts in Fig. 4). This observation can be explained by two simultaneous

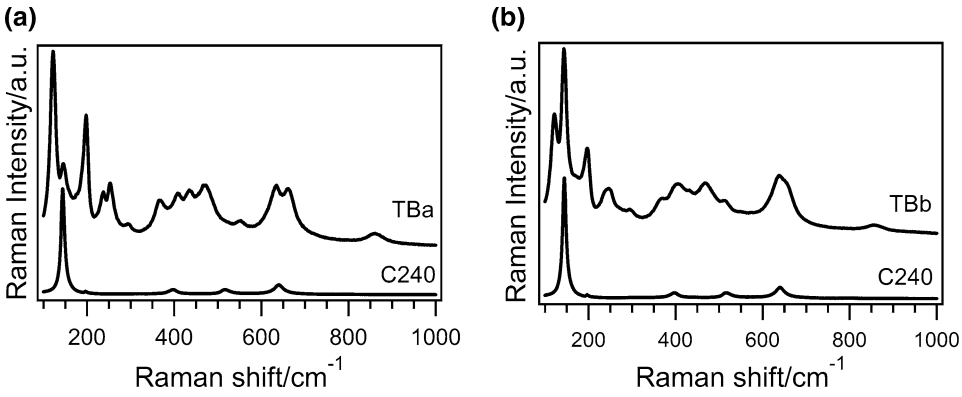

Fig. 2 Raman spectra of samples **a** TBa and **b** TBb. The spectra of phase-pure anatase powder C240 are added for comparison

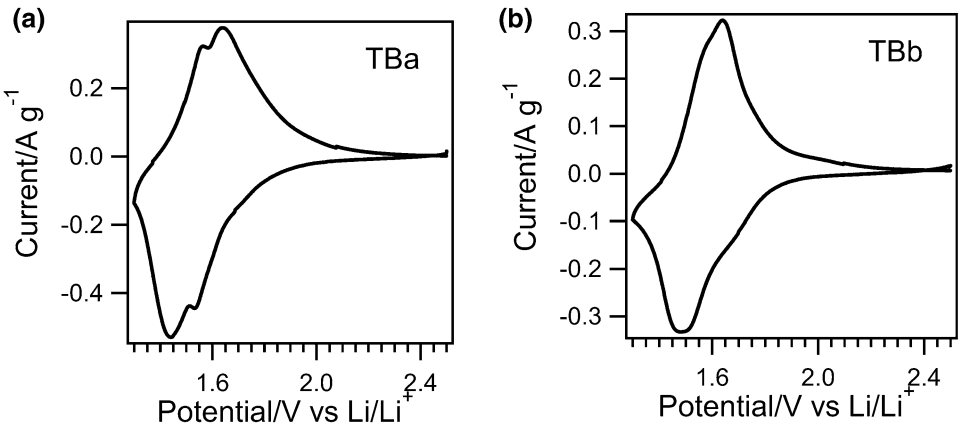

Fig. 3 Cyclic voltammograms of Li insertion into the samples TBa (**a**) and TBb (**b**). Electrolyte: 1 mol/dm^3 $LiClO_4$ in EC/DMC (1/1 w/w), scan rate: 0.2 mV/s

processes induced by Li insertion: (1) improvement of material conductivity [54, 59] and (2) distortion of TiO_2(B) monoclinic structure. However, no new vibrational bands analogous to those reported earlier for anatase [53, 54] are observed during insertion. The extinct Raman spectrum of a TiO_2(B) at low potentials is restored again during Li^+ extraction (the right charts in Fig. 4). Nevertheless, the spectrum of TiO_2(B) (Fig. 4) is recovered at more positive potentials than the potential of TiO_2(B) extraction peak maxima in the corresponding cyclic voltammogram (see Fig. 3a). Hence, certain hysteresis in the insertion/extraction processes is observed. A similar tendency was observed in spectra recorded analogously for the sample TBb. However, new features in spectra were detected during Li^+ insertion into TBb material. From Fig. 5 (left charts) it is obvious, that two new peaks localized at 166 and 180 cm^{-1} are present at potentials between 1.81 and 1.67 V. With gradual potential decrease these vibrational bands disappear together with all Raman modes of TiO_2(B). The response of the TBb sample to Li^+ extraction is different compared to TBa sample (Figs. 4 right, 5 right). The spectrum of TBb electrode is similar to that of pure electrolyte at potentials about 1.4 V. Vibrational bands typical for orthorhombic lithium titanate appear with increasing potential until 1.89 V [30, 52–55, 60]. Subsequently the Raman features of TiO_2(B) become more visible. The mixture of both phases is observable at potentials about 1.96–2.35 V. Finally a standard TiO_2(B) spectrum is recovered above 2.42 V. The occurrence of spectrum of lithium titanate during Li^+ insertion/extraction is typical for anatase phase [30, 52–55, 60]. For comparison Raman spectrum of orthorhombic Li_xTiO_2 formed during Li insertion into phase-pure anatase material C240 is presented in Fig. 6 (electrolyte signals are subtracted). The lower intensity of the Raman modes of orthorhombic lithium titanate during insertion is apparently caused by decrease of the overall signal of material due to enhanced TiO_2(B) conductivity in this potential range. On the other hand, the recovery of both TiO_2(B) (Fig. 4, left chart) and anatase spectra during Li^+ extraction starts at more positive potentials [53, 54]. This enables an easy identification of orthorhombic phase at lower potentials. Hence, anatase impurities in TBb sample manifest themselves by occurrence of orthorhombic phase in the spectrum during Li^+ insertion/extraction.

The pretreated RB sample (see "Experimental" section) was characterized by X-ray diffraction (Fig. 7a). Except for rutile pattern there is a small almost undistinguishable peak at about 25° (2θ) perhaps indicating a presence of anatase in the RB material as well (see inset in Fig. 7a).

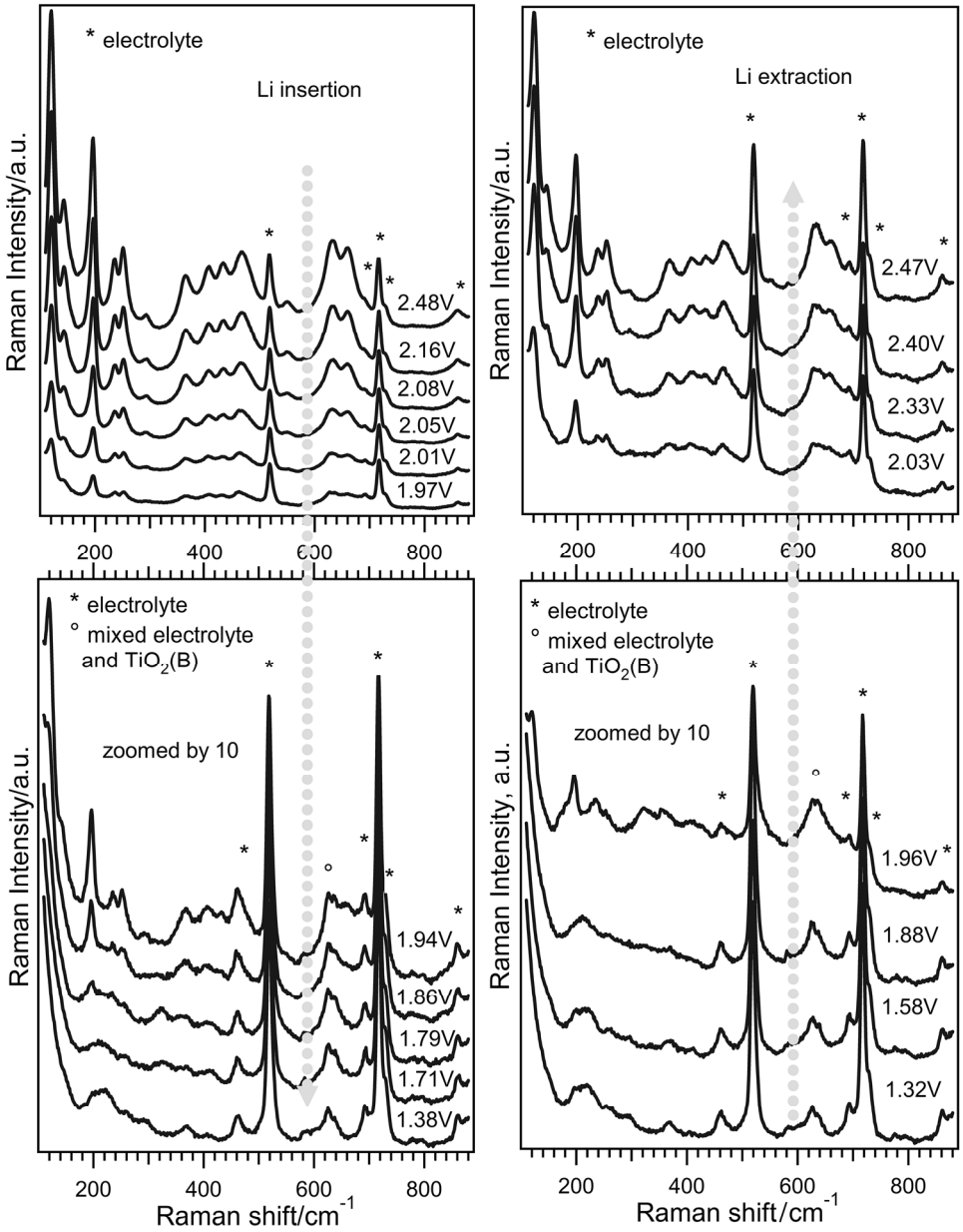

Fig. 4 In situ Raman spectra of the TBa electrode in 1 M $LiClO_4$ + EC/DMC (1/1) during cyclic voltammetry at scan rate of 0.2 mV/s. The *left charts* depict the spectra for Li insertion (from *top to bottom*). The *right charts* (*bottom to top*) show reverse process, Li extraction. The average potentials from potential sweeps corresponding to each spectrum recording are depicted. The intensity scale is zoomed by a factor of 10 in the two *bottom charts*. The spectra are offset for clarity, but the intensity scale is identical in *each chart*

The Raman spectrum of RB powder exhibits features of rutile too (see Fig. 7b). The rutile vibrational band B_{1g} at 144 cm^{-1} is still subject of contradictory discussions due to its different intensity observed as compared to other vibrational modes of rutile [61, 62]. This peak was assigned to anatase impurities in some studies [49]; however, the existence of rutile Raman mode B_{1g} at the same wavenumber was calculated and observed too [48, 63]. In addition, Cheng et al. [64] observed a variable intensity and position of this vibrational band of rutile for different nanocrystals size in the past.

RB material was studied by in situ Raman spectroelectrochemistry. The Raman spectra of RB were measured during cyclic voltammetry of Li^+ insertion at a scan rate 0.5 mV/s (see "Experimental" section for detail). Figure 8 shows corresponding cyclic voltammogram exhibiting features specific for TiO_2 rutile [11, 65]. No other peaks assignable to Li^+ insertion into anatase structure are present [3, 53]. Since the cyclic voltammetry of Li^+ insertion was reported to be a very sensitive and reliable technique for identification of different phases in TiO_2 powder [21], one can take the phase purity of RB material proved by this method for virtually granted. However, our refined analysis presented below shows that this is not true.

The in situ Raman spectroelectrochemical data acquired on a RB electrode in $LiClO_4$ + EC/DMC electrolyte solution are shown in Fig. 9. The measurement started from 2.5 V versus Li/Li^+. The initial spectrum is

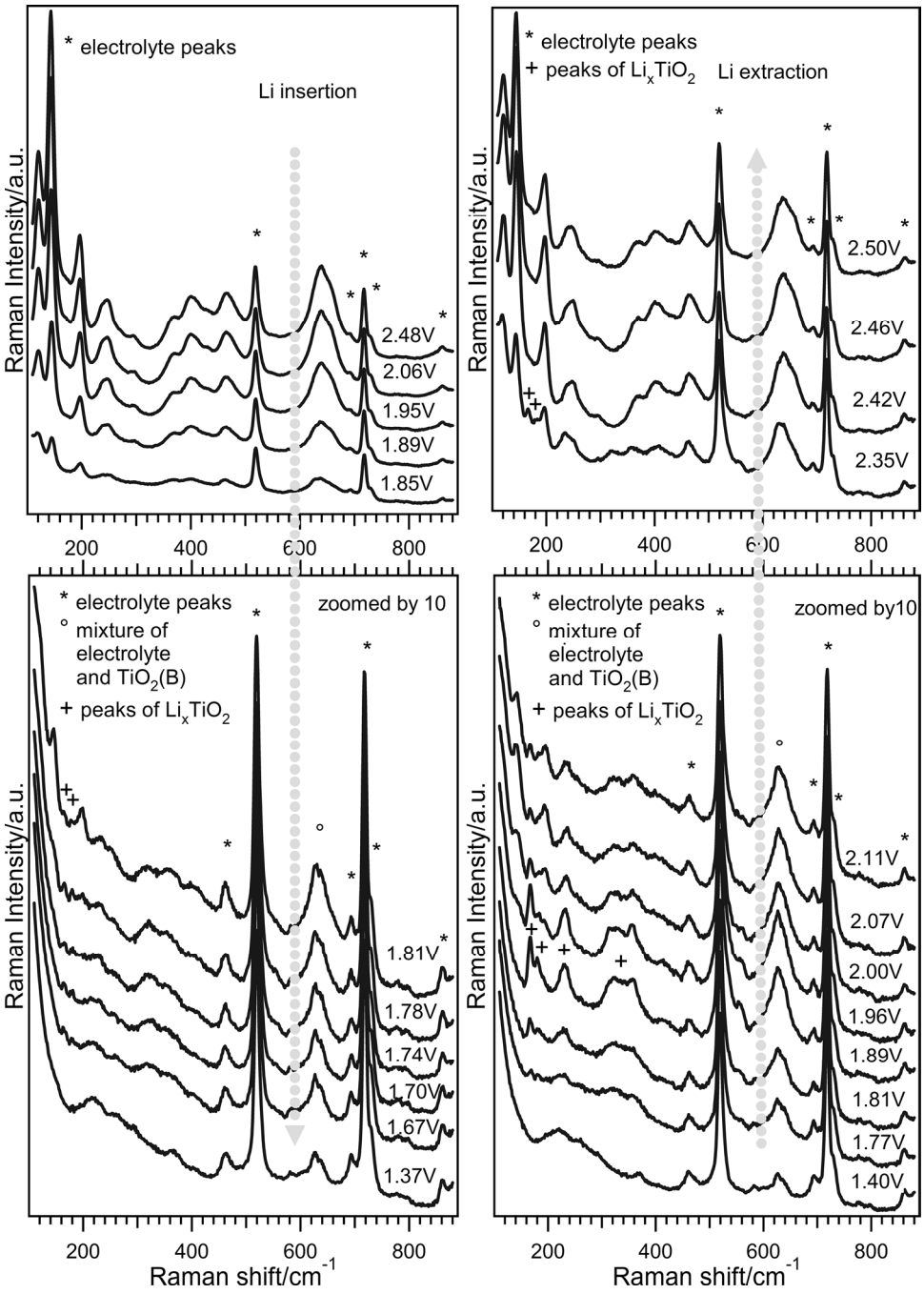

Fig. 5 In situ Raman spectra of the TBb electrode in 1 M $LiClO_4$ + EC/DMC (1/1) during cyclic voltammetry at scan rate of 0.2 mV/s. The *left charts* depict the spectra for Li insertion (from *top to bottom*). The *right charts* (*bottom to top*) show reverse process, Li extraction. The average potentials from potential sweeps corresponding to each spectrum collection are depicted. The intensity scale is zoomed by a factor of 10 in the two *bottom charts*. The spectra are offset for clarity, but the intensity scale is identical in *each chart*

that of RB rutile in electrolyte. The Raman modes of rutile attenuate during potential decrease and peaks specific for orthorhombic Li_xTiO_2 are observable at potential below 1.68 V. Subsequently, the features of both these phases diminish continuously with negative potential and only electrolyte spectrum is observed at potentials close to 1.3 V. The reverse potential sequence (the right charts in Fig. 9) is characterized by complete recovery of all the RB features seen in the previous insertion potential sweep. In detail, the rutile spectrum recovery by potential increase includes an intermediate step, where both amplifying rutile features and features of orthorhombic lithium titanate are present at the same time. There are two possible explanations of the occurrence of lithium titanate features in Raman spectrum during cyclic voltammetry of Li insertion. The Li-insertion coefficient x for nanocrystalline rutile was reported typically in the range of 0.1–0.5. Hence a possible explanation of the presence of orthorhombic Li_xTiO_2 phase in RB could be the phase transition of rutile structure to lithium titanate.

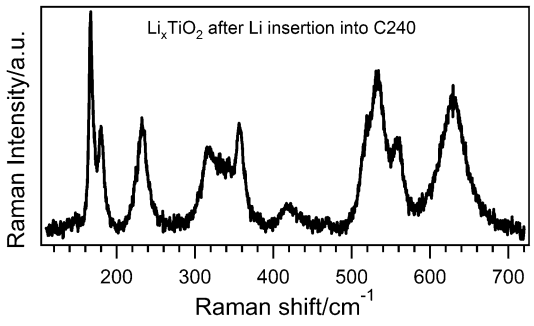

Fig. 6 In situ Raman spectrum of orthorhombic lithium titanate Li_xTiO_2 observed on phase-pure anatase C240 electrode during Li insertion (the electrolyte signal was subtracted)

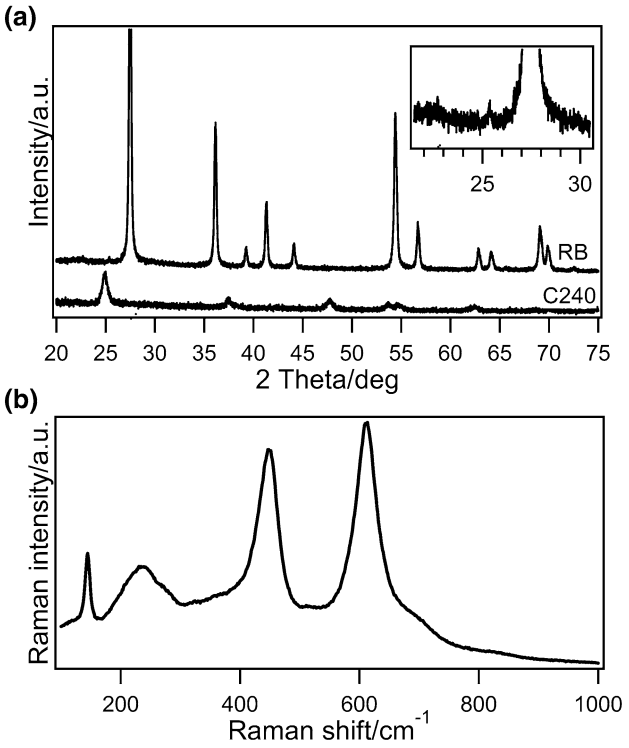

Fig. 7 X-ray diffractogram (**a**) and Raman spectrum (**b**) of the sample RB

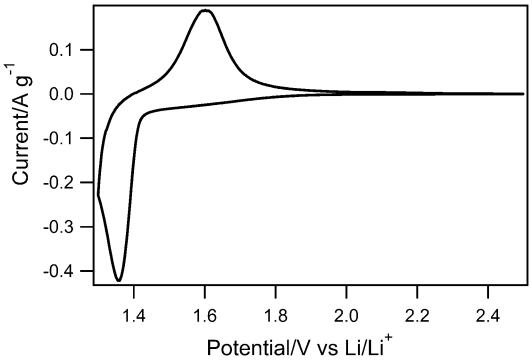

Fig. 8 Cyclic voltammogram of Li insertion in the sample RB. Electrolyte: 1 mol/dm^3 $LiClO_4$ in EC/DMC (1/1 w/w), scan rate: 0.5 mV/s

However, this is not in agreement with our observations if we expect a similar behavior both for rutile and phase-pure anatase. The changes in Raman spectrum for anatase electrode occur at the lithium insertion coefficient of 0.05 or higher [30, 53–55]. Nevertheless, the first features of Li_xTiO_2 are recognizable in RB spectrum at potentials about 1.68 V, which correspond to lithium insertion coefficient lower than 0.01 (Figs. 8, 9). Therefore, the observed forming of orthorhombic phase is caused most likely by anatase impurities in RB sample as in the case of TBb material. This is in agreement with the Raman spectra because the Li_xTiO_2 features are visible in the RB spectrum at potentials lower than the formal potential of Li insertion into anatase and much higher than the formal potential of Li insertion into rutile. The Li_xTiO_2 spectrum is clearly visible for a long range of potentials, because the signal decrease caused by changes in material conductivity is faster at potentials close to Li^+ insertion peak of rutile.

These data demonstrate Raman spectroelectrochemistry as a very sensitive tool for revealing anatase impurities in TiO_2(rutile) and TiO_2(B) materials, especially in cases when methods as XRD and cyclic voltammetry are insufficient. The detection limit of cyclic voltammetry for anatase impurities is in the range of about 5–1 % [28, 66]. As it is generally known, this detection limit is highly dependent on the size of anatase crystals [39, 67]. In cyclic voltammograms the Li insertion peak of anatase is less distinguishable for larger crystal size. On the other hand, Raman bands are better resolved for larger particles, because their amplitude is directly proportional and their width inversely proportional to particle size (or coherent domain size). Therefore, the above presented technique of Raman spectroelectrochemistry is advantageous mainly in the case of lower than 5 % contamination of TiO_2 sample by larger anatase nanocrystals (tens and hundreds nanometers).

Conclusion

In situ Raman spectroelectrochemistry was demonstrated as a sensitive tool for detection of small impurities of anatase phase in other TiO_2 polymorphs. This method was found to be the most reliable to detect traces of anatase phase unequivocally even in the cases where other standard techniques (XRD, CV, or Raman spectroscopy) are insufficient. In addition, in situ Raman spectroelectrochemistry represents a user-friendly analytic method since it is neither time nor material consuming.

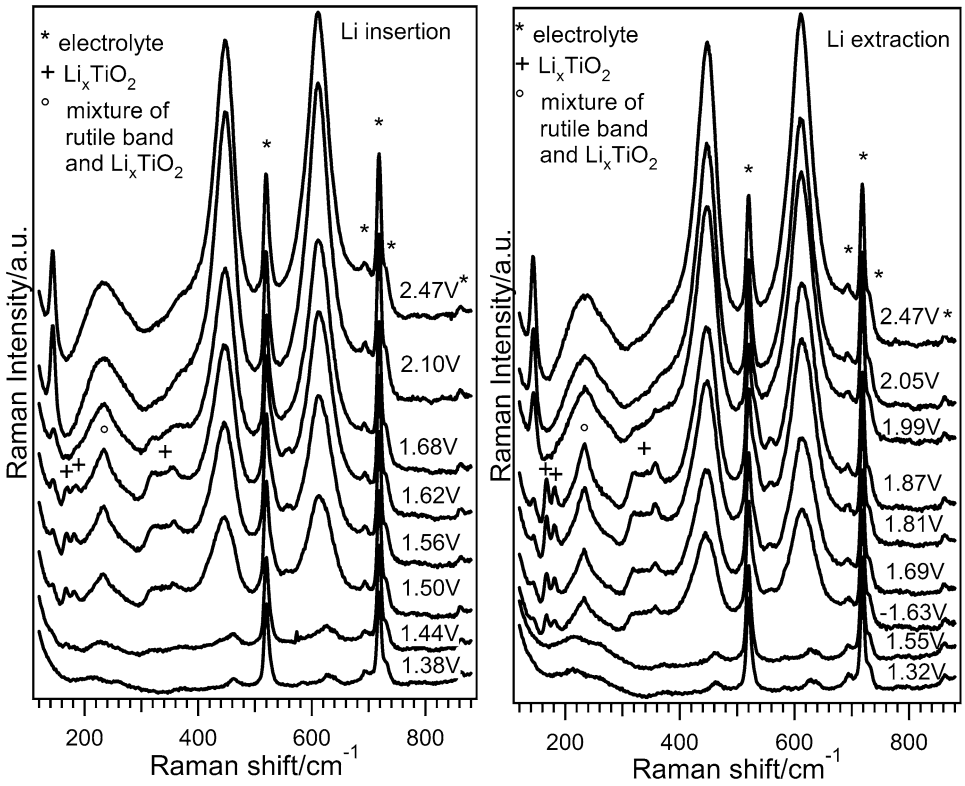

Fig. 9 In situ Raman spectra of the RB electrode in 1 M $LiClO_4$ + EC/DMC (1/1) during cyclic voltammetry at scan rate of 0.5 mV/s. The *left charts* depict the spectra for Li insertion (from *top to bottom*). The *right charts* (*bottom to top*) show reverse process, Li extraction. The average potentials from potential sweeps corresponding to each spectrum collection are depicted. The spectra are offset for clarity, but the intensity scale is identical in *each chart*

Experimental

Preparation of electrodes

The monoclinic TiO_2(B) was synthesized by a method previously reported by Zukalova et al. [21]. Briefly, 10 g of amorphous TiO_2 was mortared with 7.8 g of Cs_2CO_3 (Aldrich). This powder was then calcined at 800 °C for 4 h, mortared again, and heated to 800 °C in a crucible with a tight lid for 48 h to form cesium titanate. Excess of 1 M HCl was added to the solid and stirred vigorously for 4 × 24 h with the fresh acid exchanged every 24 h. The product was finally dried in air. This material is coded as TBa. The second TiO_2(B) material (Lor-035-013B, calcined for 7 h at 400 °C; SusTech GmbH & Co. Kg, Darmstadt, Germany) was available from our previous work [23]; it is coded as TBb. The commercial powder of TiO_2 nanocrystalline rutile PK5556 (Bayertitan, Bayer, Germany) with the Brunauer–Emmett–Teller (BET) surface area, $S_{BET} = 103$ m^2/g was tested too. This rutile material was pretreated for 20 min at 800 °C and is denoted as RB. The nanocrystaline anatase coded as C240 was used as a reference anatase material. The crystal morphology of C240 is characterized by particles ca. 10–20 nm in size exposing mainly the (101) facets [39, 68].

Powder titania samples were dispersed in aqueous medium into a viscous paste. 4 mg of the powder was mixed with 40 mm^3 of 4 % aqueous solution of hydroxypropylcellulose (Aldrich, MW 100,000) and 10 mm^3 of 10 % aqueous solution of Triton-X100 (Fluka), after which 20 mm^3 of H_2O was added. For Raman spectroelectrochemistry, the platinum mesh (4 × 4 mm^2, Goodfellow) served as conductive support and the TiO_2 film was deposited by dip-coating. The coated area was approximately 2 × 4 mm^2 with an edge serving as an electrical contact. For control electrochemical measurements the titanium mesh (7 × 25 mm^2, Goodfellow) was used as conductive support and the coated area was ca 7 × 12 mm^2. All prepared electrodes were dried in air and subsequently calcined in air at 450 °C for 30 min.

Methods

The spectroelectrochemical measurements were carried out in an airtight spectroelectrochemical cell under argon using a μAutolabIII (Metrohm Autolab) controlled by the NOVA 1.5 software. The electrolyte solution was 1 mol/dm^3 $LiClO_4$ in ethylene carbonate (EC) + dimethyl carbonate (DMC) (1/1 w/w). The counter electrode was from Pt metal and the AgCl-coated Ag wire was employed as the pseudoreference electrode. The latter is a convenient reference electrode for in situ Raman spectroelectrochemistry due to its easier use compared to commercial Ag/AgCl electrodes. The potential of our Ag/AgCl-pseudoreference electrode

was calibrated by a control cyclic voltammogram measurement of Li insertion against the usual Li/Li^+ reference electrode in a glove box under Ar atmosphere (in 1 M $LiClO_4$). Our Ag/AgCl pseudoreference is upshifted by 3.05 V against the Li/Li^+ reference electrode. Electrochemical data in the text are presented in relation to Li/Li^+ potential reference. The Raman spectra were measured on a MicroRaman system (LabRAM HR spectrometer, Horiba Jobin–Yvon) interfaced to an Olympus BX microscope (objective 50×). The spectra were excited by a He–Ne laser, 633 nm, power 4.7 mW. The Raman spectrometer was calibrated before each set of measurements using the F_{1g} line of Si at 520.2 cm^{-1} as a reference.

The in situ Raman spectra were measured during cyclic voltammetry (CV). The CV scan rate was 0.5 mV/s for RB and 0.2 m V/s for TBa and TBb samples. Each spectrum was collected for 2 min in the case of RB material, which corresponded to two 60 s accumulations. Four accumulations (45 s each) were used for spectra of TBa and TBb electrodes with 5 s intervals between spectral acquisition. The potentials presented in the spectroelectrochemical studies are average potentials from the potential sweep corresponding to the respective spectrum collection. Powder XRD was studied on a Bruker D8 Advance diffractometer using Cu Kα radiation. BET surface area of the samples was determined from nitrogen adsorption isotherm measurements at $T = -196$ °C (ASAP 2010, Micromeritics).

Acknowledgments This work was supported by the Grant Agency of the Czech Republic (Contract No. 15-06511S).

References

1. Fujishima A, Honda K (1972) Nature 238:37
2. Kubiak P, Pfanzelt M, Geserick J, Hormann U, Husing N, Kaiser U, Wohlfahrt-Mehrens M (2009) J Power Sourc 194:1099
3. Bousa M, Laskova B, Zukalova M, Prochazka J, Chou A, Kavan L (2010) J Electrochem Soc 157:A1108
4. Froeschl T, Hoermann U, Kubiak P, Kucerova G, Pfanzelt M, Weiss CK, Boehm RJ, Husing N, Kaiser U, Landfester K, Wohlfahrt-Mehrens M (2012) Chem Soc Rev 41:5313
5. Kavan L (2012) Chem Rec 12:131
6. O'Regan B, Grätzel M (1991) Nature 353:737
7. Hagfeldt A, Boschloo G, Sun L, Kloo L, Pettersson H (2010) Chem Rev 110:6595
8. Henderson MA (2011) Surf Sci Rep 66:185
9. Chen HH, Nanayakkara CE, Grassian VH (2012) Chem Rev 112:5919
10. Lam SW, Soetanto A, Amal R (2009) J Nanopart Res 11:1971
11. Kavan L, Fattachova D, Krtil P (1999) J Electrochem Soc 146:1375
12. Chen X, Mao SS (2007) Chem Rev 107:2891
13. Diebold U (2003) Surf Sci Rep 48:5
14. Liu G, Yang HG, Pan J, Yang YQ, Lu GQ, Cheng H-M (2014) Chem Rev 114:9559
15. Yella A, Lee HW, Tsao HN, Yi CY, Chandiran AK (2011) Science 334:1203
16. Gratzel M (2014) Nat Mater 13:838
17. Ahmed AY, Kandiel TA, Oekermann T, Bahnemann D (2011) J Phys Chem Lett 2:2461
18. Shiraishi Y, Hirakawa H, Togawa Y, Sugano Y, Ichikawa S, Hirai T (2013) ACS Catal 3:2318
19. Zhang YQ, Fu Q, Xu QL, Yan X, Zhang RY, Guo ZD, Du F, Wei YJ, Zhang D, Chen G (2015) Nanoscale 7:12215
20. Marchand R, Brohan L, Tournoux M (1980) Mater Res Bull 15:1129
21. Zukalova M, Kalbac M, Kavan L, Exnar I, Grätzel M (2005) Chem Mater 17:1248
22. Armstrong G, Armstrong AR, Canales J, Bruce PG (2006) Electrochem Solid State Lett 9:A139
23. Kavan L, Kalbac M, Zukalova M, Exnar I, Lorenzen V, Nesper R, Grätzel M (2004) Chem Mater 16:477
24. Laskova B, Zukalova M, Zukal A, Bousa M, Kavan L (2014) J Power Sourc 246:103
25. Kobayashi M, Petrykin VV, Kakihana M (2007) Chem Mater 19:5373
26. Wang JF, Xie JJ, Jiang YM, Zhang JJ, Wang YG, Zhou ZF (2015) J Mater Sci 50:6321
27. Okumura T, Fukutsuka T, Yanagihara A, Orikasa Y, Arai H, Ogumi Z, Uchimoto Y (2011) Chem Mater 23:3636
28. Prochazka J, Kavan L, Zukalova M, Frank O, Kalbac M, Zukal A, Klementova M, Carbone D, Graetzel M (2009) Chem Mater 21:1457
29. Prochazka J, Kavan L, Shklover V, Zukalova M, Frank O, Kalbac M, Zukal A, Pelouchova H, Janda P, Mocek K, Klementova M, Carbonne D (2008) Chem Mater 20:2985
30. Gentili V, Brutti S, Hardwick LJ, Armstrong AR, Panero S, Bruce PG (2012) Chem Mater 24:4468
31. Nakade S, Saito Y, Kubo W, Kitamura T, Wada Y, Yanagida S (2003) J Phys Chem B 107:8607
32. Sang L, Zhao Y, Burda C (2014) Chem Rev 114:9283
33. De Marco L, Manca M, Buonsanti R, Giannuzzi R, Malara F, Pareo P, Martiradonna L, Giancaspro NM, Cozzoli PD, Gigli G (2011) J Mater Chem 21:13371
34. Sabyrov K, Burrows ND, Penn RL (2013) Chem Mater 25:1408
35. Zhu SC, Xie SH, Liu ZP (2015) J Am Chem Soc 137:11532
36. Armstrong AR, Armstrong G, Canales J, Bruce PG (2004) Angew Chem Int Ed 43:2286
37. Beuvier T, Richard-Plouet M, Mancini-Le Granvalet M, Brousse T, Crosnier O, Brohan L (2010) Inorg Chem 49:8457
38. Dylla AG, Xiao P, Henkelman G, Stevenson KJ (2012) J Phys Chem Lett 3:2015
39. Kavan L, Grätzel M, Rathousky J, Zukal A (1996) J Electrochem Soc 143:394
40. O'Regan B, Grätzel M, Fitzmaurice D (1991) Chem Phys Lett 183:89
41. Kavan L, Grätzel M, Gilbert SE, Klemenz C, Scheel HJ (1996) J Am Chem Soc 118:6716
42. Laskova B, Moehl T, Kavan L, Zukalova M, Liu XJ, Yella A, Comte P, Zukal A, Nazeeruddin MK, Graetzel M (2015) Electrochim Acta 160:296
43. Elgh B, Palmqvist AEC (2015) J Sol-Gel Sci Technol 76:395
44. Nakade S, Matsuda M, Kambe S, Saito Y, Kitamura T, Sakata T, Wada Y, Mori H, Yanagida S (2002) J Phys Chem B 106:10004
45. Mansfeldova V, Laskova B, Krysova H, Zukalova M, Kavan L (2014) Catal Today 230:85
46. Zhang J, Liu PL, Lu ZD, Xu GL, Wang XY, Qian LS, Wang HB, Zhang EP, Xi JH, Ji ZG (2015) J Alloys Compd 632:133
47. Kavan L, Zukalova M, Vik O, Havlicek D (2014) ChemPhysChem 15:1056
48. Frank O, Zukalova M, Laskova B, Kürti J, Koltai J, Kavan L (2012) Phys Chem Chem Phys 14:14567

49. Swamy V (2008) Phys Rev B 77:195414
50. Armstrong AR, Armstrong G, Canales J, Bruce PG (2005) J Power Sourc 146:501
51. Lan TB, Dou J, Xie FY, Xiong PX, Wei MD (2015) J Mater Chem A 3:10038
52. Smirnov M, Baddour-Hadjean R (2004) J Chem Phys 121:2348
53. Laskova B, Frank O, Zukalova M, Bousa M, Dracinsky M, Kavan L (2013) Chem Mater 25:3710
54. Hardwick LJ, Holzapfel M, Novak P, Dupont L, Baudrin E (2007) Electrochim Acta 52:5357
55. Ren Y, Hardwick LJ, Bruce PG (2010) Angew Chem Int Ed 49:2570
56. Zhuang W, Lu L, Wu X, Jin W, Meng M, Zhu Y, Lu X (2013) Electrochem Commun 27:124
57. Santara B, Giri PK, Imakita K, Fujii M (2013) Nanoscale 5:5476
58. Dylla AG, Lee JA, Stevenson KJ (2012) Langmuir 28:2897
59. Itoh T, Sato H, Nishina T, Matue T, Uchida I (1997) J Power Sourc 68:333
60. Baddour-Hadjean R, Bach S, Smirnov M, Pereira-Ramos JP (2004) J Raman Spectrosc 35:577
61. Kavan L, Zukalova M, Ferus M, Kürti J, Koltai J, Civis S (2011) Phys Chem Chem Phys 13:11583
62. Kuznetsov VN, Ryabchuk VK, Emeline AV, Mikhaylov RV, Rudakova AV, Serpone N (2013) Chem Mater 25:170
63. Lan T, Tang XL, Fultz B (2012) Phys Rev B 85:094305
64. Cheng H, Ma J, Zhao Z, Qi L (1995) Chem Mater 7:663
65. Hu YS, Kienle L, Guo YG, Maier J (2006) Adv Mater 18:1421
66. Kavan L, Grätzel M (2002) Electrochem Solid State Lett 5:A39
67. Kavan L, Murakami TN, Comte P, Grätzel M (2007) Electrochem Solid State Lett 10:A85
68. Laskova B, Zukalova M, Kavan L, Chou A, Liska P, Wei Z, Bin L, Kubat P, Ghadiri E, Moser JE, Gratzel M (2012) J Solid State Electrochem 16:2993

Appendix 5

Markéta Zukalová, Barbora Pitňa Lásková, Mariana Klementová and Ladislav Kavan. "Na insertion into nanocrystalline $Li_4Ti_5O_{12}$ spinel: An electrochemical study." *Electrochim. Acta*, 2017, **245**, 505-511.

Electrochimica Acta 245 (2017) 505–511

Contents lists available at ScienceDirect

Electrochimica Acta

journal homepage: www.elsevier.com/locate/electacta

Na insertion into nanocrystalline $Li_4Ti_5O_{12}$ spinel: An electrochemical study

Markéta Zukalová[a,*], Barbora Pitňa Lásková[a,b], Mariana Klementová[c], Ladislav Kavan[a]

[a] J. Heyrovský Institute of Physical Chemistry, The Czech Academy of Sciences, v.v.i. Dolejškova 3, CZ-18223 Prague 8, Czech Republic
[b] Department of Inorganic Chemistry, Faculty of Science, Charles University, Hlavova 2030/8, CZ-128 43 Prague 2, Czech Republic
[c] Institute of Physics of the Czech Academy of Sciences, v.v.i., Na Slovance 2, 182 21 Prague, Czech Republic

ARTICLE INFO

Article history:
Received 20 November 2016
Received in revised form 20 April 2017
Accepted 24 May 2017
Available online 25 May 2017

Keywords:
Na insertion
$Li_4Ti_5O_{12}$
Nanocrystalline
Spinel
Charge capacity

ABSTRACT

Na insertion into sol-gel made nanocrystalline spinel, $Li_4Ti_5O_{12}$ (nano LTS) and reference commercial spinel (Aldrich LTS) is studied by cyclic voltammetry and galvanostatic chronopotentiometry at 1C and 2C charging/discharging rates. Nanocrystalline LTS exhibits the best performance for Na storage, its charge capacities reach 156 mAhg ^{1} and are twice as high as those of reference Aldrich LTS. A capacity drop of nano LTS taking place during galvanostatic cycling is ascribed to irreversible structural changes induced by Na accommodation in the $Li_4Ti_5O_{12}$ lattice. Raman spectroscopy of nano LTS after Na insertion reveals a formation of orthorhombic $Li_{0.5}TiO_2$ phase in original nanocrystalline $Li_4Ti_5O_{12}$. The occurrence of this phase, which is commonly formed during Li insertion into anatase, is discussed in terms of induced Li redistribution and its accommodation in very minor anatase impurities detectable by Raman spectroelectrochemistry and HRTEM, but visible neither by X-ray diffractometry nor cyclic voltammetry of Na insertion.

1. Introduction

Recent boom of all kinds of portable electronic devices improving quality of our daily life places at the same time demands on availability of suitable electrochemical energy storage systems with respect to their charge capacity, charging rate, safety, reliability and price. The state of the art lithium-ion batteries meet almost all above requirements, nevertheless due to limited lithium resources and higher cost, the Na-storage based systems have made a comeback. The issue is not insufficient lithium global reserve, but what fraction can be used and still be economically effective [1]. The use of Na instead of Li in batteries could mitigate the feasible shortage of lithium in an economic way, due to the larger sodium sources, the ease to recover it, and its lower price. Moreover, for electrode materials sodium insertion chemistry is very similar to Li, which enables to use the same compounds for both kinds of systems.

In recent years there have been numerous attempts to explore anode materials for sodium ion batteries. The ion radius of sodium (1.02 Å) is larger than that of lithium (0.76 Å), hence, Na-ions accommodation occurs only for host materials with large interlayer spacing [2]. On the contrary to several types of TiO_2 polymorphs and ternary oxides being introduced as alternative anode materials to graphite in rechargeable lithium batteries only few of them were found to be appropriate for sodium storage as well; monoclinic TiO_2(B) with a relatively open channel structure [2,3], anatase TiO_2 nanotubes with high surface area and unique geometry serving due to good electrode–electrolyte contact as a fast diffusion pathway for electrolyte species during the cation insertion [4–7] and spinel lithium titanate ($Li_4Ti_5O_{12}$, LTS) [8]. LTS is known as a "high potential" zero-strain negative electrode material, because the reversible reaction:

$$Li_4Ti_5O_{12} + 3Li^+ + 3e^- \rightarrow Li_7Ti_5O_{12} \quad (1)$$

takes place at a relatively high potential of 1.55 V vs. Li^+/Li, whereby one can avoid the dendrite problem, which is significant in carbon-based anode materials [8]. A Li-ion battery using the LTS anode has been commercialized, mainly owing to these beneficial properties. LTS should also prevent the Na-dendrite deposition, and LTS should be a promising candidate of a negative electrode material for Na-ion batteries. Kitta et al. [8] found that an Na-substituted LTS phase with about 4-5% larger unit cell volume is generated in pristine LTS during Na insertion and co-exists with $Li_4Ti_5O_{12}$ in a single particle.

$$(Li_3)(LiTi_5)(O_{12}) + xNa^+ \rightarrow (Na_xLi_{3-x})(LiTi_5)(O_{12}) + xLi^+ \ (0 < x < 3) \quad (2)$$

* Corresponding author.
E-mail address: marketa.zukalova@jh-inst.cas.cz (M. Zukalová).

http://dx.doi.org/10.1016/j.electacta.2017.05.161
0013-4686/

$$Li_4Ti_5O_{12} + 3Li^+ + 3e^- \rightarrow Li_7Ti_5O_{12} \quad (3)$$

DFT calculations made by Sun et al. [9] predicted even three-phase separation mechanism,

$$2Li_4Ti_5O_{12} + 6Na^+ + 6e^- \rightarrow Li_7Ti_5O_{12} + Na_6LiTi_5O_{12} \quad (4)$$

which has been confirmed through in-situ synchrotron X-ray diffraction and transmission electron microscopy. Nevertheless, the mechanism of Na- substituted LTS phase formation and its behavior upon cycling remain still unclear [8].

Numerous Li insertion studies into LTS revealed a dependency of its electrochemical behavior on morphology (particle size, surface area). Nanocrystalline LTS spinel made by sol-gel synthesis exhibited in thin film excellent activity toward Li insertion [10], even at charging rates as high as 250C. Optimization of LTS particle size with respect to its electrochemical behavior concluded that the best performance of thin-film $Li_4Ti_5O_{12}$ electrodes is achieved, if the parent materials have surface areas between ca. 20 to 110 m^2g^{-1}, with the maximum at ca. 100 m^2g^{-1} [11,12].

Due to the above mentioned similarity in Li and Na insertion behavior, one could expect an enhanced Na insertion ability for the sol-gel made LTS with large surface area too. In addition, faster electrochemical response of nanocrystalline particles could better separate and identify a course of the two mentioned processes taking place during Na insertion into LTS. This was a motivation for our study.

2. Experimental section

2.1. Materials

$Li_4Ti_5O_{12}$ nanocrystalline spinel (nano LTS) was synthesized according to our previously published procedure [10,11]. Briefly: 1.34 M solution of lithium methoxide (LiOMe, Aldrich) in absolute ethanol was mixed with a stoichiometric amount (4/5) of titanium (IV) isopropoxide ($Ti(OPr)_4$; Aldrich) or titanium (IV) n-butoxide, ($Ti(OBu)_4$; Aldrich). The solution was hydrolyzed and concentrated on rotary evaporator (40 °C, 20 mbar) to a concentration of 10–20 wt%. Polyethylene glycol (molecular weight 20 000, Merck) was added in the proportion of 100-150% of the weight of $Li_4Ti_5O_{12}$, and the mixture was stirred overnight. Resulting slurry was then calcined at 500 °C 1 hour. Reference LTS material was purchased from Aldrich (Aldrich LTS). Electrodes were prepared by dip-coating of Ti-mesh (20 × 5 mm^2, Goodfellow) into ethanolic suspension of active material followed by calcination at 450 °C for 30 min. The powder samples for Raman measurement were peeled off from the electrodes already tested by cyclic voltammetry of Na insertion and finally kept at a potential of 0.4 V vs Na/Na^+ (1 M) reference electrode for 8 hours, washed by diethylcarbonate (DEC) and dried under argon atmosphere. A material coded as C240 was used as an anatase standard for Raman measurements. It is a nanocrystalline anatase with a S_{BET} of 89 m^2g^{-1}, prepared by hydrolysis of titanium tetra(isopropoxide) and hydrothermal recrystallization at 240 °C [13]. The C240 has particles ca. 10–20 nm in size exposing mainly the {101} facets.

2.2. Methods

The BET surface areas of the prepared materials were determined from nitrogen adsorption isotherms at 77 K (ASAP 2020, Micromeritics). Powder X-ray diffraction (XRD) was studied on a Bruker D8 Advance diffractometer using CuKα radiation. Electrochemical measurements were carried out in a one-compartment cell using an Autolab Pgstat-302N (Metrohm) controlled by GPES-4 and Nova 2.1 software. The Na-insertion experiments were carried out in 1 M $NaPF_6$ + ethylene carbonate (EC)/diethylcarbonate (DEC) (1/1 by volume) in a glove box with an argon atmosphere. Reference and auxiliary electrodes were Na metal, hence, the potentials are referred to as the Na/Na^+ (1 M) reference electrode. Electrolytes, solvents, and redox-active molecules were of standard quality (p.a. or electrochemical grade) purchased from Aldrich or Merck and used as received. Raman spectra were measured on MicroRaman system (LabRAM HR spectrometer, Horiba Jobin-Yvon) with microscope Olympus BX. The spectra were excited by a He-Ne laser (633 nm). The spectra of powder samples were measured in hermetically closed optical cell to avoid any contact to air. The Raman spectrometer was calibrated

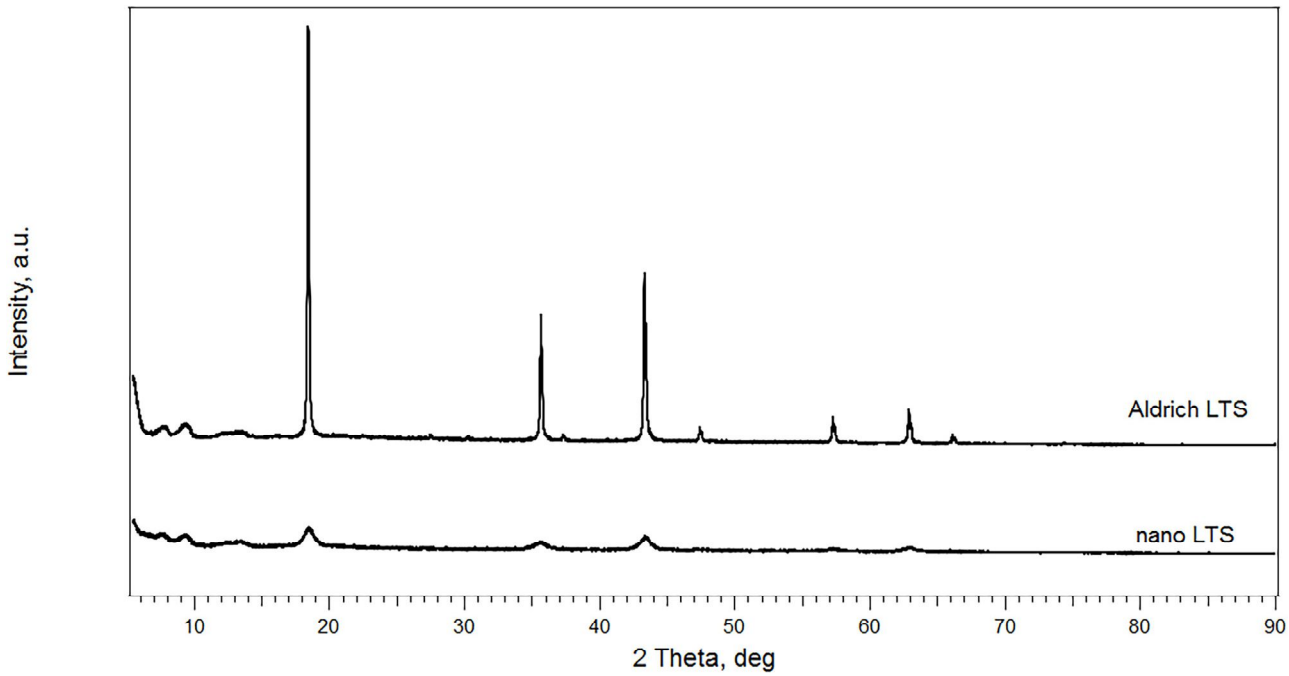

Fig. 1. X-ray diffractogram of nano LTS and Aldrich LTS.

before measurements using the F_{1g} line of Si at 520.2 cm^{-1} as a reference. Transmission electron microscopy (TEM) was carried out on an FEI Tecnai TF20 X-twin microscope operated at 200 kV (FEG, 1.9 Å point resolution). Images were recorded on a CCD camera with resolution of 2048 × 2048 pixels. The HRTEM (high resolution TEM) images were processed in the Digital Micrograph software package using fast Fourier transformation (FFT) mask and inverse FFT to map out selected spatial frequencies in the images. Powder samples for TEM analysis were dispersed in distilled ethanol and the suspension was treated in ultrasound for 5 minutes. A drop of dilute suspension was placed on a holey-carbon-coated copper grid and allowed to dry by evaporation at ambient temperature.

3. Results and Discussion

X-ray diffractograms of nano LTS and reference Aldrich LTS are shown in Fig. 1 and confirm the presence of cubic $Li_4Ti_5O_{12}$ (space group *Fd*-3*m*). No features of other phases are visible in the diffractogram. The crystal sizes estimated from the X-ray linewidth according to Scherrer formula match roughly the values calculated from BET surface area. Assuming spherical particles, the size of nano crystalline LTS (S_{BET} of 162 m^2g^{-1}) and Aldrich LTS (S_{BET} of 12.5 $m^2 g^{-1}$) particles are about 10 and 140 nm, respectively. Further characteristics of sol-gel made nanocrystalline LTS including lattice constant determination by Rietveld refinement were reported earlier [10,11]. Cyclic voltammetry (CV) of the Na insertion of nano LTS and Aldrich LTS was measured in the potential window of 0.4/2.5 V at different scan rates.

Fig. 2 displays cyclic voltammograms of Na-insertion into the samples nano LTS and Aldrich LTS collected with a scan rate 0.1 mVs^{-1}. The voltammogram of sample nano LTS exhibits cathodic peak at 0.81 V and a pair of anodic peaks at 0.91 and 0.98 V, the voltammogram of Altair LTS shows a pair of cathodic peaks at 0.77 V and 0.92 V and a pair of anodic peaks at 0.9 V and 1.06 V. The peak-to-peak splitting (ΔEp) is obviously smaller for nano LTS compared to that of Aldrich LTS (Fig. 2). This splitting is known to decrease with to S_{BET} of TiO_2 anatase [14] and provided a qualitative indication of improved Na-insertion ability of the nanocrystalline material. Charge capacities calculated from the extraction branch of cyclic voltammogram were 156 $mAhg^{-1}$ and 75 mAh g^{-1} for nano LTS and Aldrich LTS, respectively. The found capacity of nano LTS is close to the theoretical value calculated from equation (2) for the insertion coefficient x = 3. Na insertion into Aldrich LTS is hindered due to large particle size and even for the slowest scan rate, 0.1 mVs^{-1} reaches only half of that of nanocrystalline sample.

Chronopotentiometric measurements confirm that Na insertion into nano LTS is substantially facilitated due to nanometer sized particles. Galvanostatic charging at the 1C rate (Fig. 3) provided nano LTS charge capacities of 158 mAh g^{-1} (charge) and 131 mAh g^{-1} (discharge) and at the 2C rate capacities of 149 mAh g^{-1} (charge) and 119 mAh g^{-1} (discharge). Aldrich LTS evaluated at the same charging rates provided at 1C charge capacities of 43 and 25 mAh g^{-1} for charging and discharging, respectively and at 2C capacities of 36 and 22 mAh g^{-1} for charging and discharging, respectively.

A charging stability of both samples was tested by galvanostatic cycling at the 1C and 2C charging rates (Fig. 4). After 25 cycles a capacity of the nano LTS sample decreased by about 70% (1C) and 65% (2C). Despite this relatively large capacity drop of nano LTS sample, its nominal charge capacity after 25 cycles at both charging rates is still comparable with the first cycle capacity of microcrystalline Aldrich LTS sample. On the contrary, a charging capacity of microcrystalline sample exhibits after initial steep drop surprisingly a slight continuous increase during cycling. The 25th cycle capacity is of about 30% higher than the capacity of the 2nd cycle for both charging rates. Whereas an initial capacity drop during cycling for both samples and charging rates can be obviously assigned to forming of solid electrolyte interface (SEI), a reason of subsequent slight capacity increase for Aldrich LTS is unclear.

It is obvious that both capacity decrease of nano LTS and its slight increase for Aldrich LTS are caused by structural changes during cycling. Taking into account the suggested mechanism of Na insertion which is based on induced Li-redistribution [8], one can expect faster and more pronounced structural changes in nanocrystalline LTS. Although a small particle size of this material is generally beneficial for alkali metal insertion, processes taking place on grain boundaries and defects play a more significant role in nanoparticles. Development of Na-substituted LTS phase with larger unit cell volume [8] can be more critical in nanocrystals with lower surface/volume ratio and can result in either disorder in crystalline structure or even structural transformation hindering Na insertion. In our previous works a formal potential determined by cyclic voltammetry of Li insertion was found to be specific parameter of particular TiO_2 polymorph [3,15,16]. Hence cyclic voltammetry of Li insertion can serve as an analytic tool for identification of structural changes. Since one can expect analogous structure/formal potential dependence in the case of Na insertion too, cyclic voltammetry of Na insertion was used as to examine possible structural changes of nano LTS. Fig. 5 depicts

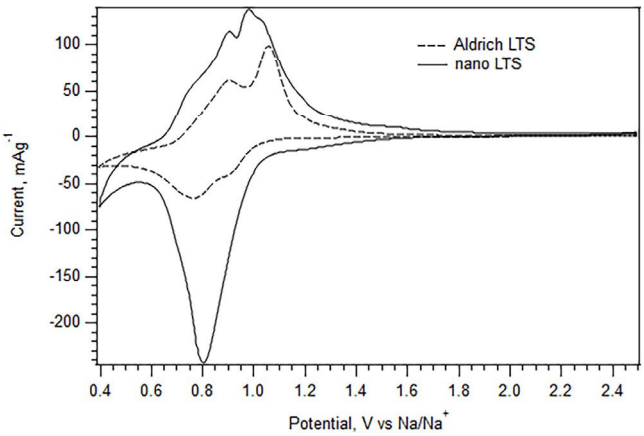

Fig. 2. Cyclic voltammogram of Na insertion in nano LTS (solid line) and Aldrich LTS (dashed line). Electrolyte: 1 M $NaPF_6$ in EC/DEC (1:1). Scan rate 0.1 mVs^{-1}.

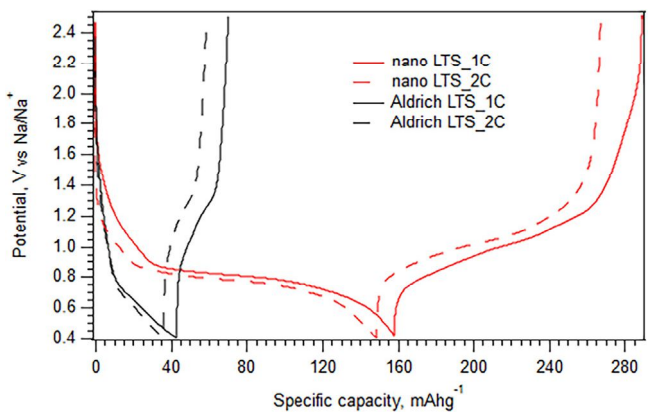

Fig. 3. Galvanostatic chronopotentiometry at charging rates 1C (solid lines) and 2C (dashed lines). Nano LTS (red lines) and Aldrich LTS (black lines).

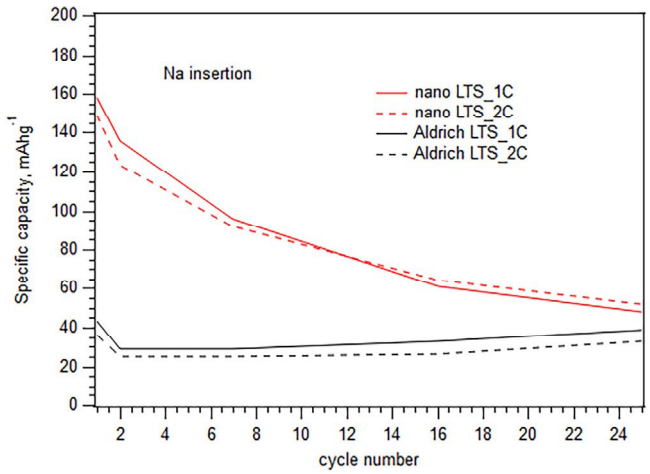

Fig. 4. Galvanostatic cycling (25 cycles) of nano LTS (red lines) and Aldrich LTS (black lines) at charging rates 1C (solid lines) and 2C (dashed lines).

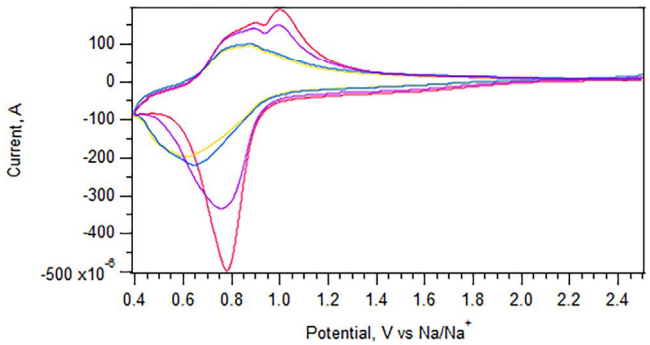

Fig. 5. Comparison of cyclic voltammograms of Na insertion into nano LTS measured on a fresh sample (red curve), after 25 (violet curve), 50 (blue curve) and 75 (yellow curve) cycles at 1C charging rate. Scan rate 0.1 mVs^{-1}.

cyclic voltammograms of Na insertion into fresh nano LTS sample and into samples after galvanostatic cycling at 1C rate. Generally, charging/discharging cycles cause structural changes, which manifest themselves by current peak broadening and shift of both insertion and extraction peak maxima to lower potentials. Nanocrystalline LTS is partially transformed into another phase and its ability to accommodate Na is reduced.

To determine phase composition of nano LTS after galvanostatic cycling at 1C rate, the sample was analyzed by Raman spectroscopy. Fig. 6a shows a comparison of Raman spectra of nano LTS before and after Na insertion. The Raman spectrum of nano LTS after Na insertion exhibits besides the LTS features additional peaks at 167 cm^{-1}, 180 cm^{-1}, 516 cm^{-1}, 532 cm^{-1} and 557 cm^{-1} assignable to orthorhombic titanate, $Li_{0.5}TiO_2$ (space group *Imma*, lattice constants $a = 3.819$ Å, $b = 4.084$ Å, $c = 9.066$ Å). On the contrary, no features of $Li_{0.5}TiO_2$ were observed in the Raman spectrum of Aldrich LTS after Na insertion (data not shown). An occurrence of this phase in Na substituted nano LTS is surprising because it is commonly formed during Li insertion into tetragonal anatase TiO_2 (space group $I4_1/amd$, lattice constants: $a = 3.792$ Å, $c = 9.497$ Å) at certain level of its lithiation ($x \approx 0.5$) (see the Raman spectrum of anatase C240 after Li insertion in Fig. 6a). On the other hand any analogous orthorhombic phase is formed neither during Na insertion into anatase TiO_2 (Fig. 6b) nor during Li insertion into rutile [17]. Hence, the orthorhombic titanate, $Li_{0.5}TiO_2$ in nano LTS after Na insertion is obviously a product of Na induced Li redistribution either into very minor anatase impurities not detectable by XRD and cyclic voltammetry or it is formed in situ on defects sites or grain boundaries from quasi-amorphous nanocrystals exhibiting just short-range ordering and excluding an accommodation of large Na ion. To prove these two hypotheses, detailed analysis of nano LTS by Raman spectroscopy and HRTEM was carried out.

Raman spectroscopy is a useful tool for detection of anatase impurities formed during synthesis which cannot be detected by other usual techniques as XRD and cyclic voltammetry [17]. It is a very sensitive method for revealing even low amount of $Li_{0.5}TiO_2$ after Li insertion [17]. Therefore the detailed analysis of vibrational spectra of nano LTS was made for checking the possibility of local anatase impurities causing the presence of orthorhombic phase in nano LTS after cycling. The Raman spectra from different places of nano LTS powder are presented in Fig. 7. (The spectra were accumulated 5 times longer than spectrum of nano LTS in Fig. 6a). Five Raman active modes ($A_{1g} + E_g + 3F_{2g}$) were predicted for the cubic $Li_4Ti_5O_{12}$ [18–21]. All nano LTS spectra in Fig. 7 show characteristic $Li_4Ti_5O_{12}$ vibrational bands at 229, 272, 345, 429 and 675 cm^{-1} [12,18–24]. The band at 675 cm^{-1} (A_{1g}) was assigned to Ti-O stretching vibration in TiO_6 octahedra [21–23]. The peak at 429 cm^{-1} originates from the stretching vibrational mode of Li-O in LiO_4 tetraedra (E_g) [21–23]. The three Raman modes (F_{2g}) at 345, 272 and 229 cm^{-1} reflect displacement of oxygen atoms and lithium ions motions [21,24]. The next three lines are observed at 760, 514 and 144 cm^{-1}. The narrow peak at 144 cm^{-1} has a variable intensity at different places of nano LTS powder and it is matching with the anatase most intensive vibrational band E_g (1) very well (see Fig. 7). This line can be assigned to small anatase impurities in nano LTS sample. On the base of Fig. 7 we assume the peak at 514 cm^{-1} is an effect of anatase impurities too, however, the Raman band at 514 cm^{-1} was expected to be a line of $Li_4Ti_5O_{12}$ in some studies [21,22,24]. Although the theory doesn't predict any other bands the shoulder to peak at 675 cm^{-1} is usually observed in range of frequencies 740–765 cm^{-1} [12,19,21–24]. The presence of band at 760 cm^{-1} in nano LTS could be explained as a result of breaking the selection rules by disorder effects [21,23].

Due to the fact that long range defects and minor phases present in the untreated sample could be clearly observed by HRTEM [25], this technique was used to complete detailed structure analysis of nano LTS (Fig. 8). Majority of the sample is composed of cubic $Li_4Ti_5O_{12}$ with leaf morphology (Fig. 8a). However, other phases were also detected by electron diffraction and high-resolution TEM. Electron diffraction pattern (Fig. 8b) shows in addition to cubic $Li_4Ti_5O_{12}$ (ICSD-182954) ring pattern highlighted in green also extra diffraction spots belonging to anatase (ICSD-63711) highlighted in red and rutile (ICSD-39166) highlighted in blue. The HRTEM images (Fig. 8c, d) display anatase nanocrystals of about 10 nm in size mapped out using the fast FFT filtering of the corresponding spatial frequencies shown in the inserted FFT.

Hence, the presence of anatase impurities has been proved. The voids in their structure are not able to host large Na ion, on the other hand an accommodation of smaller Li ion in these nanocrystals is still feasible. Nevertheless, during subsequent potential step Li from orthorhombic phase is extracted into electrolyte. Since small vacancies in this structure are not able to accommodate Na in the next insertion step, this phase remains either inactive in charging/discharging process or accommodates another Li from the parent LTS. Finally the ongoing redistribution leads to Li depleting during long term cycling of nano LTS. This gradual process results obviously in partial structure collapse, which manifests itself by Na insertion capacity decrease and changes in cyclic voltammogram. A development of broader peaks with maxima at lower potentials indicates a forming of additional phase with hindered ability to accommodate Na. This process can obviously explain differences in cycling stability between nano and

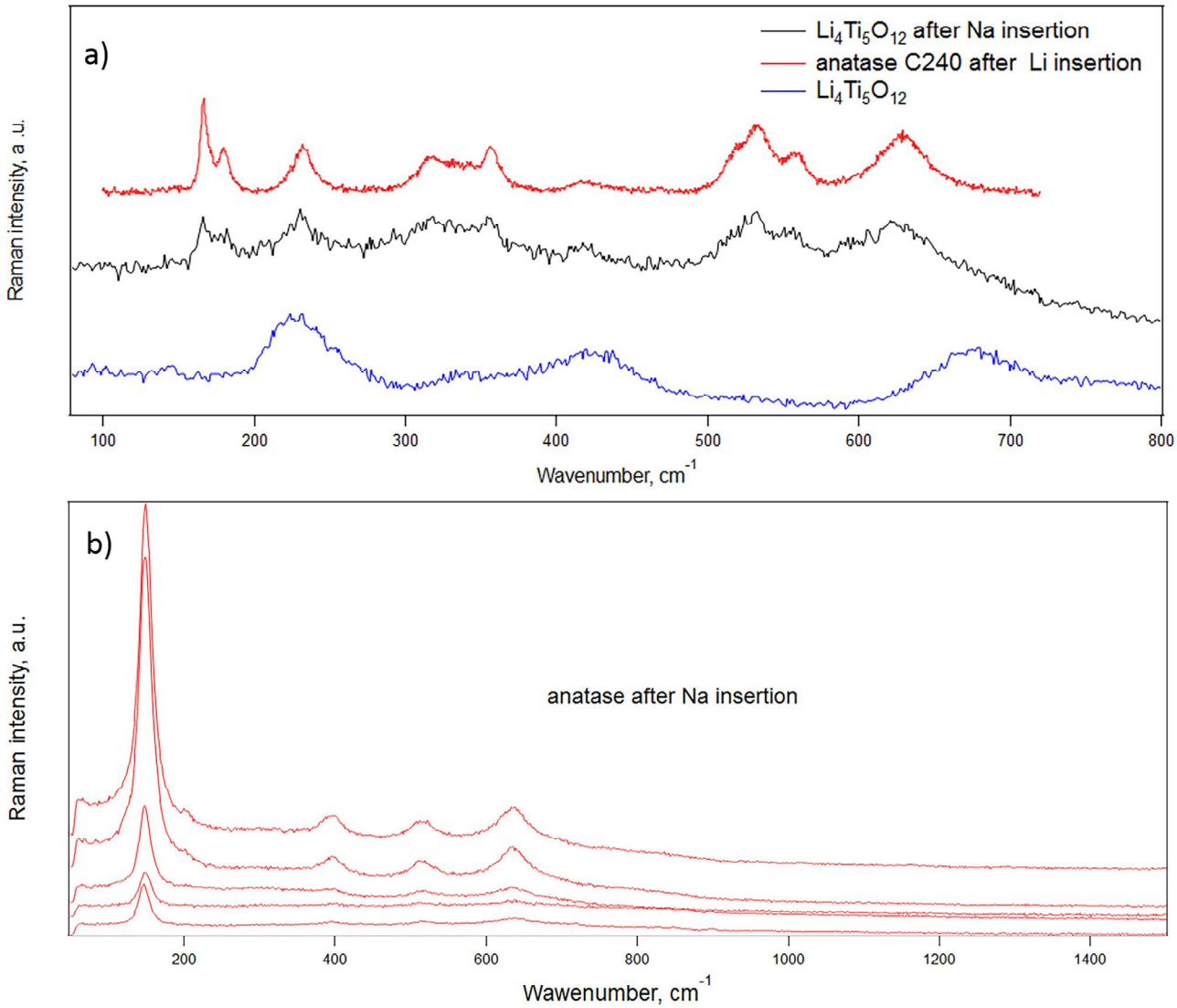

Fig. 6. (a) Comparison of Raman spectrum of pure nano LTS, nano LTS after Na insertion and anatase C240 after Li insertion. (b) Raman spectrum of anatase C240 after Na insertion (different spots of the same sample). Spectra are offset for clarity, but the intensity scale is identical.

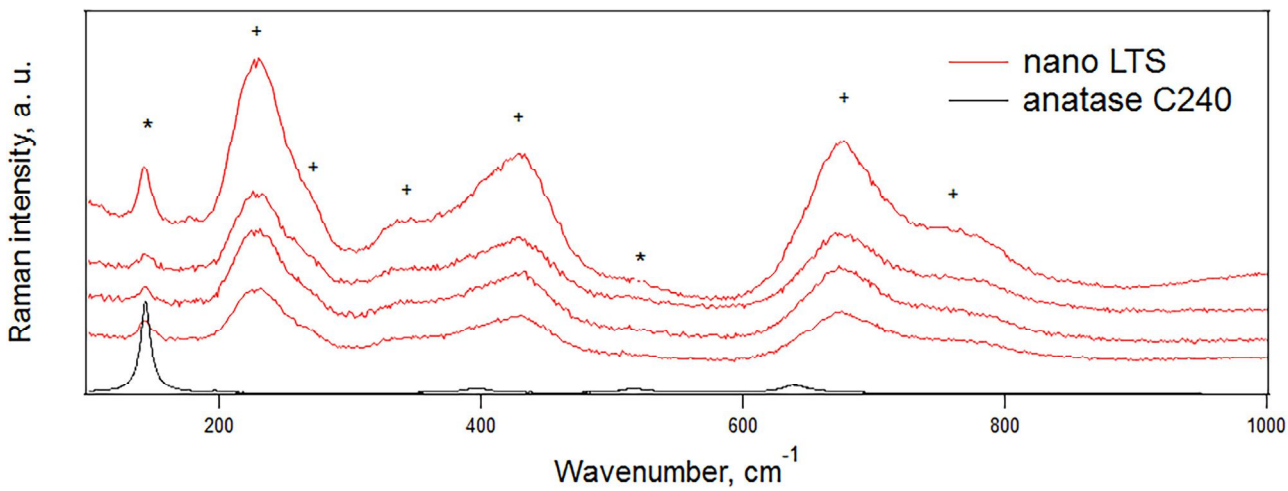

Fig. 7. Raman spectra of anatase C240 (black line) and different parts of nano LTS powder (red lines). Spectra of nano LTS are offset for clarity, but the intensity scale is identical. The Raman bands in nano LTS assigned to $Li_4Ti_5O_{12}$ are labeled by+. The peaks in nano LTS arising from the presence of anatase are labeled by *.

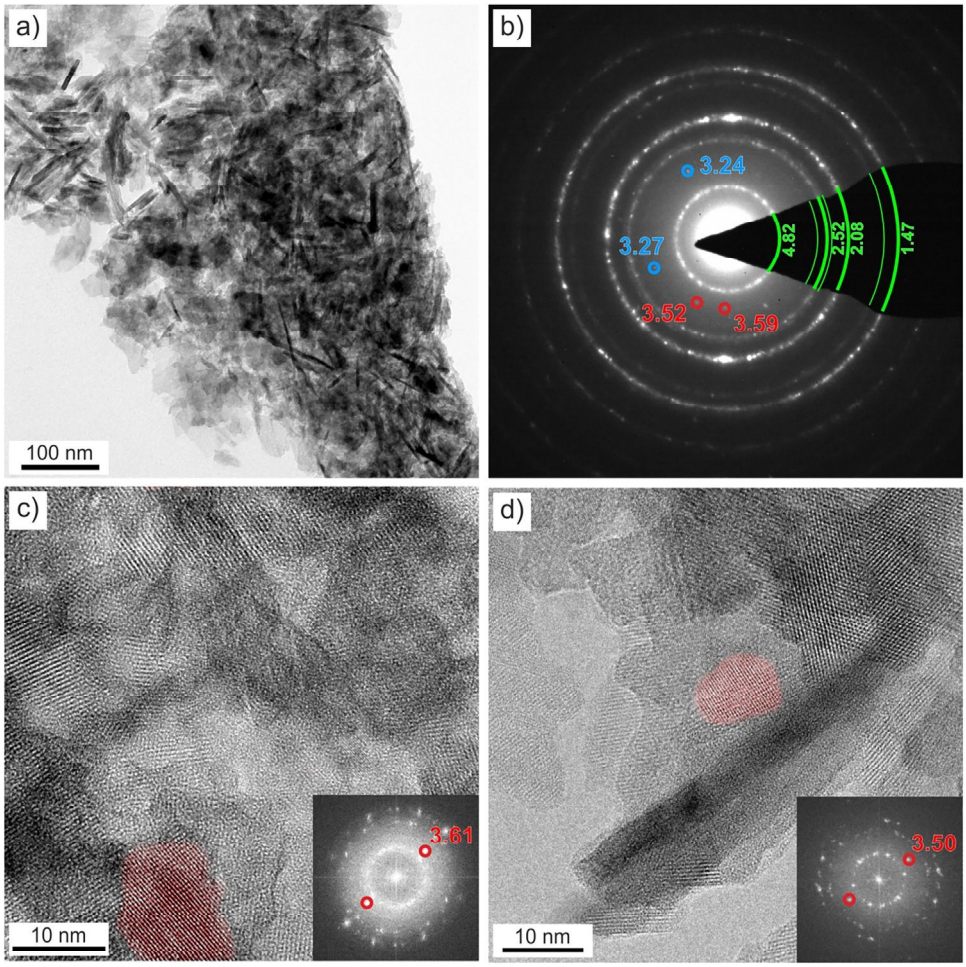

Fig. 8. TEM observations of nano LTS sample. (a) bright-field TEM image, (b) electron diffraction of area shown in (a) with the assigned phases ($Li_4Ti_5O_{12}$ – green, anatase – red, rutile – blue), (c, d) HRTEM image with mapped anatase crystals in red (FFT inserted with anatase spatial frequencies circled in red).

Aldrich LTS. Whereas large particles of Aldrich LTS withstand volume changes accompanying forming Na-substituted LTS phase with an about 4-5% larger unit cell volume [8], the same process in 10 nm sized particles of nano LTS induces stress and consequently irreversible changes in structure, which result in decrease of Na ion insertion capacity.

A role of rutile phase detected by HRTEM in nano LTS on its capacity decrease is not clear since rutile is not transformed to orthorhombic phase during Li insertion [17]. It could accommodate Li ion during Na insertion induced redistribution, but since no phase changes accompany this accommodation, it is probable that rutile influence on changes of morphology and capacity is less pronounced than that of anatase.

4. Conclusions

Cubic $Li_4Ti_5O_{12}$ is considered to be a promising candidate for sodium ion insertion mainly due to its high formal potential preventing Na-dendrite deposition. Na insertion into both commercial and laboratory-made nanocrystalline $Li_4Ti_5O_{12}$ samples was evaluated by cyclic voltammetry and chronopotentiometry.

Nanocrystalline $Li_4Ti_5O_{12}$ exhibited the best performance and charge capacity for Na storage. However considerable capacity drop was observed during cycling. This is obviously the consequence of irreversible structural changes induced by Na accommodation in the $Li_4Ti_5O_{12}$ lattice.

To identify these structural changes, nano LTS after several cycles of Na insertion/extraction was studied by Raman spectroscopy. Except for LTS peaks the spectrum exhibited features of orthorhombic $Li_{0,5}TiO_2$ phase, which is normally formed during Li insertion into anatase. There are no features of orthorhombic phase in the Raman spectrum of anatase after Na insertion. Detailed analysis of original nano LTS by Raman spectroscopy confirmed the presence of minor anatase impurities, transmission electron microscopy found minor impurities of both anatase and rutile. These additional minor phases were detectable neither by X-ray diffraction nor by cyclic voltammetry. Obviously Na insertion into nano LTS is accompanied by partial Li redistribution into minor anatase impurities. This process results in decrease of nano LTS ability to accommodate Na.

Acknowledgements

This work was supported by the Grant Agency of the Czech Republic (Contract No. 15-06511S) and by the project LM2015087 of the Ministry of Education, Youth, and Sports of the Czech Republic.

References

[1] V. Palomares, P. Serras, I. Villaluenga, K.B. Hueso, J. Carretero-González, T. Rojo, Na-ion batteries, recent advances and present challenges to become low cost energy storage systems, Energy & Environmental Science 5 (2012) 5884.

[2] J.P. Huang, D.D. Yuan, H.Z. Zhang, Y.L. Cao, G.R. Li, H.X. Yang, X.P. Gao, Electrochemical sodium storage of TiO_2(B) nanotubes for sodium ion batteries, RSC Advances 3 (2013) 12593.
[3] M. Zukalova, M. Kalbac, L. Kavan, I. Exnar, M. Graetzel, Pseudocapacitive lithium storage in TiO_2(B), Chemistry of Materials 17 (2005) 1248–1255.
[4] J. Lee, J.K. Lee, K.Y. Chung, H.-G. Jung, H. Kim, J. Mun, W. Choi, Electrochemical Investigations on TiO_2-B Nanowires as a Promising High Capacity Anode for Sodium-ion Batteries, Electrochimica Acta 200 (2016) 21–28.
[5] D. Prutsch, M. Wilkening, I. Hanzu, Long-Cycle-Life Na-Ion Anodes Based on Amorphous Titania Nanotubes–Interfaces and Diffusion, ACS Applied Materials & Interfaces 7 (2015) 25757–25769.
[6] M. Cabello, G.F. Ortiz, M.C. López, R. Alcántara, J.R. González, J.L. Tirado, R. Stoyanova, E. Zhecheva, Self-organized sodium titanate/titania nanoforest for the negative electrode of sodium-ion microbatteries, Journal of Alloys and Compounds 646 (2015) 816–826.
[7] K. Shen, M. Wagemaker, $Na_{(2+x)}Ti_6O_{13}$ as potential negative electrode material for Na-ion batteries, Inorganic chemistry 53 (2014) 8250–8256.
[8] M. Kitta, K. Kuratani, M. Tabuchi, N. Takeichi, T. Akita, T. Kiyobayashi, M. Kohyama, Irreversible structural change of a spinel $Li_4Ti_5O_{12}$ particle via Na insertion-extraction cycles of a sodium-ion battery, Electrochimica Acta 148 (2014) 175–179.
[9] Y. Sun, L. Zhao, H. Pan, X. Lu, L. Gu, Y.S. Hu, H. Li, M. Armand, Y. Ikuhara, L. Chen, X. Huang, Direct atomic-scale confirmation of three-phase storage mechanism in $Li_4Ti_5O_{12}$ anodes for room-temperature sodium-ion batteries, Nature communications 4 (2013) 1870.
[10] L. Kavan, M. Gratzel, Facile synthesis of nanocrystalline $Li_4Ti_5O_{12}$ (spinel) exhibiting fast Li insertion, Electrochem Solid St 5 (2002) A39–A42.
[11] L. Kavan, J. Prochazka, T.M. Spitler, M. Kalbac, M.T. Zukalova, T. Drezen, M. Gratzel, Li insertion into $Li_4Ti_5O_{12}$ (Spinel) – Charge capability vs. particle size in thin-film electrodes, Journal of the Electrochemical Society 150 (2003) A1000–A1007.
[12] M. Kalbac, M. Zukalova, L. Kavan, Phase-pure nanocrystalline $Li_4Ti_5O_{12}$ for a lithium-ion battery, Journal of Solid State Electrochemistry 8 (2003) 2–6.
[13] L. Kavan, M. Gratzel, J. Rathousky, A. Zukal, Nanocrystalline TiO_2 (anatase) electrodes: Surface morphology, adsorption, and electrochemical properties, Journal of the Electrochemical Society 143 (1996) 394–400.
[14] L. Kavan, A. Attia, F. Lenzmann, S.H. Elder, M. Gratzel, Lithium insertion into zirconia-stabilized mesoscopic TiO_2 (anatase), Journal of the Electrochemical Society 147 (2000) 2897–2902.
[15] L. Kavan, M. Kalbac, M. Zukalova, I. Exnar, V. Lorenzen, R. Nesper, M. Graetzel, Lithium storage in nanostructured TiO_2 made by hydrothermal growth, Chemistry of Materials 16 (2004) 477–485.
[16] B. Laskova, M. Zukalova, A. Zukal, M. Bousa, L. Kavan, Capacitive contribution to Li-storage in TiO_2 (B) and TiO_2 (anatase), Journal of Power Sources 246 (2014) 103–109.
[17] B. Pitna Laskova, L. Kavan, M. Zukalova, K. Mocek, O. Frank, In situ Raman spectroelectrochemistry as a useful tool for detection of TiO_2(anatase) impurities in TiO_2(B) and TiO_2(rutile), Monatshefte für Chemie – Chemical Monthly 147 (2016) 951–959.
[18] D.Z. Liu, W. Hayes, M. Kurmoo, M. Dalton, C. Chen, Raman scattering of the $Li_{1+x}Ti_{2-x}O_4$ superconducting system, Physica C: Superconductivity 235–240 (1994) 1203–1204.
[19] C.M. Julien, K. Zaghib, Electrochemistry and local structure of nano-sized $Li_{4/3}Me_{5/3}O_4$(MeMn, Ti) spinels, Electrochimica Acta 50 (2004) 411–416.
[20] L. Aldon, P. Kubiak, M. Womes, J.C. Jumas, J. Olivier-Fourcade, J.L. Tirado, J.I. Corredor, C. Pérez Vicente, Chemical and Electrochemical Li-Insertion into the $Li_4Ti_5O_{12}$Spinel, Chemistry of Materials 16 (2004) 5721–5725.
[21] M. Michalska, M. Krajewski, D. Ziolkowska, B. Hamankiewicz, M. Andrzejczuk, L. Lipinska, K.P. Korona, A. Czerwinski, Influence of milling time in solid-state synthesis on structure, morphology and electrochemical properties of $Li_4Ti_5O_{12}$of spinel structure, Powder Technology 266 (2014) 372–377.
[22] J. Mosa, M. Aparicio, K. Tadanaga, A. Hayashi, M. Tatsumisago, $Li_4Ti_5O_{12}$ thin-film electrodes by in-situ synthesis of lithium alkoxide for Li-ion microbatteries, Electrochimica Acta 149 (2014) 293–299.
[23] A.V. Knyazev, N.N. Smirnova, M. Mączka, S.S. Knyazeva, I.A. Letyanina, Thermodynamic and spectroscopic properties of spinel with the formula $Li_{4/3}Ti_{5/3}O_4$, Thermochimica Acta 559 (2013) 40–45.
[24] D.G. Kellerman, V.S. Gorshkov, E.V. Shalaeva, B.A. Tsaryev, E.G. Vovkotrub, Structure peculiarities of carbon-coated lithium titanate: Raman spectroscopy and electron microscopic study, Solid State Sciences 14 (2012) 72–79.
[25] P. Zheng, H. Wu, J. Guo, J. Dong, S. Jia, Z. Zhu, P–N co-doping induced structural recovery of TiO_2 for overall water splitting under visible light irradiation, Journal of Alloys and Compounds 615 (2014) 79–83.

Appendix 6

Barbora Laskova, Marketa Zukalova, Ladislav Kavan, Alison Chou, Paul Liska, Zhang Wei, Liu Bin, Pavel Kubat, Elham Ghadiri, Jacques E. Moser and Michael Grätzel. "Voltage enhancement in dye-sensitized solar cell using (001)-oriented anatase TiO_2 nanosheets." *J. Solid State Electrochem*, 2012, **16**, 2993-3001.

Voltage enhancement in dye-sensitized solar cell using (001)-oriented anatase TiO_2 nanosheets

Barbora Laskova, Marketa Zukalova, Ladislav Kavan, Alison Chou, Paul Liska, Zhang Wei, Liu Bin, Pavel Kubat, Elham Ghadiri, et al.

Journal of Solid State Electrochemistry
Current Research and Development in Science and Technology

ISSN 1432-8488
Volume 16
Number 9

J Solid State Electrochem (2012)
16:2993-3001
DOI 10.1007/s10008-012-1729-0

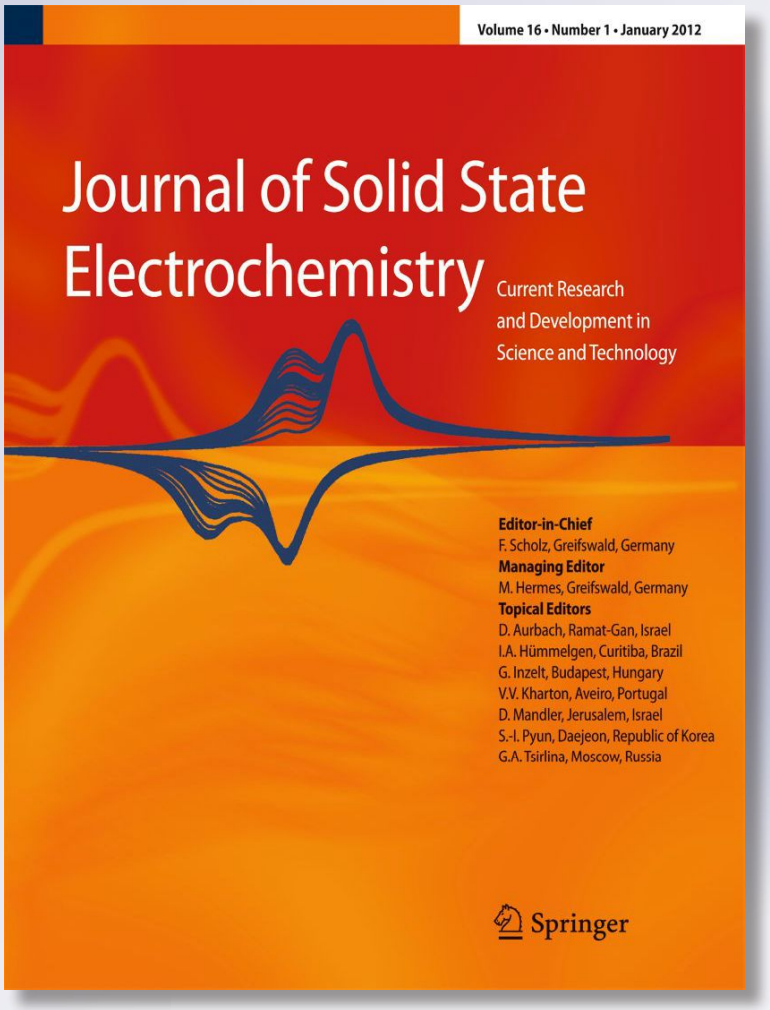

Springer

J Solid State Electrochem (2012) 16:2993–3001
DOI 10.1007/s10008-012-1729-0

ORIGINAL PAPER

Voltage enhancement in dye-sensitized solar cell using (001)-oriented anatase TiO_2 nanosheets

Barbora Laskova · Marketa Zukalova · Ladislav Kavan · Alison Chou · Paul Liska · Zhang Wei · Liu Bin · Pavel Kubat · Elham Ghadiri · Jacques E. Moser · Michael Grätzel

Received: 13 November 2011 / Revised: 13 March 2012 / Accepted: 15 March 2012 / Published online: 11 April 2012

Abstract A nanocrystalline TiO_2 (anatase) nanosheet exposing mainly the (001) crystal faces was tested as photoanode material in dye-sensitized solar cells. The nanosheets were prepared by hydrothermal growth in HF medium. Good-quality thin films were deposited on F-doped SnO_2 support from the TiO_2 suspension in ethanolic or aqueous media. The anatase (001) face adsorbs a smaller amount of the used dye sensitizer (C101) per unit area than the (101) face which was tested as a reference. The corresponding solar cell with sensitized (001)-nanosheet photoanode exhibits a larger open-circuit voltage than the reference cell with (101)-terminated anatase nanocrystals. The voltage enhancement is attributed to the negative shift of flatband potential for the (001) face. This conclusion rationalizes earlier works on similar systems, and it indicates that careful control of experimental conditions is needed to extract the effect of band energetic on the current/voltage characteristics of dye-sensitized solar cell.

Keywords Titanium dioxide · Anatase · Dye-sensitized solar cell

B. Laskova · M. Zukalova · L. Kavan (✉) · P. Kubat
J. Heyrovský Institute of Physical Chemistry, v.v.i.,
Academy of Sciences of the Czech Republic,
Dolejškova 3,
18223 Prague 8, Czech Republic
e-mail: kavan@jh-inst.cas.cz

B. Laskova · L. Kavan
Department of Inorganic Chemistry, Faculty of Science,
Charles University,
Hlavova 2030,
12843 Prague 2, Czech Republic

A. Chou
ARC Centre of Excellence for Functional Nanomaterials,
The University of Queensland,
Level 5, AIBN Building No. 75,
Corner College and Cooper Roads,
St Lucia, Queensland 4072, Australia

P. Liska · M. Grätzel
Laboratory of Photonics and Interfaces,
Institute of Chemical Sciences and Engineering,
Swiss Federal Institute of Technology,
1015 Lausanne, Switzerland

Z. Wei · L. Bin
Department of Chemical and Biomolecular Engineering,
National University of Singapore,
Singapore 117576, Singapore

E. Ghadiri · J. E. Moser
Photochemical Dynamics Group, Institute of Chemical Sciences and Engineering, Swiss Federal Institute of Technology,
1015 Lausanne, Switzerland

Introduction

Dye-sensitized solar cell (DSC), also called Grätzel cell, represents an attractive alternative of solid state photovoltaics due to high efficiency, low cost, and easy fabrication [1–4]. Optimization of TiO_2 photoanode for dye-sensitized solar cell has been a subject of numerous studies, and nanocrystalline anatase turned out to be the best material for this device [5]. The voltage enhancement is crucial for further improvement of DSCs [1, 3, 6–10]. Promising data were acquired recently by replacing the traditional electrolyte redox relay, I_3^-/I^- by other systems [3, 6–10], but little is known about the voltage enhancement via tuning of the photoanode material.

The (101) face is dominating in ordinary TiO_2 (anatase) materials (>94 % of the total surface area of crystals) [11]. The remaining face on the anatase crystal is (001) which is

consistent with the conclusion that a truncated bipyramid is the corresponding crystal morphology [12]. Only rarely, the rhombic-shaped crystals are found, exposing the (010) face [13]. Both (001) and (010) facets are called "high-energy" or "reactive" ones, and they show interesting activity in catalysis and photocatalysis [13–16].

Comparative studies of anatase (101) or (001) faces have been carried out on macroscopic single-crystal electrodes [17, 18], but the dye sensitization was attempted only on the (101) face of the single-crystal electrode [17]. The works on single-crystal electrodes confirmed that the (001) face had more negative flatband potential and was more active for Li insertion than the (101) face [18]. The conclusion about flatband potential shift was later reproduced on polycrystalline electrodes [19]. Also, the improved Li insertion was subsequently confirmed on polycrystalline (001)-oriented nanosheets [20]. They were prepared hydrothermally in HF medium according to Yang et al. [11], and the follow-up studies [14, 15, 21–23] report on materials enriched up to 90 % with the (001) face.

Recently, Wang et al. [24] studied the sensitization of such (001) nanosheets by CdS quantum dots, but no comparison with (101)-exposing crystals was presented. This was carried out earlier by Yu et al. [25], who observed improved conversion efficiency of a DSC employing hydrothermally grown nanosheets sensitized by the organometallic dye, N719 [chemical name: di-tetrabutylammonium cis-bis(isothiocyanato)bis(2,2′-bipyridyl-4,4′ dicarboxylato) ruthenium(II)], as the photoanode material. They attributed the improvement to three effects specific for the (001)-oriented nanosheets: (1) enhanced diffusion of the electrolyte, (2) more easy adsorption of the dye, and (3) fewer defects in the surface. However, there were no clear experimental data about electrolyte diffusion and defects, and the amount of adsorbed dye (N719) was actually smaller on nanosheets than that on nanoparticles [25] which seems to contradict the statement (2). Yang et al. [23] reported recently on hierarchical spheres with over 90 % (001) faces which were more active than the Degussa P25 titania material in dye-sensitized solar cells, and the effect was ascribed to (1) stronger ability to dissociatively "absorb" (COOH) groups, (2) higher surface area for dye loading, (3) light scattering, and (4) smaller electron losses at grain interfaces [23]. However, these conclusions were not supported by direct experimental data. Zhang et al. [26] tested the (001)-exposed microspheres in a bilayer photoanode with Degussa P25 underlayer, and concluded that the beneficial effect consists in enhanced light scattering on the mirror-like (001) facets.

To address these divergences, we report here on a comparative study showing that a significant effect favoring the (001) nanosheets is the enhanced open-circuit voltage of the solar cell. This result is consistent with the negative shift of flatband potential of the (001) face. To the best of our knowledge, this conclusion is presented here for the first time; hence, it upgrades earlier works dealing with these problems [23, 25, 26].

Experimental section

Materials

Anatase TiO_2 nanosheets were prepared as follows: 10 mL of titanium (IV) butoxide was mixed with 0.8–1.2 mL of hydrofluoric acid (concentration, ≈50 %). The mixture was sealed in a Teflon cell encased in a stainless steel autoclave and heated at 180–200 °C for 24 h. A sample was then collected, washed with copious amounts of Milli-Q water and finally dried at 100 °C. The reference material was prepared in the same way, but in the absence of HF which was replaced by the same amount of water. X-ray diffraction patterns (data not shown) confirmed that the reference material was phase-pure anatase. For comparison, a second reference material (coded C240) [27] was also used. It is nanocrystalline anatase, S_{BET}=89 m^2/g, prepared by hydrolysis of titanium tetra(*iso*propoxide) and hydrothermal recrystallization at 240 °C in the absence of HF [28]. The crystal morphology of C240 is characterized by particles ca. 10–20 nm in size exposing mainly the (101) facets, and it is frequently used for DSC [29]. The photoelectrochemical behavior of both reference materials was very similar.

Electrodes from all parent powder materials (see above) were fabricated using either aqueous paste (A films) or simply ethanolic suspension (E films). The aqueous paste was prepared as follows: 0.3 g of the powder was mixed under slow addition of 4×0.15 mL of 10 % aqueous solution of acetylacetone, 0.3 mL of 4 % aqueous solution of hydroxypropylcellulose (MW 100,000), and 0.3 mL of 10 % aqueous solution of Triton-X100. The obtained slurry was deposited on F-doped SnO_2 (FTO) glass (TEC 15 from Libbey-Owens-Ford, 15Ω/sq) with Kapton foil tape defining the TiO_2 film edges. The film was then calcined for 30 min in air at 450 °C. For the preparation of E film electrodes, the powder samples were sonicated in ethanol. The obtained slurry was deposited by doctor blading, and a uniform semitransparent film was obtained after drying at room temperature and calcination in air at 450 °C. Typical film thickness was 2–4 μm (Alpha-step profilometer, Tencor Instruments) for both A/E films.

The C101 dye [NaRu(4,4′-bis(5-hexylthiophene-2-yl)-2,2′-bipyridine)(4-carboxylic acid-4′-carboxylate-2,2′-bipyridine)$(NCS)_2$] with chenodeoxycholic acid (cheno) as a coadsorbent was used for sensitization (see [30] for details). Immediately after calcination, the still warm electrode (ca. 50 °C) was dipped in a solution containing

300 μmol/L of C101 dye and 300 μmol/L cheno in a mixed solvent of acetonitrile+t-butanol solution (1:1, *v*/*v*). The electrodes were soaked at room temperature in the solution overnight to secure complete attachment of the sensitizer dye to the electrode surface. To avoid irregularities in dye attachment [31], the sensitization time and temperature were identical for all the tested electrodes. The DSC was assembled with platinized F-doped tin oxide (FTO) counter electrode [32, 33] using a Surlyn tape (25 μm in thickness) as a seal and spacer. The electrolyte solution was 0.6 M *N*-methyl-*N*-butyl imidazolium iodide, 40 mM I_2, 0.075 M lithium iodide, 0.26 M *tert*-butylpyridine, and 0.05 M guanidine thiocyanate in acetonitrile/valeronitrile (85/15 %, *v*/*v*). The cell active area for illumination was 0.22 cm^2, defined by a mask.

Methods

The X-ray diffraction (XRD) was investigated on powder samples by XRD-6000, Shimadzu, Japan, using Ni-filtered CuKα radiation (λ=0.15418 nm). The transmission electron microscopy (TEM) images were measured on a JEOL JEM-2010F microscope. The BET surface areas of the prepared powder materials were determined from nitrogen adsorption isotherms at 77 K using the Micromeritics ASAP 2020 instrument. The surface areas of thin films were determined from Kr-adsorption isotherms, which were measured directly on the sintered films following the methodology described in [34]. The surface concentration of the C101 dye on TiO_2 was measured spectrophotometrically as follows: The sensitized electrode was dipped in 0.1 M tetrabutylammonium hydroxide in dimethylformamide and stirred until complete desorption into the liquid took place. The solution was analyzed on the PerkinElmer Lambda 1050 spectrometer using the extinction coefficient $\varepsilon_{550}=17.5\cdot10^3\ M^{-1}\,cm^{-1}$ [30]. The dye surface coverage (Γ_{dye}) was determined by normalizing the found dye concentration to the film's physical surface area from Kr-adsorption isotherm. Scanning electron microscopy (SEM) and energy-dispersive X-ray analysis (EDX) were carried out with the Hitachi FE SEM S-4800 microscope equipped with the Noran EDX system. Electrochemical measurements were carried out in a one-compartment cell using an Autolab Pgstat-30 (Ecochemie) controlled by GPES-4 software. For photoelectrochemical tests, the light source was a 450-W xenon light source (Osram XBO 450, Germany) with a filter (Schott 113). The light power was regulated to the AM 1.5G solar standard by using a reference Si photodiode equipped with a color-matched filter (KG-3, Schott) to reduce the mismatch in the region of 350–750 nm between the simulated light and AM 1.5G to less than 4 %. The differing intensities were regulated with a neutral wire mesh attenuator. The applied potential and cell current were measured using a Keithley model 2400 digital source meter. Optical determination of the flatband potential was made by a spectroelectrochemical method described in [35–37]. The measurement was carried out in 0.2 M $NaClO_4$ (pH adjusted by $HClO_4$ or NaOH) using UV–vis–NIR spectrometer PerkinElmer Lambda 1050 interfaced to a potentiostat. Measurements were performed in transmission mode at gradually decreasing potentials from 0 V to −1.2 or −1.4 V. Potential was set, and after 1.5 min at the given potential, the spectrum was measured. For data processing, the measured spectra were normalized by subtracting the spectrum measured at 0 V. Nanosecond flash photolysis was applied to C101 dye-sensitized transparent TiO_2 layers covered by a film of pure methoxypropionitrile and a thin cover glass. Pulsed excitation (λ=530 nm, 5-ns FWHM pulse duration, 20-Hz repetition rate) was provided by an optical parametric oscillator (GWU OPO-355), pumped by a frequency-tripled, Q-switched Nd:YAG laser (Continuum, Powerlite 7030). The laser beam output was expanded by plano-concave lens to irradiate a large cross section of the sample, whose surface was kept at a 30° angle to the excitation beam. The probe light, produced by a Xe arc lamp, passed through the first monochromator, various optics, and the sample. Transmitted light was focused on the entrance slit of the second monochromator and detected by a fast photomultiplier tube. Data waves were recorded on a DSA 602A digital signal analyzer (Tektronix). Satisfactory signal-to-noise ratios were typically obtained by averaging over 3,000 laser shots.

Results and discussion

Figure 1a shows a typical X-ray diffraction pattern of TiO_2 nanosheets (grown in HF medium), indicating the formation of pure anatase TiO_2 (JCPDS no. 21–1272). The diffractograms of (001) nanosheets are similar to those of (101)-nanoparticles, which is in accord with earlier literature [11, 14, 15, 21, 22]. As XRD is obviously not very sensitive to distinguish the (001) or (101) oriented anatase crystals, the morphology of our TiO_2 anatase nanosheets was characterized by transmission electron microscopy. A typical nanosheet dimension was $40\cdot30\cdot7\ nm^3$ (Fig. 1b). Figure 1c shows a high-magnification TEM image of two selected individual TiO_2 nanosheets (ca. $30\cdot20\cdot7\ nm^3$ in size). The lattice spacing parallel to the top and bottom facets was determined to be ~0.235 nm, corresponding to the (001) planes of anatase TiO_2. Figure 1d shows the corresponding selected-area electron diffraction (SAED) pattern (indexed as the (001) zone axis diffraction). It further indicates that the top and bottom facets of the nanosheets are the (001) planes. The anatase nanosheets exhibited a specific surface area from nitrogen adsorption measurement, S_{BET} between 85 and 120 m^2/g depending on the sample batch. Higher values were

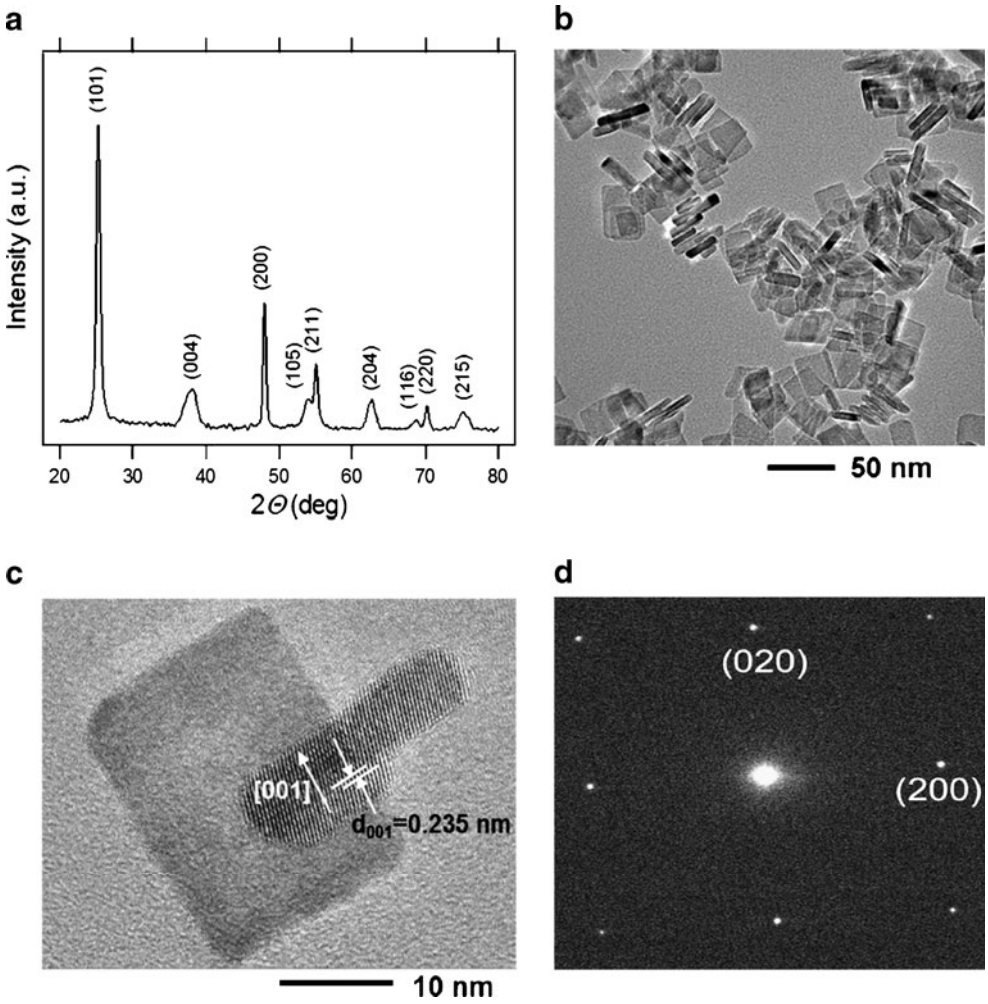

Fig. 1 Structural characteristics of (001) nanosheets. **a** XRD pattern. **b** Low-magnification TEM image. **c** High-magnification TEM image. **d** Typical SAED pattern of an individual TiO_2 nanosheet

observed in products grown from mixtures containing less HF and autoclaved at lower temperatures (see "Experimental section"). The typical nanosheet dimension of 40·30·7 nm^3 (cf. Fig. 1b) translates into the calculated S_{BET} of 103 m^2/g, which matches reasonably well the experimental values from adsorption isotherms. The particles grown in HF-free medium had S_{BET}=150 m^2/g and exhibited the usual bipyramidal crystal shape with (101) facets. This morphology resembles that of C240 particles optimized earlier for DSC applications [29].

SEM images of our nanosheet-based electrodes are shown in Fig. 2. Both variants of TiO_2 film deposition (A films, E films; see "Experimental section") exhibited a similar morphology of unorganized nanoplatelets which were reasonably uniform and non-agglomerated. This is beneficial for achieving good optical and mechanical quality of the films. It should be noted that even the E films were optically semitransparent with good adhesion to the FTO support in spite of the very simple deposition procedure used and the fact that particles were not stabilized against agglomeration by any other additives as in the case of A films (see "Experimental section"). The as-received nanosheet material contained 8 wt% of F, as determined by EDX analysis, but the heat treatment during electrode fabrication (450 °C, 30 min; see "Experimental section) caused the F content to drop practically to zero for both the A and E films.

The actual surface area of electrodes (determined from the Kr-adsorption isotherm of the thin-film samples) was normalized to the projected geometric area, which provided the roughness factor. The found values of roughness factor were from 100 to 600 for various film thicknesses, but without significant distinction between the A and E films. More importantly, the surface concentration of the dye (Γ_{dye}) was, for both film types (A, E), significantly smaller on the (001) films compared to that on (101) films (Table 1). The found Γ_{dye} for (101) films is comparable to the values reported earlier for various Ru-bipyridine sensitizers adsorbed on titania (from 0.56 to 1.16 molecules/nm^2; see [38] for the data overview). Recently, Sauvage et al. [31] studied the C101 dye adsorption on a TiO_2 film which was, obviously, rich in the (101)-terminated anatase particles. They found an almost perfect dye monolayer (assuming Γ_{dye}=0.57 molecules/nm^2) only for the films sensitized at low temperature (4 °C), but the dye coverage exceeded the

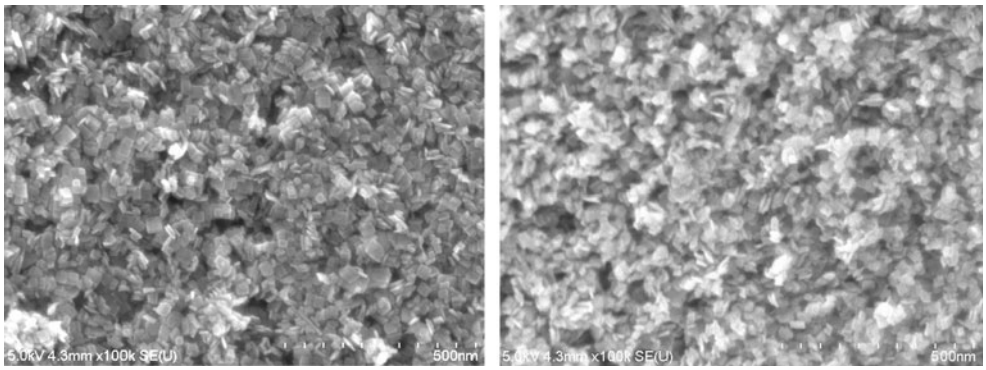

Fig. 2 Scanning electron microscopy images of the FTO-deposited film from (001)-oriented nanosheets. *Left*: A film, *right*: E film

monolayer saturation limit for the films sensitized at room or higher temperatures. In accord with this report, both our (101) films adsorb more C101 dye than expected for a monolayer (Table 1). However, our Γ_{dye} values for the (001) films are below this limit. The relatively smaller dye loading on the (001) face was also reported for the N719 dye [25], but the reason for smaller adsorption capacity of this face is unclear. The anchoring of N719 and N3 dyes [N3 is *cis*-*bis*(isothiocyanato) *bis*(2,2′-bipyridyl-4,4′-dicarboxylato ruthenium(II)] on the (101) face was investigated carefully, including quantum chemical simulations [38, 39], but there is no corresponding study of the (001) face nor that of other dyes like C101.

The trend that smaller values of Γ_{dye} are observed for the (001) films qualitatively agrees with the conclusion of Yu at al. [25] who reported that the surface concentration of N719 dye was 143 nmol/cm^2 for the (001) nanosheets or 214 nmol/cm^2 for the reference (101) nanoparticles, respectively. However, the values reported by Yu et al. [25] do not seem to be normalized to the physical (BET) area of the TiO_2 film as in our case. (Note that the recalculated Γ_{dye} for the physical surface area would be unrealistically high in the cited work [25], ca. a thousand molecules per square nanometer). Also, we should note that our data in Table 1 do not support the assumption of Yang et al. [23] that the (001) face has better ability to adsorb the N719 dye.

Figure 3 shows the current–voltage characteristics of a solar cell employing the dye-sensitized A films (Fig. 3a) and E films (Fig. 3b). In both cases, data are plotted for (001)-oriented nanosheets (full curves) and reference (101) particles (dashed curves). For the reference (101) particles, we report on the materials grown from Ti(IV) butoxide in HF-free medium (S_{BET}=150 m^2/g), but the plots for our second (101) reference (C240, S_{BET}=89 m^2/g) were quite similar (data not shown). Detailed results about our solar cells are collected in Table 1. It is obvious that the (001)-oriented nanosheet films exhibit smaller short-circuit photocurrents (I_{sc}), particularly at 100 % sun illumination, when the light harvesting is less efficient, and also, the Γ_{dye} concentrations are lower (Table 1). Hence, we attribute the smaller I_{sc} to smaller dye loading on the (001) nanosheets. At 10 % sun, the differences in photocurrents are less pronounced or even negligible (A film, Fig. 3a). The (101) particles in A film further show superlinear response to light intensity which might be caused by some dye aggregation. This effect, albeit less pronounced, is also expressed for the remaining films in Table 1. It is further illustrated by higher η values for higher light intensity. Usually, we observe opposite trends [30], but there are also examples when η and light intensity do not scale monotonically for dyes of this type [40]. Furthermore, there is no proportionality between the efficiency, η, and Γ_{dye} (Table 1). This finding is supported by Sauvage et al. [31] who reported on decreasing efficiency for the C101-sensitized films, if the Γ_{dye} was larger than the monolayer coverage. They concluded that subtle structural characteristics at the C101/TiO_2 interface influence the

Table 1 Characteristics of dye-sensitized solar cells with various TiO_2 films

Film type	Γ_{dye} [molecules/nm^2]	10 % sun				100 % sun			
		I_{sc} [mA/cm^2]	U_{oc} [mV]	FF	η [%]	I_{sc} [mA/cm^2]	U_{oc} [mV]	FF	η [%]
A-(001)	0.4	0.86	620	0.74	4.2	8.78	708	0.69	4.3
A-(101)	0.7	0.89	566	0.73	3.8	10.4	660	0.69	4.7
E-(001)	0.5	0.51	625	0.74	2.5	5.34	725	0.72	2.8
E-(101)	0.8	0.65	583	0.72	2.8	6.36	681	0.71	3.1

Γ_{dye} surface concentration of the C101 dye in molecules per square nanometer, I_{sc} short-circuit photocurrent, U_{oc} open-circuit voltage, *FF* fill factor, η solar conversion efficiency

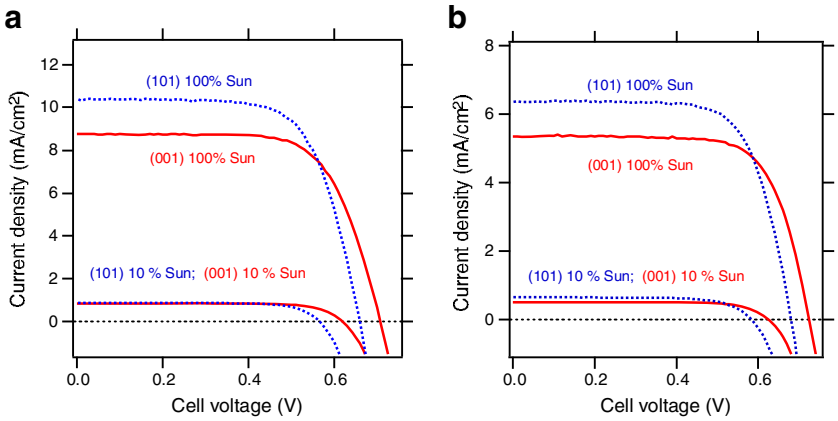

Fig. 3 Current–voltage characteristics of dye-sensitized solar cells employing C101-sensitized TiO_2 photoanode either from (001)-oriented nanosheets (*solid red lines*) or reference (101) nanoparticles (*dashed blue lines*). **a** A films, **b** E films

electron transfer dynamics and light harvesting of the assembly [31].

The actually measured photocurrent is further dependent on the TiO_2 film thickness. This is difficult to control accurately in various film-deposition techniques; hence, the matching of photocurrents in Fig. 3a (10 % sun) is casual only. From this point of view, we should consider with care the conclusion by Yu at al. [25] who observed a larger photocurrent for the (001) nanosheets, compared to that for (101) nanoparticles and reference commercial titania (P25, Degussa). They reported a film thickness of "about 10 μm," but the surface concentration of the used dye (N719) was actually smaller by a factor of ca. 1.5 on the (001) nanosheets compared to that on their reference (101) nanoparticles [25]. The relatively smaller dye loading for (001) nanosheets compared to that on (101) particles was also reproduced by us (see Γ_{dye} values in Table 1). At full sun illumination, our solar conversion efficiencies η are slightly better for the (101)-terminated nanocrystals. This is due to the dominating contribution of enhanced photocurrent for this face. Our conclusion is in conflict with Yu et al. [25] who reported just the opposite trend in photocurrents and η values.

Figure 3 and Table 1 demonstrate that the most pronounced effect distinguishing (001) nanosheets from the ordinary (101) nanoparticles is the open-circuit voltage (U_{oc}) enhancement of the former. The found differences in open-circuit voltage between nanosheets and nanoparticles (ΔU_{oc}) were 54 or 48 mV (for A films at 10 or 100 % sun, respectively) and 42 or 44 mV for E films at the corresponding conditions and for the actual experiments demonstrated in Table 1. It should be noted that these numbers (and the data in Fig. 3 and Table 1) represent only a single set of measurements; hence, experimental errors and the likely sample-to-sample variations could be unnoticed. To avoid such mistakes, we have carried out a statistical evaluation of data using an array of parallel tests on various TiO_2 films with a different preparation history. This analysis showed statistically insignificant differences between A and E films. The averaged values for both film types (A, E) were as follows:

$$\Delta U_{oc} = (47 \pm 3)\ \text{mV at 10 \% sun illumination}$$
$$\Delta U_{oc} = (45 \pm 2)\ \text{mV at 100 \% sun illumination}$$

Obviously, even the dependence on the light intensity is not very pronounced too. This points at the hypothesis, that ΔU_{oc} reflects a fundamental physical effect (albeit small) but not a variable introduced by experimental conditions, such as film thickness, preparation history, dye loading, light intensity, etc. More specifically, one of the reasons for positive values of ΔU_{oc} can be the corresponding shift of flatband potential of (001) faces/(101) faces.

Similarly enhanced voltage (ΔU_{oc}=20 mV) was found for 001-terminated anatase in hierarchical spheres, referred to the value for P25 particles [23]. However, the enhancement was not discussed in [23] and we should also note that P25 is hardly the optimum reference material. It is, actually, a mixture of anatase and rutile, while both phases exhibit a significantly different electronic structure: e.g., the flatband potential of rutile is by 0.2 V more positive than the value for anatase [17].

In contrast to these data, Yu et al. [25] reported on negligible differences in U_{oc} for their (001) nanosheets, (101) nanoparticles, and the P25 film sensitized by N719. To address this paradox, we should note that Yu et al. [25] found a considerably smaller U_{oc} (ca. 580 to 590 mV at 100 % sun) for their DSCs compared to our values (Table 1). Smaller U_{oc} values may stem from a voltage drop caused by enhanced recombination of photoinjected electrons in the titania conduction band with the electrolyte [4, 41], and this effect can mask any other mechanism of fine tuning of U_{oc}, e.g., by crystal face orientation.

Our combination of cheno-coadsorbent with high-extinction dye (C101) provides, obviously, a more-defined interface for exploring small U_{oc} shifts undisturbed by such parasitic effects. Cheno improves the dye attachment by assembling the geometry of the surface complex, prevents

agglomeration of dye molecules, and decreases the recombination losses with the electrolyte solution [30, 42, 43]. Furthermore, the back electron transfer can be hindered by a compact titania underlayer on top of the FTO support [4]. This strategy is unsuitable for our study, aiming at the distinction of (001)- and (101)-terminated nanocrystals, but we should note that the optimization of the morphology of TiO_2 photoanode may further enhance U_{oc} for a DSC device quite similar to ours [30]. Hence, the elimination of all the other factors influencing ΔU_{oc} is essential, if subtle effects caused by band energetic are to be unraveled.

To test our hypothesis about different band energetic, Fig. 4 compares spectroelectrochemical data for thin-film electrodes made from (001)- and (101)-terminated nanocrystals. This technique was developed for determination of the flatband potential of transparent semiconductors, and it is particularly useful for nanocrystalline electrodes where the standard method based on electrochemical impedance (Mott–Schottky plots) is complicated by various factors [35–37]. The flatband potential of anatase, E_{fb} (in volts) is known to exhibit Nernstian dependence on pH:

$$E_{fb} = E_0 - 0.0591\mathrm{pH} \quad (1)$$

where the constant E_0 was reported to be −0.4 V for the (101) face assuming a saturated calomel electrode (SCE) as the reference electrode [17, 35, 36]. The negative shift of absorbance/potential profiles for the (001)-oriented film is apparent from Fig. 4, although the absorbance onset potential is not that clearly different. This might be due to surface states which contribute differently in (001) or (101) films. Based on optical spectra and X-ray photoelectron spectroscopy (XPS), Pan et al. [16] concluded that the conduction band edge of (001) face is upshifted (in electrochemical scale) by 0.04 V. This contradicts our conclusion, as well as earlier spectroelectrochemical reports on single-crystal [18] and polycrystalline [19] electrodes. (One of the reasons for this discrepancy might be that the reported upshift is within experimental error of the determination of the valence band edge by XPS [16].)

Our data are in qualitative accord with the earlier conclusion by Kawakita et al. [19] based on Mott–Schottky plots for (001)- vs. (101)-oriented nanocrystals similar to ours. These authors reported on negative shift of E_{fb} for their (001)-oriented nanocrystals; the E_{fb} values were from ca. −0.4 to 0 V vs. SCE for various samples at pH 6 (phosphate buffer). This is more positive than the value of $E_{fb} \approx -0.75$ V predicted by Eq. (1), but the difference was not commented on in [19]. As discussed above, accurate impedance data are available for single-crystal electrodes only; in this case, the E_{fb} values for (001) face were negatively shifted by 0.06 V compared to that of (101) face [18]. This negative shift of E_{fb} is not far from the observed enhancement of open-circuit voltage, ΔU_{oc} of ca. 0.04 V found in this study (vide ultra). However, there might be also other effects at play, such as different geometry of the dye/titania surface complex [44].

To get further insight into the specific behavior of (001) nanosheets referenced to that of (101) nanoparticles, we employed transient absorption spectroscopy. Nanosecond flash excitation was applied to C101-sensitized TiO_2 film contacting pure methoxypropionitrile solvent. Monitoring the transient absorbance signal at a wavelength λ=650 nm allowed to follow the time course of the dye cation S^+ produced upon ultrafast electron injection from the photo-excited sensitizer, S*, into the conduction band of TiO_2 (Eq. 2). In the absence of electrolyte (redox mediator), the

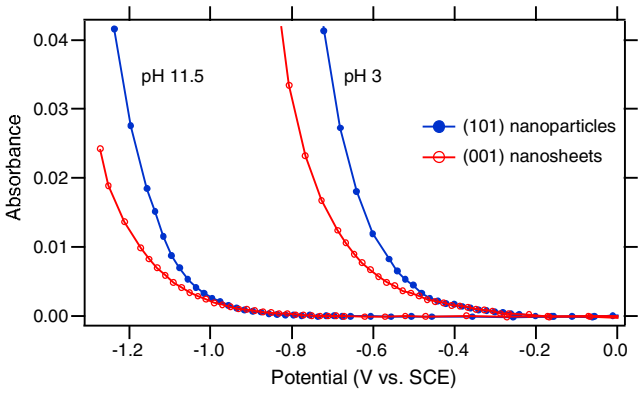

Fig. 4 Optical absorbance of TiO_2 films from (001)- or (101)-oriented nanosheets plotted by *open red points* or *full blue points*, respectively. The absorbance was measured at 640 nm and normalized to the mass of the TiO_2 film. It is plotted as a function of the applied electrochemical potential in 0.2 M $NaClO_4$ at two different pH values. The *lines* are guides to the eye

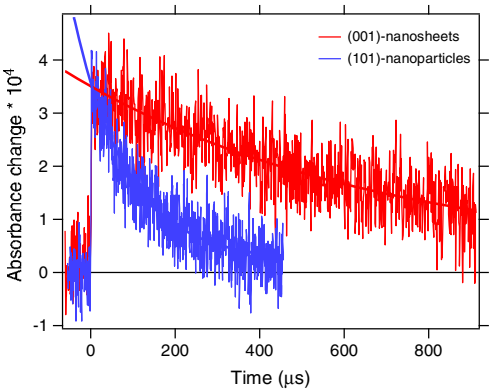

Fig. 5 Temporal behavior of the transient absorbance measured at λ=650 nm for a C101 dye-sensitized anatase (001)-nanosheet film, covered by pure methoxypropionitrile solvent, upon ns-pulsed laser excitation (*red trace*). A typical transient absorbance decay curve obtained in identical conditions with (101) nanoparticles is shown for comparison (*blue trace*). Amplitudes of both signals were normalized at time zero for a better visual comparison. The first-order kinetic fits are indicated on top of each experimental curve

decay of the S^+ signal was due to the back electron transfer reaction (Eq. 3).

$$S|TiO_2 + h\nu \rightarrow S^*|TiO_2 \rightarrow S^+ + e^-{}_{cb}(TiO_2) \quad (2)$$

$$S^+ + e^-{}_{cb}(TiO_2) \rightarrow S|TiO_2 \quad (3)$$

The excitation pulse fluence was progressively decreased by neutral density filters until the signal displayed a single exponential decay (Fig. 5). The used fluence of 35 μJ/cm^2 was then believed to relate to the injection of at most one electron per TiO_2 nanoparticle or nanosheet. The transport of charges between individual nanoparticles or nanosheets is negligible within the sub-millisecond time frame of the back electron transfer process.

The corresponding rate constant, k_b (Eq. 3), can be obtained from first-order kinetic fit of the absorbance change, ΔA:

$$\Delta A = C + B \cdot \exp(-k_b \cdot t) \quad (4)$$

where t is time and C and B are constants. The fitted values of k_b are: $1.2 \cdot 10^3$ s^{-1} for the (001) nanosheets and $7.7 \cdot 10^3$ s^{-1} for the (101) nanoparticles, respectively. Hence, the back electron transfer is by a factor of 6 slower for the (001) nanosheets compared to the same process on (101) nanoparticles. The difference in the back electron transfer kinetics observed for both samples could be rationalized by a change in the dye-anchoring geometry. Assuming a damping coefficient β=1.2 Å^{-1} for through-space electron tunneling (Eq. 5), retardation of the charge recombination reaction by a factor of 6 corresponds to the increase of the electron transfer distance existing between the Ru(III) center of the oxidized dye and the closest Ti(IV) site on the surface of the oxide by Δr=1.5 Å:

$$k_b = k_b^0 \cdot \exp(-\beta \Delta r) \quad (5)$$

C101 has only two carboxylic anchoring groups available on a single bpy ligand. The distance between the Ru ion and the TiO_2 thus depends strongly upon the tilt angle of the pyridyl rings on the surface. Because the dicarboxylated bpy ligand (bi-isonicotinic acid) tends to distort upon anchoring on the TiO_2 surface, different geometries are expected on the (101) and (001) surfaces [45]. The distance between the Ru center of the dye and the Ti^{4+} ion directly linked to one of the oxygen atoms of the carboxylic anchor is ≈10 Å when the bpy adopts a flat structure. A change of the tilt angle of the pyridyl rings related to the surface normal of ca. 15° on the (001) facet to ca. 35° on the (101) facet would yield a decrease of the distance between the Ru center in the dye to the surface:

$$\Delta r = 10 \cdot \cos 15 - 10 \cdot \cos 35 \approx 1.5\,\text{Å} \quad (6)$$

which is the Δr value calculated from our experimental data (Eq. 5).

In DSCs, the back electron transfer process competes kinetically with the regeneration of the dye by the donor species of the electrolyte. As the latter reaction should not depend upon the crystalline face on which the dye is adsorbed, the retardation of the back electron transfer can only improve the charge separation yield. The difference in back electron transfer rate (k_b) hardly influences the open-circuit voltage of the cell. The U_{OC} certainly depends on the injected electrons' quasi-Fermi level [2, 4]. However, the electrons' lifetime is controlled by the competition between their transport in the TiO_2 network and their recombination with the oxidized mediator (I_3^-). The recombination between conduction-band electrons and the dye cations, S^+, is generally sufficiently intercepted by the reduction of S^+ by I^- and is not expected to influence the potential of DSC.

Conclusion

Nanocrystalline TiO_2 (anatase) in two different crystal morphologies exposing mainly the (001) or (101) crystal faces was employed as a photoanode material in dye-sensitized solar cells. The (001) face adsorbs a smaller amount of the used dye sensitizer (C101) but provides a larger open-circuit voltage of the solar cell. The negative shift of flatband potential is suggested to be responsible for the observed enhancement of U_{oc}. This conclusion helps to rationalize contradictory data in the earlier literature. Furthermore, it indicates that careful control of experimental conditions is needed to extract the effect of band energetic on the current/voltage characteristics of the dye-sensitized solar cell.

Acknowledgments This work was supported by the Academy of Sciences of the Czech Republic (contracts IAA 400400804 and KAN 200100801), Grant Agency of the Czech Republic (contract no. P108/12/0814), and the EC 7th FP project SANS (contract no. NMP-246124). B.L. thanks the National Research Foundation of Singapore (R279-000-276-272) for financial support. M.G. is very grateful to the European Research Council (ERC) for supporting his research under the ERC-2009-AdG grant no 247404 MESOLIGHT.

References

1. Grätzel M (2001) Nature 414:338–344
2. Hagfeldt A, Boschloo G, Sun L, Kloo L, Pettersson H (2010) Chem Rev 110:6595–6663
3. Yella A, Lee HW, Tsao HN, Yi C, Chandiran AK, Nazeeruddin MK, Diau EWG, Yeh CY, Zakeeruddin SM, Grätzel M (2011) Science 334:629–634
4. Kalyanasundaram K (2010) Dye sensitized solar cells. EPFL Press & CRC Press, Lausanne

5. Kavan L (2012) Chem Rec 12:131–142
6. Wang M, Chamberland N, Breau L, Moser J, Humphry-Baker R, Marsan B, Zakeeruddin SM, Grätzel M (2010) Nature Chem 2:385–389
7. Daeneke T, Kwon TH, Holmes AB, Duffy NW, Bach U, Spiccia L (2011) Nature Chem 3:211–215
8. Feldt SM, Gibson EA, Gabrielsson E, Sun L, Boschloo G, Hagfeldt A (2010) J Am Chem Soc 132:16714–16724
9. Kavan L, Yum JH, Grätzel M (2011) Nano Lett 11:5501–5506
10. Kavan L, Yum JH, Nazeeruddin MK, Grätzel M (2011) ACS Nano 5:9171–9178
11. Yang HG, Sun CH, Qiao SZ, Zou J, Liu G, Smith SC, Cheng HM, Lu GQ (2008) Nature 453:638–642
12. Olson CL, Nelson J, Islam MS (2006) J Phys Chem B 110:9995–10001
13. Wu B, Guo C, Zheng N, Xie Z, Stucky GD (2008) J Am Chem Soc 130:17563–17567
14. Han X, Kuang Q, Jin M, Xie Z, Zheng L (2009) J Am Chem Soc 131:3152–3153
15. Zhang D, Li G, Yang X, Yu JC (2009) Chem Commun 2009:4381–4383
16. Pan J, Liu G, Lu GQ, Cheng HM (2011) Angew Chem Int Ed 50:2133–2137
17. Kavan L, Grätzel M, Gilbert SE, Klemenz C, Scheel HJ (1996) J Am Chem Soc 118:6716–6723
18. Hengerer R, Kavan L, Krtil P, Grätzel M (2000) J Electrochem Soc 147:1467–1472
19. Kawakita M, Kawakita J, Sakka Y, Shinohara T (2010) J Electrochem Soc 157:H65–H68
20. Bousa M, Laskova B, Zukalova M, Prochazka J, Chou A, Kavan L (2010) J Electrochem Soc 157:A1108–A1112
21. Chen JS, Lou XW (2009) Electrochem Commun 11:2332–2335
22. Yang HG, Liu G, Qiao SZ, Sun CH, Jin YG, Smith SC, Zou J, Cheng HM, Lu GQ (2009) J Am Chem Soc 131:4078–4083
23. Yang W, Li J, Wang Y, Zhu F, Shi W, Wan F, Xu D (2011) Chem Commun 47:1809–1811
24. Wang X, Liu G, Wang L, Pan J, Lu GQ, Cheng HM (2011) J Mater Chem 21:869–873
25. Yu J, Fan J, Lv K (2010) Nanoscale 2:2144–2149
26. Zhang H, Han Y, Liu X, Yu H, Zhang S, Yao X, Zhao Z (2010) Chem Commun 46:8395–8397
27. Kavan L, Grätzel M, Rathousky J, Zukal A (1996) J Electrochem Soc 143:394–400
28. Barbe C, Arendse F, Comte P, Jirousek M, Lenzmann F, Shklover V, Grätzel M (1997) J Amer Ceram Soc 80:3157–3171
29. Grätzel M (2006) Prog Photovolt Res Appl 14:429–442
30. Gao F, Wang Y, Shi D, Zhang J, Wang M, Jing X, Humphry-Baker R, Wang P, Zakeeruddin SM, Grätzel M (2008) J Am Chem Soc 130:10720–10728
31. Sauvage F, Decoppet JD, Zhang M, Zakeeruddin SM, Comte P, Nazeeruddin MK, Wang P, Grätzel M (2011) J Am Chem Soc 133:9304–9309
32. Papageorgiou N, Maier WE, Grätzel M (1997) J Electrochem Soc 144:876–884
33. Murakami TN, Ito S, Wang Q, Nazeeruddin MK, Bessho T, Cesar I, Liska P, Humphry-Baker R, Comte P, Pechy P, Grätzel M (2006) J Electrochem Soc 153:A2255–A2261
34. Zukalova M, Zukal A, Kavan L, Nazeeruddin MK, Liska P, Grätzel M (2005) Nano Lett 5:1789–1792
35. Rothenberger G, Fitzmaurice D, Grätzel M (1992) J Phys Chem 96:5983–5986
36. Redmond G, Fitzmaurice D (1993) J Phys Chem 97:1426–1430
37. Kavan L, Stoto T, Grätzel M, Fitzmaurice D, Shklover V (1993) J Phys Chem 97:9493–9498
38. Zukalova M, Prochazka J, Zukal A, Yum JH, Kavan L (2008) Inorg Chim Acta 361:656–662
39. Fantacci S, De Angelis F (2011) Coord Chem Rev 2704–2726
40. Yu Q, Wang Y, Yi Z, Zu N, Zhang J, Zhang M, Wang P (2010) ACS Nano 4:6032–6038
41. Nazeeruddin MK, Kay A, Rodicio I, Humphry-Baker R, Mueller E, Liska P, Vlachopolous N, Grätzel M (1993) J Am Chem Soc 115:6382–6390
42. Morandeira A, Durante IL, O'Regan B, Martinez-Diaz MV, Fornelli A, Palomares E, Torres T, Durrant JR (2010) J Mater Chem 19:5016–5026
43. Yum JH, Jang SR, Humphry-Baker R, Grätzel M, Cid JJ, Torres T, Nazeeruddin MK (2008) Langmuir 24:5636–5640
44. De Angelis F, Fantacci S, Selloni A, Grätzel M, Nazeeruddin MK (2007) Nano Lett 7:3189–3195
45. Thomas AG, Flavell WR, Chatwin C, Rayner S, Tsoutsou D, Kumarasinghe AR, Brete D, Johal TK, Patel S, Purton J (2005) Surf Sci 592:159–168

Appendix 7

Barbora Laskova, Thomas Moehl, Ladislav Kavan, Marketa Zukalova, Xianjie Liu, Aswani Yella, Pascal Comte, Arnost Zukal, Mohammad Khaja Nazeeruddin and Michael Graetzel. "Electron Kinetics in Dye Sensitized Solar Cells Employing Anatase with (101) and (001) Facets." *Electrochim. Acta*, 2015, **160**, 296-305.

Electrochimica Acta 160 (2015) 296–305

Contents lists available at ScienceDirect

Electrochimica Acta

journal homepage: www.elsevier.com/locate/electacta

Electron Kinetics in Dye Sensitized Solar Cells Employing Anatase with (101) and (001) Facets

Barbora Laskova [a,b,*], Thomas Moehl [c], Ladislav Kavan [a,b,*], Marketa Zukalova [a], Xianjie Liu [d], Aswani Yella [c], Pascal Comte [c], Arnost Zukal [a], Mohammad Khaja Nazeeruddin [c], Michael Graetzel [c]

[a] J. Heyrovsky Institute of Physical Chemistry, ASCR, v. v. i. Dolejskova 2155/3, Prague 8, CZ 182 23, Czech Republic
[b] Department of Inorganic Chemistry, Faculty of Science, Charles University, Hlavova 2030/8, Prague 2, CZ 128 43, Czech Republic
[c] Laboratory of Photonics and Interfaces Institute of Chemical Sciences and Engineering, Swiss Federal Institute of Technology, Lausanne, CH 1015, Switzerland
[d] Linköping University, Department of Physics, Chemistry and Biology, S-58183 Linköping, Sweden

ARTICLE INFO

Article history:
Received 3 December 2014
Received in revised form 17 January 2015
Accepted 3 February 2015
Available online 4 February 2015

Keywords:
Titanium dioxide anatase
dye-sensitized solar cell
electrochemical impedance spectroscopy
electron transport
nanoparticles

ABSTRACT

Two phase-pure nanocrystalline anatase materials differing in the exposed crystal facets (001) or (101) are studied by electrochemical impedance spectroscopy and by transient photovoltage and photocurrent decay in dye sensitized solar cells. A larger chemical capacitance, indicating larger density of states, is observed for anatase (001). The presence of deep electron traps in (001) nanosheets is further confirmed by optical (UV-Vis) and photoemission (XPS, UPS) spectra. The difference in chemical capacitance indicates a slower diffusion of electrons in the (001) anatase material, but also a higher electron lifetime compared to (101) anatase material.

1. Introduction

TiO_2 (anatase) is an attractive semiconductor material due to its low cost, nontoxicity, chemical stability, abundance and facile synthesis. It has high photocatalytic activity and photostability, what is attractive in photocatalysis[1–4] and in dye sensitized solar cells (DSCs) [5–7]. Anatase has also good Li-storage capacity and charging rate, which predetermines it for application in Li-ion batteries [8–13]. The benefits of anatase nanoparticles for all these applications motivated numerous studies addressing phase purity, particle size and nanocrystals shape [14–25].

Typical anatase nanoparticles have the shape of truncated bipyramids with the main exposed crystal facet (101). The domination of (101) facet (>94% of the total surface area of ordinary crystals)[26] is rationalized by its lowest surface energy. The remaining surface on the anatase crystals is usually the (001) oriented facet [27]. Only rarely, the rhombic-shaped crystals are found, exposing the (010) and (111) facets [28,29]. Yang et al. [26] synthesized micrometer sized platelets of anatase with 47% of (001) facets by using HF as a capping agent under hydrothermal conditions. The follow-up studies reported on particles enriched with up to 90% of the (001) facet [30–32]. The synthesis of anatase enriched with (001) facets[26] triggered deeper investigations of orientation-dependent effects in nanocrystalline anatase materials. They provided various inputs for photocatalysis[33–35], DSCs [36–40] and Li-ion batteries [31,41,42]. These results also activated theoretical studies to explain the observed differences between (101) and (001) facets [32,43–46]. However, there are still some discrepancies in the studies of anatase (101) and (001) [37,38,47,48] which require attention.

Here, we focus on a deeper insight into the electron energetics of anatase (001) and (101) facets. The DSCs employing anatase (101) or anatase (001) as semiconductor photoanodes were prepared and their properties were investigated by electrochemical impedance spectroscopy, transient photovoltage and photocurrent decay. To the best of our knowledge, there is only one paper reporting on the electron kinetics of anatase nanosheets with 30% of (001) facets [40]. It concluded that the nanosheets showed higher chemical capacitance compared to anatase nanoparticles (101). However, nanosheets with only low percentage of (001) facet were used in this work, and the used reference (101) material was P25 (from Degussa/Evonik) which is hardly the optimum standard, because it is a mixture of anatase and rutile [40]. The

* Corresponding authors.
E-mail addresses: laskova@jh-inst.cas.cz (B. Laskova), kavan@jh-inst.cas.cz (L. Kavan).

http://dx.doi.org/10.1016/j.electacta.2015.02.016
0013-4686/

investigation of phase-pure materials remains a challenge. We present here a detailed study of electron kinetics by the analysis of chemical capacitances, diffusion coefficients of electrons and electron lifetimes for phase-pure standard anatase materials with dominating proportion of either (1 0 1) or (0 0 1) facets.

2. Experimental Section

2.1. Materials

The phase-pure anatase (0 0 1) was prepared following the standard synthetic protocol for the TiO_2 nanosheets [26,32,42]. In the actual synthesis, 1.2 mL of 48% hydrofluoric acid was added to 10 mL of titanium(IV) butoxide. The mixture was sealed in a Teflon cell encased in a stainless steel autoclave and heated at 200 °C for 24 h. The sample was then collected, washed with copious amounts of Milli-Q water and dried at 100 °C. The material is further abbreviated as ANA001. The reference phase-pure anatase (1 0 1) material is coded ANA101. It was synthesized by the hydrolysis of Ti(IV)-isopropoxide and hydrothermal recrystallization at 250 °C (in the absence of HF) as detailed elsewhere [49].

2.2. Fabrication of solar cells

The F-doped tin oxide (FTO) conducting glass was covered by a TiO_2 blocking layer. This was made in the bath of 150 mL of H_2O and 5 mL of 2 M $TiCl_4$ for 45 minutes at 75 °C, and subsequently washed with ethanol. The anatase powders were transformed to TiO_2 pastes according to the previously reported procedure [50] and then screen printed on the pre-treated FTO glass. The resulting electrodes were calcined at 500 °C for 30 min in a mode of gradually increasing temperature. The thickness of all ANA101 and ANA001 films, prepared in this way, was 3.45 ± 0.25 μm. The sintered electrodes were post-treated (after cooling to room temperature) in 1 mL of 2 M $TiCl_4$ aqueous solution with 150 mL of H_2O for 20 min at 75 °C. This treatment improved loading of a dye on TiO_2 particles.

The organic dye, [(E)-3-(5-(4-(Bis(2′,4′-dibutoxybiphenyl-4-yl)amino)phenyl) thiophen-2-yl)-2-cyanoacrylic acid] coded D35, was used for sensitization (see[51] for details). The as prepared electrodes were dipped for 14 hours in the solution containing 0.2 mM of the D35-dye in ethanol. After withdrawal, the electrodes were washed with acetonitrile and dried in air at ambient temperature. DSC was assembled with the Surlyn tape (25 μm in thickness) separating the titania photoanode from the counter electrode (platinized FTO glass). Finally, the cell was filled with an iodine- or cobalt-containing electrolyte solutions (see below) and sealed by Surlyn with glass slide. The edges of conductive FTO glasses of the photoanode and cathode were covered by soldering with Cerasolzer alloy 146 (MBR Electronics GmbH) to improve the electrical contacts. The active solar cell area for illumination was 0.28 cm^2. Two types of electrolyte solutions were used: the iodine-based electrolyte Z946 contained 1 M 1, 3-dimethylimidazolium iodide, 0.15 M I_2, 0.5 M N-butylbenzimidazole, and 0.1 M guanidinium thiocyanate in 3-methoxypropionitrile [52]. The cobalt-based electrolyte solution was composed as follows: 0.1 M bis(trifluromethane) sulfonimide (TFSI) lithium salt, 0.5 M nonylpyridine, 0.25 M $[Co^{II}(bpy)_3](TFSI)_2$ (bpy = 2,2′-bipyridine) and 0,06 M $[Co^{III}(bpy)_3](TFSI)_3$.

2.3. Methods

Electrochemical impedance spectroscopy (EIS) was performed with a BioLogic SP300 potentiostat on complete solar cells with an active surface area of 0.28 cm^2 in the dark and under simulated solar illumination close to 1 sun (90 mW cm^{-2}). The applied bias potential was from 0 V to about open-circuit voltage (V_{oc}) in 50 mV steps. A sinusoidal potential perturbation (20 mV amplitude) was applied over the bias potential. The resulting spectra were fitted to the transmission line model[53] with the Zview software (Scribner). Before each electrochemical impedance measurement, the photocurrent-voltage characteristic was tested for the given cell. Transient photovoltage/photocurrent decay was measured under varying light intensities provided by a white-light LED array over which a small red LED light perturbation pulses were superimposed. A source meter (Keithley 2602) recorded the photovoltage and photocurrent dynamics. Photovoltage decays were measured at different open-circuit potentials defined by varying the light intensity. The device's capacitance was obtained from the integrated photocurrent decay measured close to V_{oc} (varying the bias light intensity to probe different V_{oc} values) by charge extraction. Red light perturbation pulses did not exceed 5% of the bias signal resulting from the white-light illumination (either from current or voltage) in order to maintain single-exponential decay:

$$V(t) = V_0 + A\exp(-t/\tau_e) \quad (1)$$

with V_0 and A as fitting coefficients, t as time and τ_e as the electron lifetime.

The Brunauer–Emmett–Teller (BET) surface areas of the prepared materials were determined from nitrogen adsorption isotherms at 77 K using the Micromeritics ASAP 2020 instrument. The amount of adsorbed dye D35 on the films was determined by UV–Vis absorption measurement, recorded with PerkinElmer Lambda 1050 spectrometer, using the dye's extinction coefficient, $\varepsilon_{454} = 17\,000\ M^{-1}\ cm^{-1}$ [54]. The transmittance and reflectance of films for the band gap determination were measured at the same instrument. TEM analysis was carried out on a Jeol JEM – 3010 microscope. The thickness of TiO_2 films was determined by Alpha-step profilometer, Tencor Instruments. The overall porosity of ANA001 and ANA101 films was determined by comparison of the calculated mass of compact anatase in the total film volume and the real mass of the porous layer. The porosity of both types of films were very similar (64% for ANA001 and 65% for ANA101).

Raman spectra were measured on a Micro Raman (LabRam HR, Horiba Jobin-Yvon) instrument with the 633 nm (He-Ne laser) excitation. The X-ray diffraction (XRD) of powders was investigated on a Bruker D8 Advance diffractometer using CuKα radiation. X-ray photoelectron spectroscopy (XPS) and ultraviolet photoelectron spectroscopy (UPS) experiments were carried out using a Scienta ESCA 200 spectrometer in ultrahigh vacuum (ca. 10^{-10} mbar) with an AlKα source and by the He discharged lamp providing photon energies of 1486.6 eV and 21.22 eV, respectively. The full width at half maximum of the clean Au $4f_{7/2}$ line was 0.65 eV at the position of 84.0 eV. The total-energy resolution of the measurements in UPS, determined by Fermi edge of clean gold, was about 90 meV. All spectra were measured at a photoelectron takeoff angle of 0° (normal emission). The UPS spectra have been corrected for the contributions from He I satellites radiation. The work function of sample was extracted from the high binding-energy cutoff of the UPS spectra by applying a bias of −3 V to the sample. To avoid any charge influence on spectrum, both XPS and UPS measurements were measured at varying powers of incident radiation to prove no shifts of the peak positions. In most cases, the charging of our FTO supported, ≈3 μm thick films was very low during the XPS/UPS measurement.

3. Results and Discussion

3.1. Material characterization

Both studied anatase materials were prepared by the commonly used synthetic protocols for crystals with exposed facets (1 0 1) or alternatively (0 0 1). Fig. S1 (Supporting Info) shows that there is no fluorine (F1s signal) detectable by XPS which confirms that our hydrothermal synthesis of ANA001 in the HF medium provides a clean titania surface. The phase purity of the prepared TiO_2 anatase nanosheets ANA001 was confirmed by X-ray diffraction. The corresponding diffractogram is similar to that of the standard phase-pure anatase ANA101 (see Fig. 1a) and in agreement with earlier literature.[26,30,31,38] We should note that the phase purity of (0 0 1) oriented nanosheets requires careful calcination to avoid the presence of cubic $TiOF_2$ [55]. XRD is useful for detection of various titania phases, but it is less sensitive to distinguish the (0 0 1) and (1 0 1) oriented anatase crystals. The diagnostic Bragg peaks for preferential crystal orientation are 0 0 4 and 2 0 0 [29,56,57]. Suppressing and broadening of the 0 0 4 peak is typical for anatase (0 0 1) nanosheets together with the intensity increase of the 2 0 0 peak [29,56]. The ANA001 sample exhibits the expected changes as shown in Fig. 1a. Quantitative analysis of the percentage of (0 0 1) facets can be carried out by Raman spectroscopy.

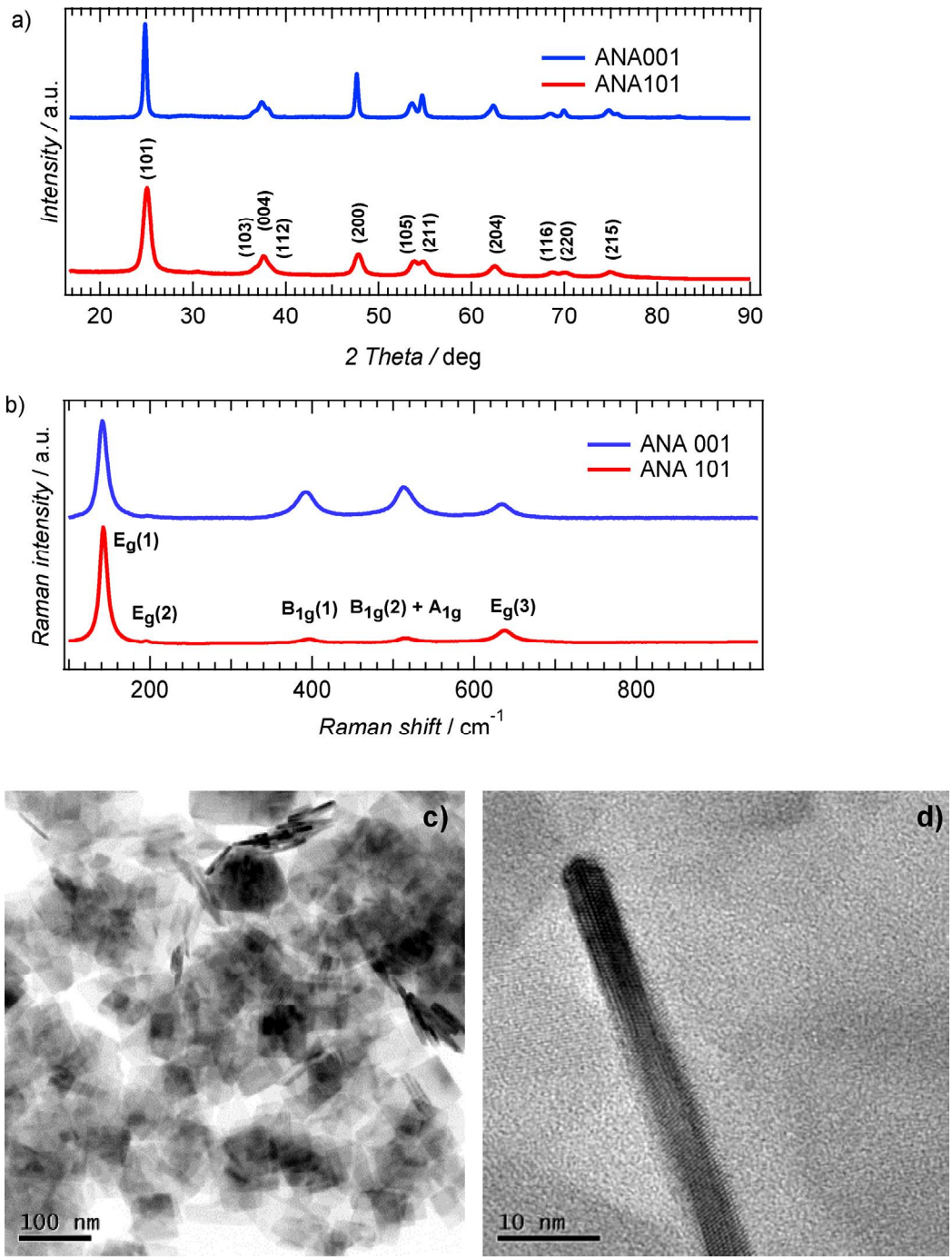

Fig. 1. (a) Powder X-ray diffraction patterns of ANA001 and ANA101 samples. (b) Raman spectra of ANA001 and ANA101 samples. Bottom charts (c, d) show the transmission electron microscopy images of the ANA001 sample.

Enrichment by the (0 0 1) facet enhances the intensity of $B_{1g}(1)$ and $(B_{1g}(2)+A_{1g})$ Raman modes referenced to the intensity of $E_g(1)$ or $E_g(3)$ modes [56,58]. These changes are clearly visible in the spectra of ANA001 and ANA101 samples (Fig. 1b). The percentage of (0 0 1) facets was calculated from the peak areas of the $B_{1g}(2)+A_{1g}$ mode (at 514 cm^{-1}) and the $E_g(1)$ mode (at 144 cm^{-1}) as detailed elsewhere [56,58]. The proportion of (1 0 1) facets in ANA101 was 90%, which is typical for common anatase nanoparticles [56]. On the other hand, the ANA001 sample had 71% of the (0 0 1) facet.

The transmission electron microscopy (TEM) images of our ANA001 nanosheets are shown in Figs. 1c and 1d. The morphology of rectangular nanoplatelets with predominant facet (0 0 1) can be clearly observed. Typical thickness of the platelets was ~ 5–8 nm and the average size about 50 nm. The specific surface area of ANA001 powder was determined by nitrogen absorption measurement as S_{BET} = 75 m^2/g. This value is close to the calculated surface area of an anatase platelet of 55 nm × 55 nm × 8 nm in size, which is 83 m^2/g. The control material, ANA101 is a nanocrystalline anatase with a well comparable surface area, S_{BET} = 84 m^2/g. The crystal morphology of ANA101 is characterized by particles of 20 nm in size exposing mainly the (1 0 1) facets. This material is frequently used for fabrication of photoanodes in DSCs [49,59].

3.2. Solar cell characterization

The dye loading of D35 dye was by about 30% lower for ANA001 than for ANA101 films. This observation matches the earlier theoretical[46] and experimental[37,38] studies of the adsorption of ruthenium based dyes on (0 0 1) and (1 0 1) facets (see however[40] for an opposite statement). To the best of our knowledge, there is no reference study of the loading of metal-free organic dyes. The current/voltage curves recorded under illumination close to 1 sun are presented in Fig. 2 for our four different types of devices together with the solar conversion efficiencies, η. Detailed photovoltaic parameters are summarized in Table 1. The maximal efficiency of solar cells employing organic dye D35 at 1 sun illumination was reported to be 5.5% for the iodide/triiodide redox couple and 6.7% for the $[Co(bpy)_3]^{3+/2+}$ redox couple [60]. The efficiencies of our devices in Fig. 2 are similar considering the fact that our anatase films had about half the thickness and did not contain any scattering overlayers in the photoanodes as in the cited works. The scattering layer was omitted in our study to simplify the system for easier interpretation of electrochemical impedance spectroscopy data. The difference in J_{sc} can be attributed to either different dye loading (see above) or to different charge collection efficiency. (We will show below that the second difference is negligible). The fill factors (*FF*) of ANA101- and ANA001-based DSCs are close too (Table 1). Fill factor is better in iodine-based electrolyte solutions, which have faster mediator diffusion. The open-circuit voltage (*Voc*) of DSCs with the cobalt-based electrolyte solution is larger, due to the considerably more positive redox potential of the $[Co(bpy)_3]^{3+/2+}$ redox couple.

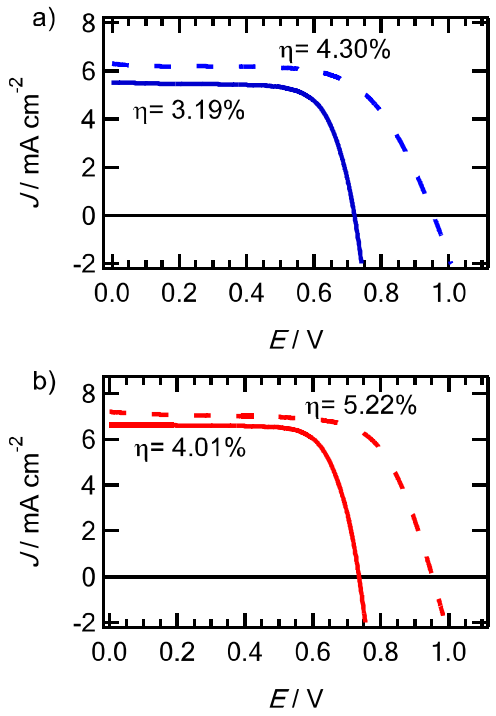

Fig. 2. The current/voltage characteristics of DSCs with ANA001 photoanode (a) and ANA101 photoanode (b). The DSCs were assembled with either iodine-based electrolyte solutions (full lines) or cobalt-based electrolyte solutions (dashed lines). The corresponding solar conversion efficiencies η of the cells are annotated in the charts. The curves were measured before EIS measurement at simulated solar illumination of 90 mW cm^{-2} power.

Table 1
The photovoltaic parameters of DSCs with ANA101 or ANA001 photoanodes at simulated solar illumination of 90 mWcm^{-2} power. The DSCs were assembled with either iodine-based electrolyte solution or cobalt-based electrolyte solution.

Photoanode	Electrolyte type	J_{sc} (mA/cm^2)	V_{oc} (V)	*FF*	η (%)
ANA101	Iodine-based	6.62	0.736	0.74	4.01
	Cobalt-based	7.21	0.953	0.69	5.22
ANA001	Iodine-based	5.52	0.720	0.72	3.19
	Cobalt-based	6.31	0.955	0.64	4.30

3.3. Electrochemical impedance spectroscopy

Electrochemical impedance is a useful technique for the determination of electronic properties of DSCs like the electron lifetime, diffusion coefficient of electrons and density of states (DOS) in the TiO_2 photoanode [53,61,62]. The impedance spectra of solar cells with ANA001- and ANA101-based photoanodes were measured in dark and under illumination close to 1 sun in the range of potentials between 0 V and open circuit potential (V_{oc}). The measurements were carried out both in the I-containing and Co-containing electrolyte solutions. The main parameters which can be extracted from the impedance spectra fitting are: the charge-transfer resistance, R_{ct} representing the recombination of electrons from TiO_2 with the oxidized form of the redox couple in electrolyte solution, the transport resistance, R_t for electrons inside TiO_2 and the chemical capacitance, C_μ which represents filling of trap states in the mesoporous metal oxide.

The dependence of R_{ct},R_t and C_μ on applied potential under illumination for all four devices (as in Fig. 2) is summarized in Figs. 3a and b. Interestingly, the chemical capacitance is much larger in ANA001 compared to ANA101 in both electrolyte solutions. For example, in the iodine-based electrolyte, the C_μ/potential plot for the ANA001 downshifts by about 100–140 mV, and the R_t/potential plot downshifts by about 70–90 mV compared to ANA101 although the open circuit voltages of the corresponding DSCs are similar (Fig. 2, Table 1). The same trend was observed for the measurements in dark.

Chemical capacitance represents filling of trap states below the titania conduction band. It is related to the density of states (DOS) by the equation:

$$DOS = 6.24 \cdot 10^{18} \frac{C_\mu}{L(1-p)} \quad (2)$$

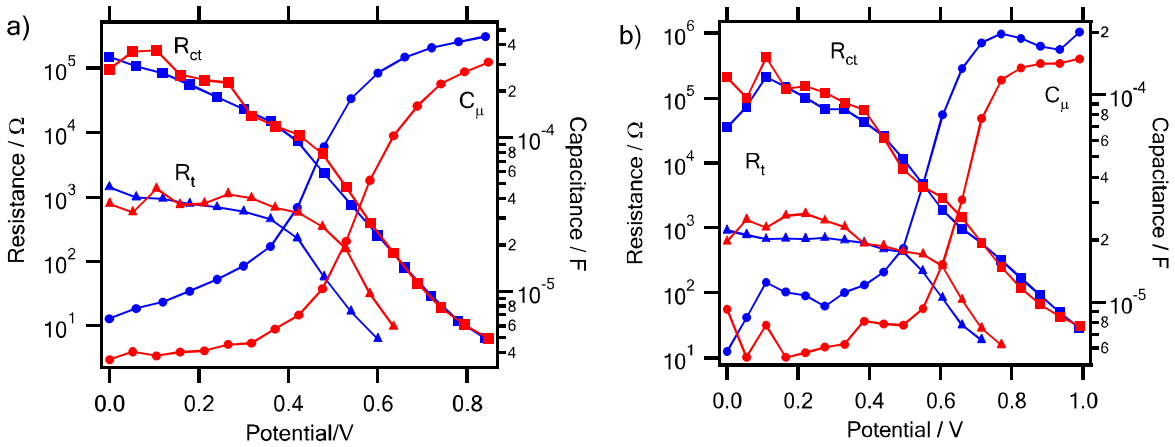

Fig. 3. Results from the fitting of impedance spectra of DSCs under illumination. The potential dependence is shown for the charge transfer resistance (R_{ct}; squares), transport resistance (R_t; triangles) and the chemical capacitance (C_μ; circles) in DSCs. The solar cells were assembled with either iodine-based electrolyte solution (chart a) or with cobalt-based electrolyte solution (chart b). The devices employing ANA001 films are depicted by blue colored symbols and the devices with ANA101 films are depicted by red colored symbols. The lines between points are guides to eye. (For interpretation of the references to color in this figure legend, the reader is referred to the web version of this article.)

where L is a thickness of the TiO_2 film and p is its porosity [63]. As the porosities and thicknesses in all our films are almost identical (see Experimental section), the found chemical capacitances are representative for a direct comparison of DOS. The actual data, calculated from Eq. (2) are shown in Fig. S2 (Supplementary Information). They indicate higher DOS for ANA001 at the given potential. Closer inspection of DOS reveals different distribution of states in the two studied anatase materials. This can be addressed by fitting of the found chemical capacitances to the following formula[64]:

$$C_\mu = C_{0,\mu} \exp\left[\alpha \frac{qV}{k_B T}\right] \quad (3)$$

where k_B is Boltzmann constant, T is temperature, q is elemental charge and V is the applied potential. From fitting we access the parameter α, which accounts for the trap distribution below the conduction band, and the temperature T_0 (defined as $T_0 = T/\alpha$) which indicates the depth of the distribution [64]. Nanocrystalline TiO_2 photoanodes typically show the T_0 values around 800–1200 K. [64–66] Our values of α and T_0 are summarized in Table 2.

The data in Table 2 clearly confirm a different distribution of traps for ANA001 and ANA101. They indicate a higher DOS, i.e. a higher amount of trap states in the (0 0 1)-anatase nanosheets compared to the (1 0 1)-anatase nanoparticles. This conclusion is supported also by a theoretical study of Lamiel-Garcia et al. [45]. To further explore this point, we have investigated the electronic structure of our materials by optical and photoemission spectroscopy.

3.4. Electronic structure of titania (0 0 1)/(1 0 1)

Since the chemical capacitance depends on the conduction band edge position, the corresponding changes of C_μ are related to the electronic structure of the particular material [61,62]. To address this point, the band positions were examined by UPS (Figs. S3 and S4, Supporting Info). Furthermore, the band-gap was determined from transmittance/reflectance UV-Vis spectra [67,68] using the Tauc plot[68,69] (Fig. S5 Supporting Info). Our found band-gap for ANA001 (3.18 eV) is in perfect agreement with the literature value of Pan et al. [48], but our band-gap for ANA101 (3.20 eV) is slightly smaller than the value of 3.22 eV from the same work [48]. Such tiny differences are ascribed to experimental errors. Recently, Xu et al. [29] reported 3.01 eV and 3.04 eV for the (0 0 1) and (1 0 1) oriented anatase, respectively. Although their absolute values are smaller, the difference is negligible, too. Hence, we note that the bandgap is virtually invariant with the (0 0 1)/(1 0 1) orientations.

Table 2
The calculated parameters from fitting of chemical capacitances to Eq. (3).

Electrolyte type	Sample	α	T_0 (K)
Cobalt-based	ANA001	0.38	784
	ANA101	0.52	573
Iodide-based	ANA001	0.36	824
	ANA101	0.47	634

UPS indicates that the valence-band maximum is upshifted by 0.1 eV for the ANA001 referenced to ANA101 (Fig. S3, Supporting Info). If we assume the same bandgap for both materials (see previous paragraph) the conduction band (CB) edge should be upshifted by 0.1 eV, too. This finding is in remarkable agreement with the theoretical (DFT calculation) by de Angelis et al. [46] (predicting the upshift of CB by 50–110 meV) and with the electrochemical flatband potentials reported by Hengerer et al. [8] (upshift of CB by 60 meV) but it contradicts the earlier works by Pan et al. [48] and Xu et al. [29] who assumed the valence-band maximum (VBM) to be identical for all anatase crystal orientations. To rationalize this discrepancy, we should note that the cited works [29,48] used solely XPS, which does not seem to be sensitive enough to distinguish such small differences (cf. also our Fig. S1c and Refs. [29,38,48]). Our VBM from XPS equals ≈3.4 eV for both samples (Figure S1c); Pan et al. [48] reported 1.93 eV for both orientations; still another XPS work by Scanlon et al. [70] reported 2.77 eV from anatase of unspecified orientation, and Liu et al. [71] found 3.28 eV by UPS. The large spread of absolute values of VBMs from different source works seems to reflect specific conditions of sample preparation and photoemission measurement, hence solely relative differences are relevant in each given work.

UPS further allows accurate determination of a work function (Fig. S4). The found values are 4.04 and 4.06 eV for ANA001 and ANA101, respectively, which is a negligible difference. Our data compare reasonably well with the work function of 4.1 eV, reported earlier by Liu et al. [71] for anatase of unspecified orientation. (But we assume that the (1 0 1) face was dominating in their sample as in most ordinary anatase materials). The fact that our two studied samples (ANA001 and ANA101) have almost identical work functions and identical optical band-gaps, but the ANA001 has upshifted conduction band edge, is a virtual paradox,

but it can be rationalized as a consequence of large density of trapped electrons in the ANA001. In other words, high DOS of trapped electrons can pin the Fermi level of the ANA001. The work function in ANA001 comes actually from the electrons in deep trapped states which, in turn, move the Fermi level close to the vacuum level. This effect is illustrated also by XPS, where we see a marked difference in the Ti2p, O1s peak positions between ANA001 and ANA101 (Figs. S1b,d). If we assume that the trapped electrons pin the Fermi level in ANA001, then the distance between the Fermi level and the (O1s, Ti2p) core levels increases for ANA001. Consequently, the Ti2p and O1s lines have larger binding energy in ANA001 which agrees with our observation (Fig. S1).

Additional arguments in favor of trapped electrons in ANA001 come from detailed scrutiny of optical (UV-Vis) spectra. Fig. S6 (Supporting Info) shows an analysis of the so-called Urbach tail of the absorption edge in the optical spectrum. From the linear fits, we can calculate the Urbach energy of 87 meV and 50 meV for ANA001 and ANA101, respectively. The found difference is attributed to a larger density of trapped electrons below the conduction band edge in ANA001, *vide ultra*. Obviously, the small difference in the conduction-band edge position, E_{cb} cannot cause such a large difference in the C_μ observed in our EIS measurements (Section 3.3). This leads to a logical conclusion that the C_μ enhancement for ANA001 is actually caused by larger number of electron traps in this material.

3.5. Transient photovoltage and photocurrent decay

Transient photovoltage and photocurrent decay are alternative techniques to confirm the differences in C_μ found from EIS. Fig. S7 (Supporting Info) shows the corresponding capacitances, C_μ of ANA001 and ANA101 in devices with iodine based electrolyte solutions. These data support our results from EIS, indicating a significantly larger chemical capacitance for the anatase ANA001-based DSCs. They further support theoretical predictions about higher density of states near the bottom of the conduction band for anatase (0 0 1) compared to that in anatase (1 0 1). [45] Similar trends were also observed by Hao et al. [40] who compared the anatase particles containing 30% of (0 0 1) facets with a TiO_2 mixture of anatase and rutile, known as P25 (Degussa/Evonik; about 70–80% anatase to 20–30% rutile) [40,72,73]. However, the rutile component (in their reference material) together with a lower quality (percentage of (0 0 1) facets) of their target material could complicate this study, too. Furthermore, Hao et al. [40] observed larger dye loading (Ru-based dye N719) for their anatase with (0 0 1) facets compared to the used reference (P25) which contradicts our data too (see above). In our study, we used phase-pure anatase materials with higher enrichment of (1 0 1)/(0 0 1), and found smaller dye loading and significantly larger chemical capacitance for DSCs with ANA001 compared to ANA101 (see Fig. 3, Fig. S7).

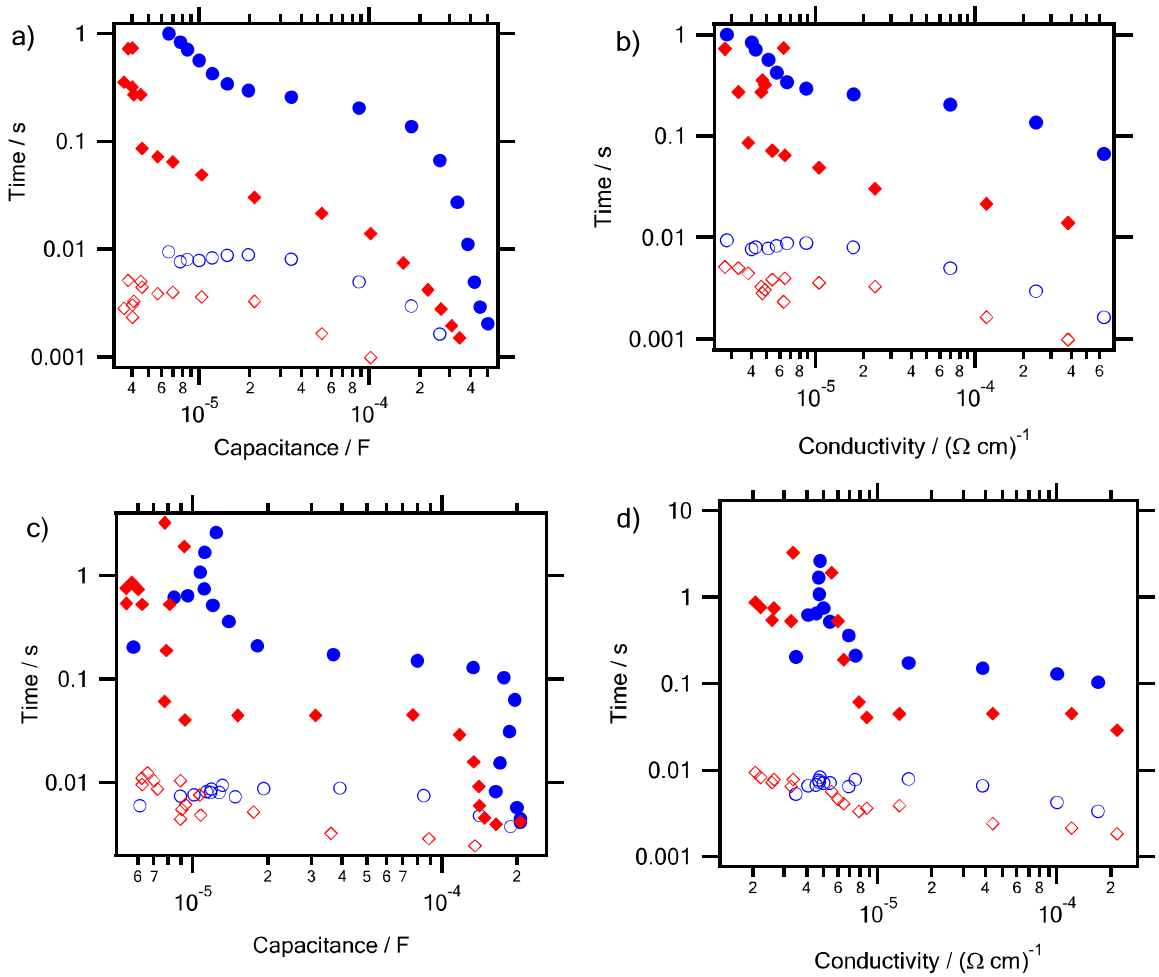

Fig. 4. Electron lifetimes (full points) and transport times (open points) plotted against the chemical capacitance (left column) and conductivity (right column) for DSCs under illumination containing either iodine-based electrolyte solution (charts a, b) or cobalt-based electrolyte solution (charts c, d). Red-colored diamonds: ANA101, blue-colored circles: ANA001. (For interpretation of the references to color in this figure legend, the reader is referred to the web version of this article.)

3.6. Electron dynamics in titania (001)/(101)

The found very similar *Voc* values of our final devices (Fig. 2, Table 1) indicate that the solar cells with ANA001 have a different recombination resistance in relation to chemical capacitance (which is clearly indicated by higher C_μ or DOS at a similar R_{ct}). This can be followed by the lifetime of electrons, τ_e inside the mesoporous metal oxide [61]:

$$\tau_e = R_{ct} \cdot C_\mu \tag{4}$$

In general, the electron lifetime (or the charge transfer resistance) should be compared at a similar electron density inside the TiO_2 conduction band. Normally, under the assumption of similar E_{cb} position and similar trap distribution, one can use the applied potential as a reference. If there are differences in the conduction band position, but the trap distribution is the same, one can use the chemical capacitance or the DOS to level the E_{cb} difference. A third possibility is to compare the electron lifetimes against the conductivity of TiO_2. The latter is given by the amount of electrons thermalized from the DOS into the conduction band. The conductivity, σ is associated with the measured transport resistance R_t:

$$\sigma = \frac{L}{R_t A(1-p)} \tag{5}$$

where L is a thickness of the TiO_2 film, p is its porosity and A is the film area [61]. Therefore this way of comparison is only possible in a potential region in which the transport resistance of the TiO_2 can be determined by EIS.

As we showed by photoemission spectra (see Section 3.5), the actual E_{cb} is slightly higher for the ANA001 compared to ANA101. Also the DOS cannot be a clear measure for the amount of thermalized electrons inside the conduction band for the comparison of the two different types of anatase, as discussed in Section 3.3. Therefore, there is no clear reference point as there might be a difference in the E_{cb} or in the trap distribution for comparing the recombination resistance or the electron lifetime.

Nevertheless, we can compare the electron lifetime, τ_e against the chemical capacitance and the conductivity of the TiO_2 (Fig. 4). Clearly, in both cases the electron lifetime is higher for the ANA001 though the difference in the electron lifetimes is somewhat smaller in the conductivity-referenced plots (Fig. 4 b, d). The expected difference in V_{oc} can be calculated for the two types of devices, ANA001 and ANA101 from the formula:

$$\Delta V_{oc} = \frac{k_B T}{q} \ln\left(\frac{\tau_{n1}}{\tau_{n2}}\right) \tag{6}$$

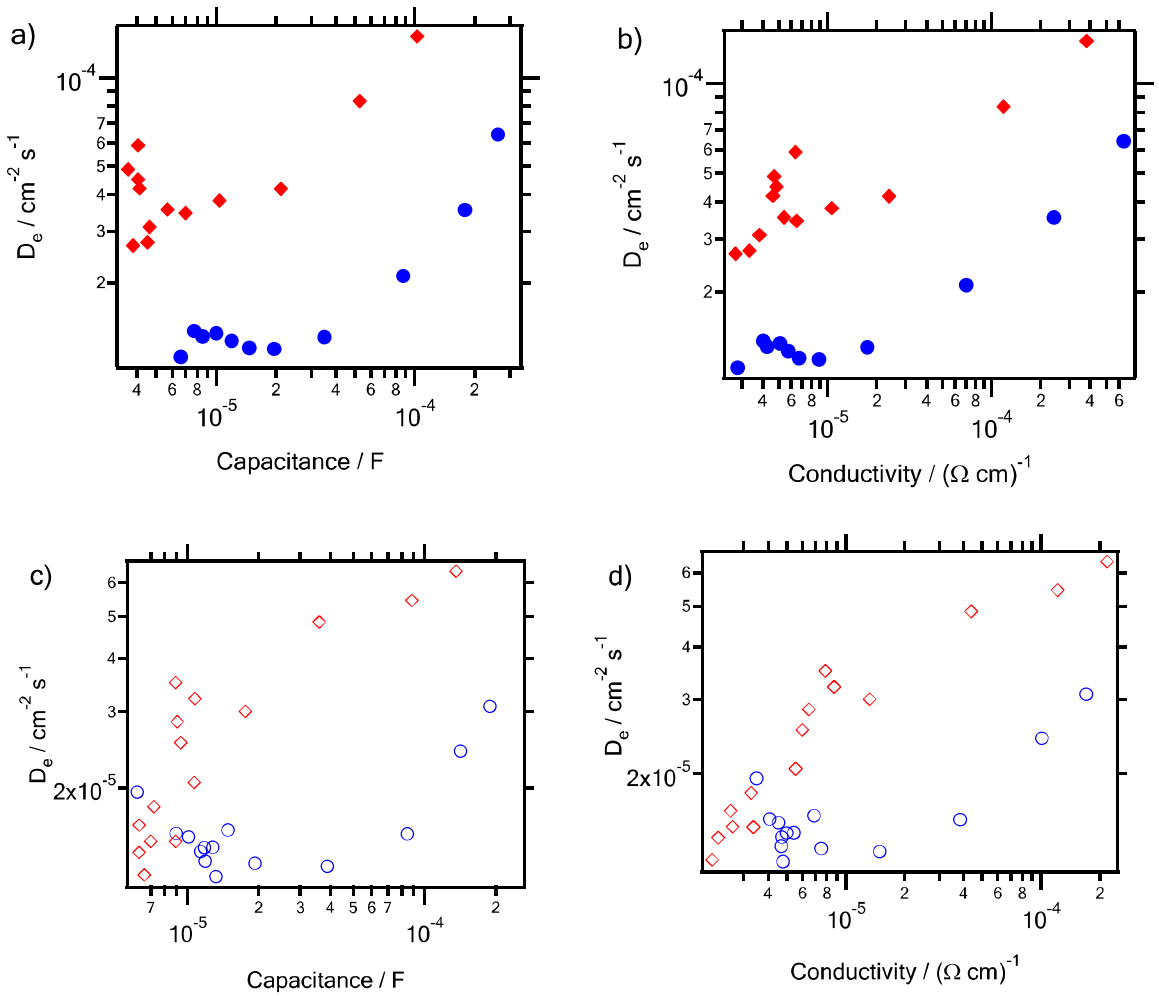

Fig. 5. Diffusion coefficient of electrons as a function of chemical capacitance (left column) and conductivity (right column) for ANA001 (blue circles) or ANA101 (red diamonds) films. The diffusion coefficient of electrons was computed from impedance spectra of DSCs with iodine-based electrolyte solution (a,b) and with cobalt-based electrolyte solution (c,d). (For interpretation of the references to color in this figure legend, the reader is referred to the web version of this article.)

with τ_{n1},τ_{n2} being electron lifetimes for the two compared devices. Eq. (6) and our data (Fig. 4) give: $\Delta V_{oc} \approx 75$ mV (from capacitance at about 10^{-4} F) or $\Delta V_{oc} \approx 45$ mV (from the conductivity at about $4 \cdot 10^{-4}\,\Omega^{-1}\,cm^{-1}$), respectively, for the cells with iodine-based electrolyte. This prediction, however, does not match the experimental ΔV_{oc} (−16 mV for I-based electrolyte solution, see Table 1). Hence, the virtual gain in V_{oc} determined from the electron lifetimes (Eq. (6)) has to be compensated by a lower conduction band position of the ANA001. The estimated downshift of ANA001 conduction band is thus predicted to be ≈90 mV from capacitance and ≈60 mV from conductivity. These values roughly agree with the predicted R_t downshift of 70–90 mV and are lower than 100–140 mV for C_μ which was already discussed in Section 3.3. Yet there is a qualitative difference, if we recall the corresponding data from DFT calculations, optical and photoemission measurements (see Section 3.4 for details). They predict just the opposite, i.e. upshift for ANA001. The reason for this discrepancy is unknown at this stage of our research. We may only note that the vacuum techniques (XPS, UPS) inherently ignore the presence of electrolyte, solvent, dye etc. which occur in real interfaces, and similar simplifications are included in theoretical (DFT) calculations, too. In fact, very similar qualitative discrepancy is found, if we recall earlier electrochemical, XPS and theoretical data for anatase/rutile comparison [70,74]. Also in this case, the band positions do not match for unclear reasons, either.

Interestingly, the transport time, τ_t of electrons inside the mesoporous TiO_2[61]:

$$\tau_t = R_t \cdot C_\mu \tag{7}$$

is higher in ANA001 compared to ANA101 (cf. Fig. 4). To gain further insight to the charge-transport in TiO_2 we plotted the diffusion coefficients of electrons against the chemical capacitance and the conductivity. These diffusion coefficients, D_e can be determined from the chemical capacitances and transport resistances, R_t, using the equation [61]:

$$D_e = \frac{L^2}{R_t C_\mu} \tag{8}$$

The calculated diffusion coefficients for ANA001 and ANA101 are displayed in Figure 5. The anatase nanoparticles (1 0 1) exhibit faster diffusion of electrons than the anatase nanosheets (0 0 1). This is in agreement with the above presented data for τ_t and it can be interpreted as a result of multiple trapping of electrons in the ANA001 material, caused by higher amount of traps in ANA001 compared to ANA101. A precise determination of the diffusion coefficient and the electron lifetime is given by conditions of quasistatic model by Bisquert et. al.[75] However, the above presented method is obviously acceptable for comparison of the electronic properties of two similar materials.

Nakade et al. [21,76] investigated the influence of anatase nanoparticle preparation, particle size and annealing temperature on the diffusion, recombination and efficiency of the DSCs. They found that surface area and particle size have the decisive influence. TiO_2 films with bigger particles (smaller surface area) have higher diffusion coefficient of electrons, lower amount of traps and lower electron lifetime [21,76]. This observation is attributed to the effects of particle sintering and grain boundaries. The bigger particles have lower surface area and larger necking cross-sections between sintered particles, which leads to the increase of diffusion coefficient and decrease of lifetime. The increase of diffusion coefficient and decrease of trap density with smaller surface area was also observed by Kopidakis et al. [77]

A similar trend, but in an opposite direction, was observed in our work. The anatase (0 0 1) material evidenced lower diffusion coefficient of electrons, higher amount of traps and higher electron lifetime than the devices made with anatase (1 0 1), in spite of a slightly lower surface area of the anatase nanosheets ANA001 ($S_{BET} = 75\,m^2/g$) compared to anatase nanoparticles ANA101 ($S_{BET} = 84\,m^2/g$). Hence, one explanation of the found higher chemical capacitance for ANA001 nanoplatelets could be an effect of different growth of anatase (0 0 1) crystals and a different sintering process compared to the standard anatase nanoparticles (1 0 1). A second possible explanation is that the larger C_μ is an intrinsic property of nanocrystals with the exposed (0 0 1) facets. An increase of electron lifetime for ANA001, compared to ANA101 is obvious, and this higher lifetime of electrons also plays a role in better photocatalytic activity of anatase (001) nanosheets compared to anatase nanoparticles (1 0 1) which was also reported by others [28,30].

Although there are clear differences in the transport time and the diffusion coefficient for the electrons, still both devices show high charge collection efficiencies [78]:

$$\eta_{col} = 1/[1 + (\tau_t/\tau_e)] \tag{9}$$

due to the longer electron lifetimes compared to the transport time in both cases.

The calculated values for η_{col} are shown in Fig. 6 for all four types of our DSCs. The charge collection efficiency is close to unity for both ANA001 and ANA101 photoanodes, in spite of the differences in τ_e and τ_t. The used formula for η_{col} is an approximation underestimating the charge collection efficiency, thus giving the lower limit of η_{col} [79]. The found high charge collection efficiencies for both types of facets show that the above discussed lower solar conversion efficiencies for DSCs employing ANA001 compared to ANA101 are caused by smaller dye loading of ANA001, which leads to lower $J_{sc,}$ (Table 1) and shift of the

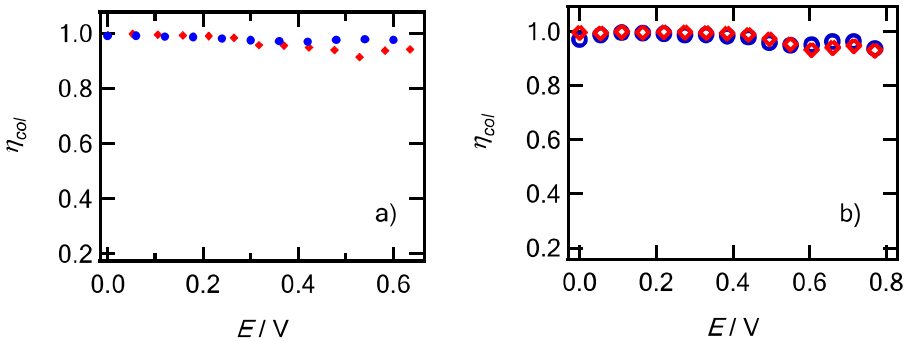

Fig. 6. The charge collection efficiency against applied potential determined from electrochemical impedance of DSCs containing either iodine-based electrolyte solution (a) or cobalt-based electrolyte solution (b). The devices employing ANA001 material are depicted by blue circles and these based on ANA101 films are depicted by red diamonds. (For interpretation of the references to color in this figure legend, the reader is referred to the web version of this article.)

conduction band of the ANA001. Though the charge collection efficiency is very close for the two different TiO_2 particles, one clear advantage of the ANA001 is the fact that the difference between the τ_e and τ_t is higher for ANA001 compared to ANA101 especially at higher forward bias (see Fig. 4). This enables the ANA001 particles to be used in thicker mesoporous metal oxide films as photoanode without significant drop of the efficiency.

4. Conclusions

Two phase-pure anatase materials differing in the exposed crystal facet of (0 0 1) or (1 0 1) were prepared by the hydrothermal synthesis. Properties of these two types of anatase nanocrystals were studied by electrochemical impedance spectroscopy and by transient photovoltage and photocurrent decay measurements on complete dye sensitized solar cells.

A larger chemical capacitance was found for the anatase nanosheets with the exposed facets (0 0 1) compared to the anatase nanoparticles with the predominant (1 0 1) facet. These results indicate a higher amount of electron traps for the anatase nanosheets than for the anatase nanoparticles. The presence of deep electron traps in (0 0 1) nanosheets is further confirmed by optical (UV-Vis) and photoemission (XPS, UPS) spectra.

A larger number of electron traps in the anatase (0 0 1) nanosheets decreases the diffusion coefficient of electrons in this material due to multiple electron-trapping. On the other hand, it results in larger electron lifetime in the (0 0 1) nanosheets, which can contribute to their previously reported better photocatalytic activity. For the solar cell performance, the slower transport and the longer lifetime for the (0 0 1) nanoplatelets leads to a similar charge collection efficiency as in the (1 0 1) particles.

Acknowledgement

This work was supported by the Sciex-NMS^{ch} programme (project 12.376) and by the Grant Agency of the Czech Republic (contracts Nos 13-07724S and P108/12/0814). M.G. and T.M. acknowledge the European Research Council (ERC) for an Advanced Research Grant (ARG no. 247404) funded under the 'Mesolight' project. X.L. acknowledges support from the Swedish Research Council Linnaeus grant LiLi-NFM. We are grateful to Mariana Klementova for the TEM images and to Ondrej Vik for thin films analyses.

Appendix A. Supplementary data

Supplementary data associated with this article can be found, in the online version, at http://dx.doi.org/10.1016/j.electacta.2015.02.016.

References

[1] A.L. Linsebigler, G. Lu, J.T. Yates, Chem. Rev. 95 (1995) 735.
[2] J. Zhang, Q. Xu, Z. Feng, M. Li, C. Li, Angew. Chem., Int. Ed. 47 (2008) 1766.
[3] M.A. Henderson, Surf. Sci. Rep. 66 (2011) 185.
[4] H.H. Chen, C.E. Nanayakkara, V.H. Grassian, Chem. Rev 112 (2012) 5919.
[5] B. O'Regan, M. Grätzel, Nature 353 (1991) 737.
[6] A. Hagfeldt, G. Boschloo, L.C. Sun, L. Kloo, H. Pettersson, Chem. Rev 110 (2010) 6595.
[7] A. Yella, H.W. Lee, H.N. Tsao, C.Y. Yi, A.K. Chandiran, Science 334 (2011) 1203.
[8] R. Hengerer, L. Kavan, P. Krtil, M. Grätzel, J. Electrochem. Soc. 147 (2000) 1467.
[9] M. Wagemaker, A.P.M. Kentgens, F.M. Mulder, Nature 418 (2002) 397.
[10] M. Wagemaker, G.J. Kearley, A.A. Van Well, H. Mutka, F.M. Mulder, J. Am. Chem. Soc. 125 (2003) 840.
[11] L. Kavan, Chem. Rec. 12 (2012) 131.
[12] B. Laskova, O. Frank, M. Zukalova, M. Bousa, M. Dracinsky, L. Kavan, Chem. Mater. 25 (2013) 3710.
[13] L. Kavan, J. Solid State Electrochem. 18 (2014) 2297.
[14] J. Prochazka, L. Kavan, V. Shklover, M. Zukalova, O. Frank, M. Kalbac, A. Zukal, H. Pelouchova, P. Janda, K. Mocek, M. Klementova, D. Carbonne, Chem. Mater. 20 (2008) 2985.
[15] J. Prochazka, L. Kavan, M. Zukalova, O. Frank, M. Kalbac, A. Zukal, M. Klementova, D. Carbonne, M. Grätzel, Chem. Mater. 21 (2009) 1457.
[16] V. Gentili, S. Brutti, L.J. Hardwick, A.R. Armstrong, S. Panero, P.G. Bruce, Chem. Mater. 24 (2012) 4468.
[17] K. Zhu, N.R. Neale, A. Miedaner, A.J. Frank, Nano Lett. 7 (2007) 69.
[18] J.M. Macak, M. Zlamal, J. Krysa, P. Schmuki, Small 3 (2007) 300.
[19] G. Liu, H.G. Yang, J. Pan, Y.Q. Yang, G.Q. Lu, H.M. Cheng, Chem. Rev. 114 (2014) 9559.
[20] L. Sang, Y. Zhao, C. Burda, Chem. Rev. 114 (2014) 9283.
[21] S. Nakade, Y. Saito, W. Kubo, T. Kitamura, Y. Wada, S. Yanagida, J. Phys. Chem. B 107 (2003) 8607.
[22] R. Agosta, R. Giannuzzi, L. De Marco, M. Manca, M.R. Belviso, P.D. Cozzoli, G. Gigli, Journal of Physical Chemistry C 117 (2013) 2574.
[23] R. Buonsanti, E. Carlino, C. Giannini, D. Altamura, L. De Marco, R. Giannuzzi, M. Manca, G. Gigli, P.D. Cozzoli, Journal of the American Chemical Society 133 (2011) 19216.
[24] L. De Marco, M. Manca, R. Buonsanti, R. Giannuzzi, F. Malara, P. Pareo, L. Martiradonna, N.M. Giancaspro, P.D. Cozzoli, G. Gigli, Journal of Materials Chemistry 21 (2011) 13371.
[25] L. De Marco, M. Manca, R. Giannuzzi, M.R. Belviso, P.D. Cozzoli, G. Gigli, Energy & Environmental Science 6 (2013) 1791.
[26] H.G. Yang, C.H. Sun, S.Z. Qiao, J. Zou, G. Liu, S.C. Smith, H.M. Cheng, G.Q. Lu, Nature 453 (2008) 638.
[27] C.L. Olson, J. Nelson, M.S. Islam, J. Phys. Chem. B 110 (2006) 9995.
[28] B.H. Wu, C.Y. Guo, N.F. Zheng, Z.X. Xie, G.D. Stucky, J. Am. Chem. Soc. 130 (2008) 17563.
[29] H. Xu, P. Reunchan, S. Ouyang, H. Tong, N. Umezawa, T. Kako, J. Ye, Chem. Mater. 25 (2013) 405.
[30] X.G. Han, Q. Kuang, M.S. Jin, Z.X. Xie, L.S. Zheng, J. Am. Chem. Soc. 131 (2009) 3152.
[31] J.S. Chen, X.W. Lou, Electrochem. Commun 11 (2009) 2332.
[32] X.H. Yang, Z. Li, C.H. Sun, H.G. Yang, C.Z. Li, Chem. Mater. 23 (2011) 3486.
[33] H.G. Yang, G. Liu, S.Z. Qiao, C.H. Sun, Y.G. Jin, S.C. Smith, J. Zou, H.M. Cheng, G.Q. Lu, J. Am. Chem. Soc. 131 (2009) 4078.
[34] G. Liu, C.H. Sun, H.G. Yang, S.C. Smith, L.Z. Wang, G.Q. Lu, H.M. Cheng, Chem. Commun. 46 (2010) 755.
[35] J.G. Yu, L.F. Qi, M. Jaroniec, J. Phys. Chem. C 114 (2010) 13118.
[36] W.G. Yang, J.M. Li, Y.L. Wang, F. Zhu, W.M. Shi, F.R. Wan, D.S. Xu, Chem. Commun. 47 (2011) 1809.
[37] J. Yu, J. Fan, K. Lv, Nanoscale 2 (2010) 2144.
[38] B. Laskova, M. Zukalova, L. Kavan, A. Chou, P. Liska, Z. Wei, L. Bin, P. Kubat, E. Ghadiri, J.E. Moser, M. Gratzel, J. Solid State Electrochem. 16 (2012) 2993.
[39] H.M. Zhang, Y.H. Han, X.L. Liu, P.R. Liu, H. Yu, S.Q. Zhang, X.D. Yao, H.J. Zhao, Chem. Commun. 46 (2010) 8395.
[40] F. Hao, X. Wang, C. Zhou, X.J. Jiao, X. Li, J.B. Li, H. Lin, J. Phys. Chem. C 116 (2012) 19164.
[41] C.H. Sun, X.H. Yang, J.S. Chen, Z. Li, X.W. Lou, C.Z. Li, S.C. Smith, G.Q. Lu, H.G. Yang, Chem. Commun. 46 (2010) 6129.
[42] M. Bousa, B. Laskova, M. Zukalova, J. Prochazka, A. Chou, L. Kavan, J. Electrochem. Soc. 157 (2010) A1108–A1112.
[43] M. Sumita, C.P. Hu, Y. Tateyama, J. Phys. Chem. C 114 (2010) 18529.
[44] S. Selcuk, A. Selloni, J. Phys. Chem. C 117 (2013) 6358.
[45] O. Lamiel-Garcia, S. Tosoni, F. Illas, J. Phys. Chem. C 118 (2014) 13667.
[46] F. De Angelis, G. Vitillaro, L. Kavan, M.K. Nazeeruddin, M. Gratzel, J. Phys. Chem. C 116 (2012) 18124.
[47] T.R. Gordon, M. Cargnello, T. Paik, F. Mangolini, R.T. Weber, P. Fornasiero, C.B. Murray, J. Am. Chem. Soc 134 (2012) 6751.
[48] J. Pan, G. Liu, G.M. Lu, H.M. Cheng, Angew. Chem., Int. Ed. 50 (2011) 2133.
[49] S. Ito, T.N. Murakami, P. Comte, P. Liska, C. Gratzel, M.K. Nazeeruddin, M. Gratzel, Thin Solid Films 516 (2008) 4613.
[50] S. Ito, P. Chen, P. Comte, M.K. Nazeeruddin, P. Liska, P. Pechy, M. Gratzel, Prog. Photovoltaics 15 (2007) 603.
[51] D.P. Hagberg, X. Jiang, E. Gabrielsson, M. Linder, T. Marinado, T. Brinck, A. Hagfeldt, L.C. Sun, J. Mater. Chem. 19 (2009) 7232.
[52] X.B. Xu, D.K. Huang, K. Cao, M.K. Wang, S.M. Zakeeruddin, M. Gratzel, Sci. Rep. 3 (2013) .
[53] F. Fabregat-Santiago, J. Bisquert, G. Garcia-Belmonte, G. Boschloo, A. Hagfeldt, Sol. Energy Mater. Sol. Cells 87 (2005) 117.
[54] X. Jiang, K.M. Karlsson, E. Gabrielsson, E.M.J. Johansson, M. Quintana, M. Karlsson, L.C. Sun, G. Boschloo, A. Hagfeldt, Adv. Funct. Mater. 21 (2011) 2944.
[55] M. Ferus, L. Kavan, M. Zukalova, A. Zukal, M. Klementova, S. Civis, J. Phys. Chem. C 118 (2014) 26845.
[56] F. Tian, Y.P. Zhang, J. Zhang, C.X. Pan, Journal of Physical Chemistry C 116 (2012) 7515.
[57] N. Roy, Y. Park, Y. Sohn, K.T. Leung, D. Pradhan, Appl. Mater. Interfaces (2014) .
[58] J.Y. Zheng, S.H. Bao, Y. Guo, P. Jin, ACS Applied Materials & Interfaces 6 (2014) 5940.
[59] M. Grätzel, Prog. Photovolt. Res. Appl. 14 (2006) 429.
[60] S.M. Feldt, E.A. Gibson, E. Gabrielsson, L. Sun, G. Boschloo, A. Hagfeldt, J. Am. Chem. Soc. 132 (2010) 16714.
[61] J. Bisquert, F. Fabregat-Santiago, Dye-sensitized Solar Cells, in: K. Kalyanasundaram (Ed.), CRC Press, 2010 Ch.12.

[62] F. Fabregat-Santiago, J. Bisquert, E. Palomares, L. Otero, D.B. Kuang, S.M. Zakeeruddin, M. Gratzel, J. Phys. Chem. C 111 (2007) 6550.
[63] B.C. O'Regan, S. Scully, A.C. Mayer, E. Palomares, J. Durrant, Phys. Chem. B 109 (2005) 4616.
[64] C. Magne, T. Moehl, M. Urien, M. Grätzel, T. Pauporté, J. Mater. Chem. A 1 (2013) 2079.
[65] Q. Wang, S. Ito, M. Gratzel, F. Fabregat-Santiago, I. Mora-Sero, J. Bisquert, T. Bessho, H. Imai, J Phys Chem B 110 (2006) 25210.
[66] J. Bisquert, F. Fabregat-Santiago, I. Mora-Sero, G. Garcia-Belmonte, E.M. Barea, E. Palomares, Inorg. Chim. Acta 361 (2008) 684.
[67] L. Kavan, M. Grätzel, Electrochim. Acta 40 (1995) 643.
[68] P.G. Wu, C.H. Ma, J.K. Shang, Appl. Phys. A: Mater. Sci. Process. 81 (2005) 1411.
[69] M. Radecka, M. Rekas, A. Trenczek-Zajac, K. Zakrzewska, J. Power Sources 181 (2008) 46.
[70] D.O. Scanlon, C.W. Dunnill, J. Buckeridge, S.A. Shevlin, A.J. Logsdail, S.M. Woodley, C.R.A. Catlow, M.J. Powell, R.G. Palgrave, I.P. Parkin, G.W. Watson, T. W. Keal, P. Sherwood, A. Walsh, A.A. Sokol, Nat. Mater. 12 (2013) 798.
[71] G. Liu, W. Jaegermann, J. He, V. Sundstrom, L. Sun, J. Phys. Chem. B 106 (2002) 5814.
[72] L. Kavan, M. Grätzel, J. Rathousky, A. Zukal, J. Electrochem. Soc. 143 (1996) 394.
[73] B. Ohtani, O.O. Prieto-Mahaney, D. Li, R. Abe, J. Photochem. Photobiol., A 216 (2010) 179.
[74] L. Kavan, M. Grätzel, S.E. Gilbert, C. Klemenz, H.J. Scheel, J. Am. Chem. Soc. 118 (1996) 6716.
[75] J. Bisquert, V.S. Vikhrenko, Journal of Physical Chemistry B 108 (2004) 2313.
[76] S. Nakade, M. Matsuda, S. Kambe, Y. Saito, T. Kitamura, T. Sakata, Y. Wada, H. Mori, S. Yanagida, J. Phys. Chem. B 106 (2002) 10004.
[77] N. Kopidakis, N.R. Neale, K. Zhu, J. van de Lagemaat, A.J. Frank, Applied Physics Letters 87 (2005) .
[78] J. van de Lagemaat, N.G. Park, A.J. Frank, J. Phys. Chem. B 104 (2000) 2044.
[79] L. Bertoluzzi, S. Ma, Phys. Chem. Chem. Phys. 15 (2013) 4283.

Supplementary Information

Electron Kinetics in Dye Sensitized Solar Cells Employing Anatase with (101) and (001) Facets

Barbora Laskova[a,b], Thomas Moehl[c], Ladislav Kavan[a,b,*], Marketa Zukalova[a], Xianjie Liu[d], Aswani Yella[c], Pascal Comte[c], Arnost Zukal[a], Mohammad Khaja Nazeeruddin[c] and Michael Graetzel[c]

[a] *J. Heyrovsky Institute of Physical Chemistry, ASCR, v. v. i. Dolejskova 2155/3, Prague 8, CZ 182 23, Czech Republic*
[b] *Department of Inorganic Chemistry, Faculty of Science, Charles University, Hlavova 2030/8, Prague 2, CZ 128 43, Czech Republic*
[c] *Laboratory of Photonics and Interfaces Institute of Chemical Sciences and Engineering, Swiss Federal Institute of Technology, Lausanne, CH 1015, Switzerland*
[d] *Linköping University, Department of Physics, Chemistry and Biology, S-58183 Linköping, Sweden*

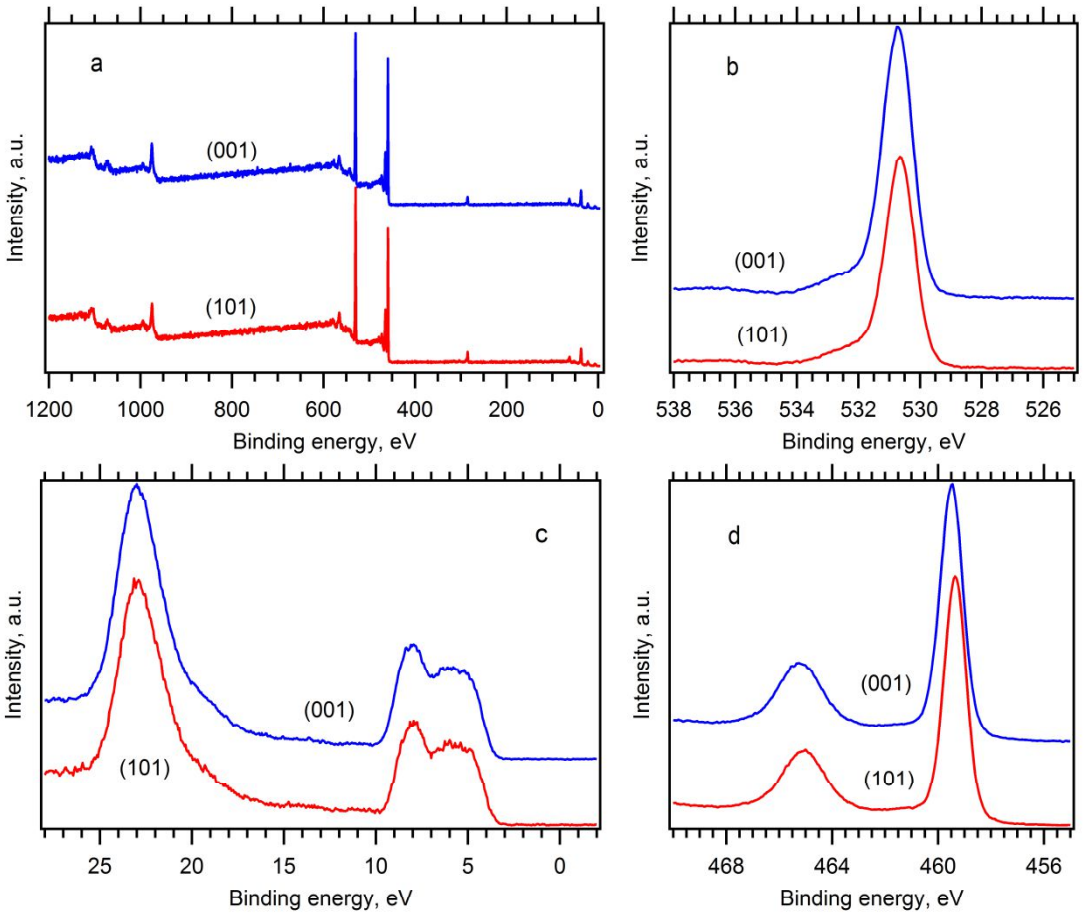

Figure S1: X-ray photoelectron spectra of ANA001 (blue curves) and ANA101 (red curves). (a) Full scan, (b) O1s detail, (c) O2s and valence band, (d) Ti $2p_{1.2}$ and $Ti2p_{3/2}$ detail. Curves are offset for clarity, but the intensity scales are identical in the respective charts.

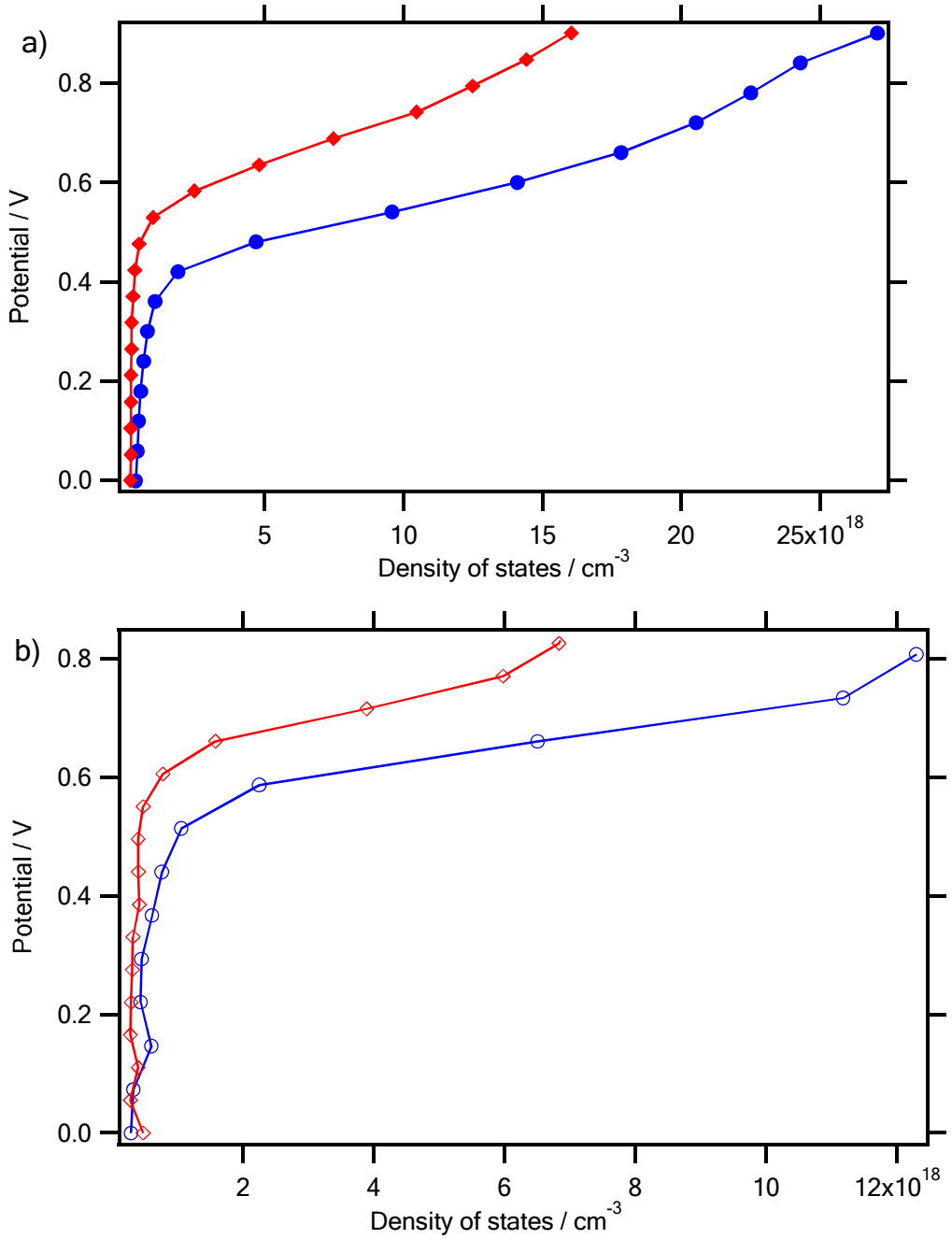

Figure S2. The density of states against applied potential computed for devices employing ANA001 (blue circles) or ANA101 (red diamonds) films as photoanode. The results are for devices with iodide based electrolyte solution (a) and cobalt based electrolyte solution (b).

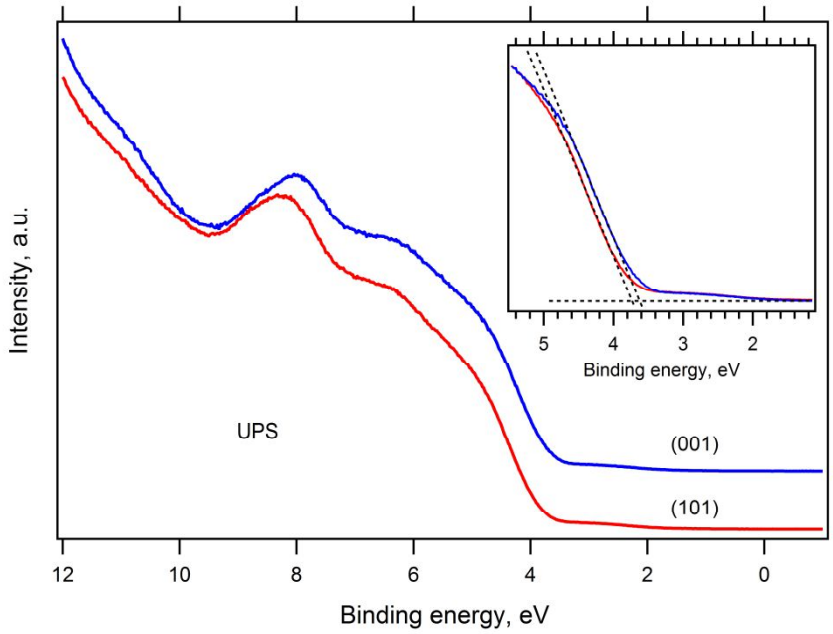

Figure S3: Ultraviolet photoelectron spectra of ANA001 (blue curves) and ANA101 (red curves) in the region of valence-band onset. Curves are offset for clarity, but the intensity scales are identical. Inset shows the detailed spectrum with determination of the valence-band maximum (VBM).

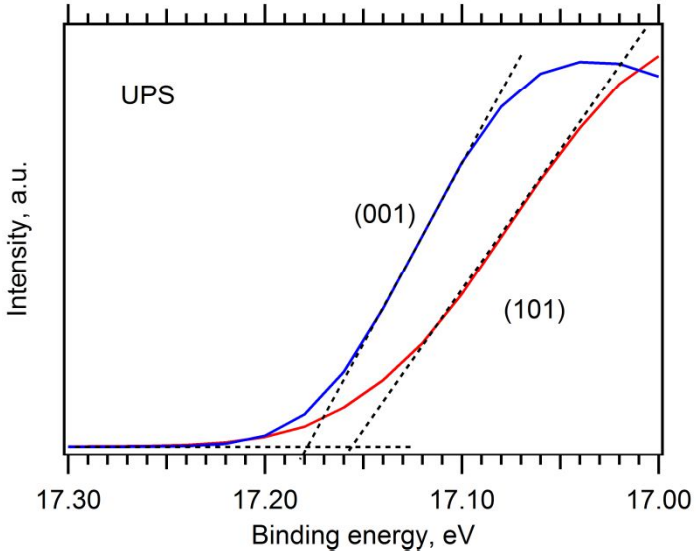

Figure S4: Ultraviolet photoelectron spectra of ANA001 (blue curves) and ANA101 (red curves) in the region of secondary electron cutoff. The linear extrapolation of the spectrum is used for the determination of work function.

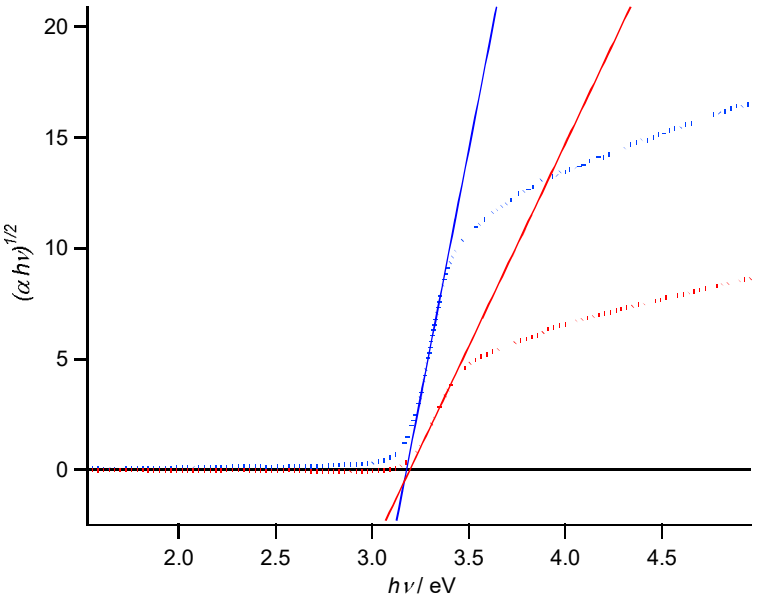

Figure S5. Tauc plot $(\alpha h\nu)^{1/2}$ vs. photon energy $h\nu$ and determination of energy band gap *Eg* for ANA101 (dashed red line) and ANA001 (dashed blue line). The *Eg* was specified by fitting of linear parts of corresponding curves (full lines).

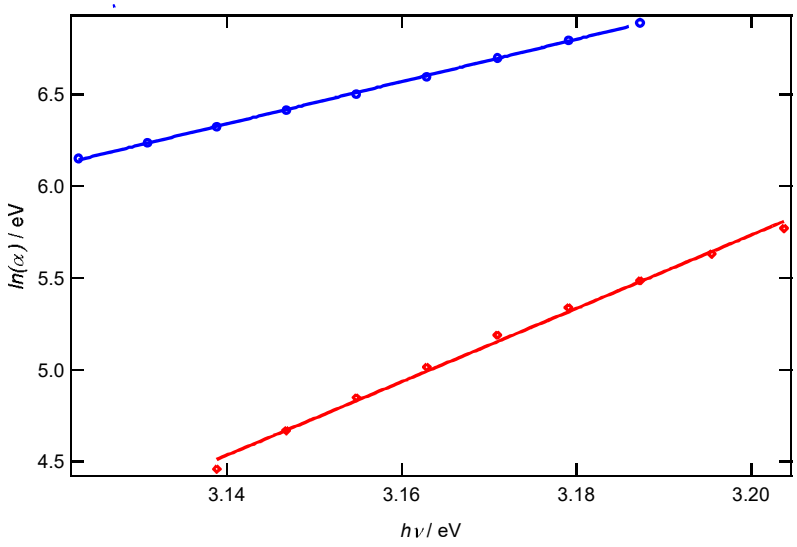

Figure S6. The dependence of ln(α) on hν in the sub-bandgap region for ANA101 (red points) and ANA001(blue points). The corresponding linear fits are depicted by full lines.

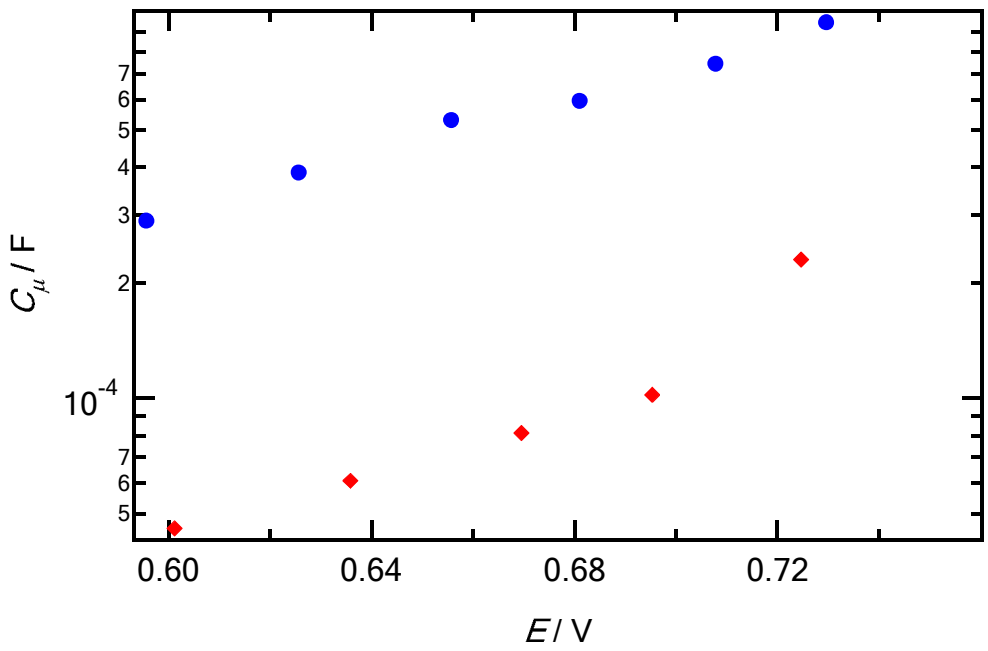

Figure S7. The transient photovoltage measurement. The dependence of chemical capacitance on applied potential for DSCs with iodine based electrolyte employing either ANA001 (blue) or ANA101 (red).